Final Report on AFOSR Grant

F496209610147

Structural Stability of Microlaminates Under Thermal and Mechanical Cycles

Principal Investigator: Timothy P. Weihs, Assistant Professor
Department of Materials Science and Engineering
The Johns Hopkins University
Baltimore, MD 21218-2689

Collaborator: Timothy Foecke, Materials Scientist
Materials Science and Engineering Laboratory
National Institute of Standards and Technology
Gaithersburg, MD 20899

EXECUTIVE SUMMARY

Free-standing Nb/Nb_5Si_3 microlaminate foils were fabricated to investigate their strength at room temperature and their microstructural stability at high temperatures (1200°C–1600°C). The foils were fabricated using a combination of magnetron sputtering and subsequent high temperature anneals. The most promising as-deposited structures consist of crystalline Nb layers and amorphous Nb-Si layers. The Nb-Si layers were co-deposited from elemental targets as well as directly deposited from a compound target. Following deposition the foils were removed from their Si substrates and annealed at 1200°C to crystallize the silicide layers. The resulting layers of Nb and Nb_5Si_3 were chemically distinct and flat with no continuous columnar grain boundaries or growth defects, both of which can degrade mechanical properties. Experiments with self-propagating reactions in Nb/Si nanolaminates were undertaken to demonstrate that Nb/Nb_5Si_3 composite foils can also be fabricated and shaped through the use of the very exothermic reaction of Nb and Si.

Since Nb and Nb_5Si_3 have disparate coefficients of thermal expansion, considerable thermal stresses can arise in the microlaminate foils on cooling from high-temperature anneals. Using an improved, assymetric X-ray diffraction analysis, we have shown that residual stresses as high as 300MPa can appear in the alternating layers; the silicide layers being in compressive and the Nb layers in tension.

When tested in tension at room temperature, the Nb/Nb_5Si_3 microlaminate foils showed high strengths and small plastic elongations. The silicide layers fractured in a brittle manner and the Nb layers showed local plasticity when blunting and bridging cracks in the silicide layers. The elastic limit for most samples was near 560MPa and appears to be controlled by fracture of the silicide layer. For samples with very small silicide layer thicknesses, there is some indication that the elastic limit increases substantially. The ultimate tensile strength of the microlaminates varied from 471MPa to 1101MPa, increasing continuously as bilayer thickness and silicide layer thickness decreased, and as volume fraction of the Nb increased.

To investigate the stability of the Nb/Nb_5Si_3 microlaminates at high temperatures, we considered the chemical, phase, and microstructural stability of the samples. The predominant high-temperature breakdown mechanism in vacuum was a chemical instability: the loss of Si from the outermost Nb_5Si_3 layers. Si diffused perpendicular to the layering, through the outermost Nb layer, and sublimed to the atmosphere. (Si was also lost from the ends of the samples by subliming directly from the exposed ends of the silicide layers.) The rate at which Si was lost depended on the diffusion rate of Si in the Nb layers and the vapor pressure of Si in the external atmosphere. Raising the external partial pressure of Si or annealing in flowing Ar dramatically reduced the rate at which Si was lost. Ignoring the damaging effects of sublimation, the foils were otherwise chemically stable with little dissolution of Si from the silicide layers into the Nb layers at elevated temperatures.

While the equilibrium Nb and Nb_5Si_3 phases were stable up to 1500°C, a metastable Nb_3Si phase formed on the Nb/Nb_5Si_3 interfaces on annealing at 1500°C and 1600°C. The Nb_3Si phase appears to be stress induced. An amorphous, impurity stabilized, intergranular phase also formed in the Nb_5Si_3 layers on annealing. Microstructurally, the microlaminates are very stable. While porosity develops in the silicide layers at elevated temperatures due to tensile stresses, the Nb/Nb_5Si_3 interfaces are very stable and exhibit very little grooving, even at 1600°C. The measured groove angles suggest that breakdown of the layering is most likely to occur via pinch-off of the Nb layers. This would leave the creep-resistant silicide layers fully continuous and load bearing.

REPORT DOCUMENTATION PAGE

AFRL-SR-BL-TR-00-

0409

1. REPORT DATE *(DD-MM-YYYY)*	2. REPORT TYPE	3. DATES COVERED *(From - To)*
	Final Report	05/01/96 to 07/31/99

4. TITLE AND SUBTITLE
Structural Stability of Microlaminates Under Thermal and Mechanical Cycles

5a. CONTRACT NUMBER
F496209610147

5b. GRANT NUMBER
F49620-96-1-0147

5c. PROGRAM ELEMENT NUMBER

6. AUTHOR(S)
Weihs, Timothy P.,*

Van Heerden, David,*

Foecke, Timothy,**

5d. PROJECT NUMBER

5e. TASK NUMBER
2306/AS

5f. WORK UNIT NUMBER

7. PERFORMING ORGANIZATION NAME(S) AND ADDRESS(ES)

*Dept. of Mat. Sci. 7 Eng.
Johns Hopkins University
3400 North Charles St.
Baltimore, MD, 21218

**Mat. Sci. & Eng. Laboratory
National Institute of Standards
And Technology
Gaithersburg, MD, 20899

8. PERFORMING ORGANIZATION REPORT

9. SPONSORING / MONITORING AGENCY NAME(S) AND ADDRESS(ES)
Dr. Spencer Wu
AFOSR/NA
801 N. Randopl Street
Arlington Va 22203-1977

10. SPONSOR/MONITOR'S ACRONYM(S)

11. SPONSOR/MONITOR'S REPORT NUMBER(S)

12. DISTRIBUTION / AVAILABILITY STATEMENT
no restrictions on distribution

DISTRIBUTION STATEMENT A
Approved for Public Release
Distribution Unlimited

13. SUPPLEMENTARY NOTES
none

14. ABSTRACT: Free-standing Nb/Nb_5Si_3 microlaminate foils were fabricated using a combination of magnetron sputtering and subsequent high temperature anneals (1200°C). The Nb and Nb_5Si_3 layers were chemically distinct and flat with no growth defects. The silicide layers, however, have a residual compressive stress and the Nb layers a residual tensile stress. At room temperature, the Nb/Nb_5Si_3 microlaminates showed ultimate tensile strengths ranging from 471MPa to 1101MPa, increasing continuously as bilayer thickness decreased and volume fraction of Nb increased. The predominant high-temperature breakdown mechanism in vacuum was a loss of Si from the outermost Nb_5Si_3 layers via sublimation. Raising the external partial pressure of Si or annealing in flowing Ar dramatically reduced the rate at which Si was lost. While the equilibrium Nb and Nb_5Si_3 phases were stable up to 1500°C, a metastable Nb_3Si phase formed on the Nb/Nb_5Si_3 interfaces on annealing at 1500°C and 1600°C. The Nb_3Si phase appears to be stress induced. The Nb/Nb_5Si_3 interfaces, themselves, are very stable and exhibit very little grooving, even at 1600°C.

15. SUBJECT TERMS
Microlaminates, Structural Stability, Chemical Stability, Phase Stability, Vapor Deposition, thermal Stresses, Strength, and Fracture

16. SECURITY CLASSIFICATION OF:			17. LIMITATION OF ABSTRACT	18. NUMBER OF PAGES	19a. NAME OF RESPONSIBLE PERSON
a. REPORT U - unclassified	b. ABSTRACT U - unclassified	c. THIS PAGE U - unclassified	UU	106	19b. TELEPHONE NUMBER *(include area code)* (410) 516-4071

TABLE OF CONTENTS:

1. Introduction

Jet engine manufacturers are striving to develop new structural materials that can operate at temperatures well above 1100°C in order to increase engine efficiency and power [1-15]. The material requirements for this application are stringent [1-7,16-18]. Creep rates must be less than $3x10^{-8}$ sec^{-1} for an applied stress of 100MPa at 1100°C, and oxidation rates must be low. Microstructures and chemistries must be stable, and densities must be near or below $8g/cm^3$. At lower temperatures, the materials must have fracture toughnesses near $20MPa\sqrt{m}$ and 1 to 2% ductility in tension to withstand impacts with high-velocity particles.

Along with these material requirements that are based on the jet engine application, new requirements are arising that are based on the processing of the turbine blades. Jet engine designers want to decrease the outer wall thickness on their turbine blades to 300μm [16,18], and this generates significant challenges when attempting to fabricate such structures. Traditional processing techniques such as investment casting will be extremely difficult because mold walls can shift up to 50μm during fabrication [16]. Thus, alternative methods such as vapor deposition are being investigated. More specifically, jet engine manufacturers are attempting to vapor deposit the outer walls of a turbine blade onto an inner spar that is directionally cast or extruded [2,16,18]. Thus, any new material may also need to be compatible with vapor deposition techniques.

One set of materials that hold particular promise for future turbine blades is Nb/Nb_5Si_3 composites [1-8, 19-27]. These Refractory Metal-Intermetallic Composites (RMICs) have received considerable attention because they are chemically and microstructurally stable up to 1650°C and their densities are similar to most superalloys. The ductile Nb toughens the composite at room temperature, and the brittle silicide

strengthens the composite at high temperatures. In addition, alloying can enhance oxidation resistance [2], an important issue for Nb-based alloys.

Nb/Nb_5Si_3 *in situ* composites have been formed by casting and extruding Nb alloys that contain 10-17 at% Si [1-7]. After anneals at 1500°C their microstructures generally consist of elongated Nb dendrites (50μm) in a Nb_5Si_3 matrix as shown in Figure 1.1(a). The Nb_5Si_3 matrix also contains small Nb particles (5μm) [5,20-22]. Nb/Nb_5Si_3 microlaminate composites have also been fabricated using hot-pressing [28-30] and vapor deposition techniques [31-33]. Figure 1.1(b) shows a cross-sectional SEM image of a microlaminate from our current project that was sputter deposited near room temperature and then annealed at 1400°C [31-33].

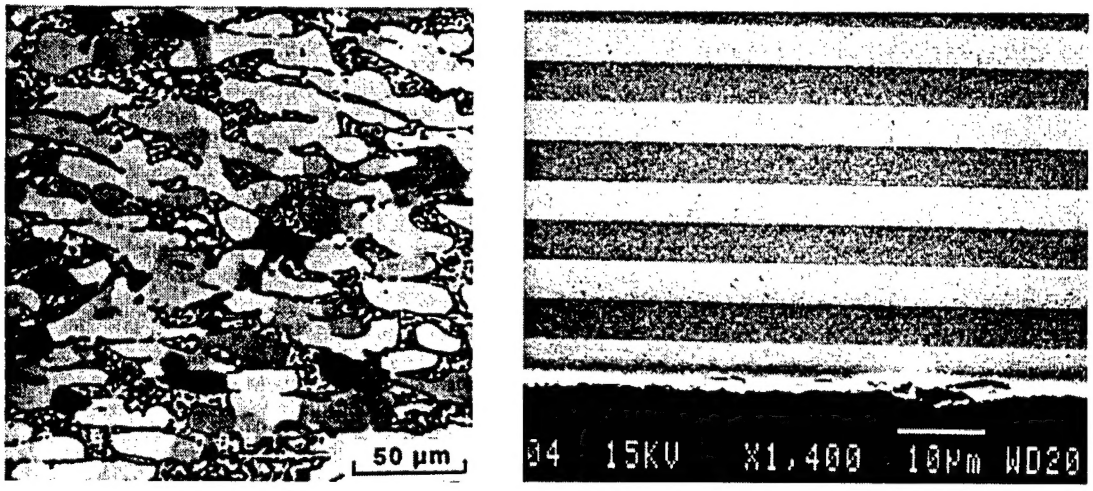

(a) (b)

Figure 1.1: (a) Cross-sectional micrograph from [22] showing a Nb/Nb_5Si_3 *in situ* composite that was hot extruded at 1482°C. The light phase is the primary Nb and the dark phase is Nb_5Si_3 with small Nb particles. (b) A cross-sectional SEM view of a Nb/Nb_5Si_3 microlaminate that was vapor deposited and annealed at 1400°C; the light layers are Nb and the dark layers are Nb_5Si_3 [32].

Since the enhanced mechanical properties of the Nb-based refractory composites depend strongly on the unique microstructure of the materials, the individual layers and phases in these composites will need to be stable at elevated operating temperatures. This is particularly true of the laminated composites [30-44]. Consider just one supporting example. Rowe et al. [37, 38] have shown that the room temperature fracture strength of $Nb/NbCr_2$ microlaminates decreases from 735MPa to 475MPa when layer thicknesses increase from 2μm to 6μm. This example shows that coarsening of layers or grains can affect the mechanical properties of the refractory composites. Thus, to utilize refractory microlaminates in jet turbine engines, one must be sure that the microlaminate's performance-enhancing microstructure is stable under severe operating conditions.

The initial efforts to develop Nb-based microlaminates focused on Nb/Nb_3Al and $Nb/NbCr_2$ microlaminates with promising reports on mechanical and structural properties. Rowe et al. [37, 38] and Cao et al. [41, 42] studied the room temperature strength and toughness and the high temperature stability of Nb/Nb_3Al and $Nb/NbCr_2$ microlaminates. The microlaminates were magnetron sputter deposited to a total thickness of 150μm and were tested as free-standing foils. Microlaminates with both 2μm and 6μm layer thicknesses were investigated. The Nb/Nb_3Al laminates with 2μm thick layers have an average fracture strength of 476MPa and an average toughness of $10MPa\sqrt{m}$. In comparison, the Nb/Cr_2Nb laminates have a higher average fracture strength of 735MPa, and a higher fracture toughness of $18MPa\sqrt{m}$ [37, 38]. The higher strengths and toughnesses are largely attributed to Cr solid solution strengthening of the Nb in the $Nb/NbCr_2$ microlaminates [37, 38]. The stronger Nb layers strengthen and toughen the $Nb/NbCr_2$ microlaminates relative to the Nb/Nb_3Al microlaminates which have softer, relative pure Nb layers. Based on these differences alone, the Nb-Cr system is considered to be more promising than the Nb-Al system [37, 38].

Rowe et al. [37, 38] also investigated the high temperature microstructural stability of Nb/Nb_3Al and $Nb/NbCr_2$ microlaminates using 2hr isothermal anneals. They found that the volume fraction of Nb_3Al in the Nb/Nb_3Al microlaminates dropped rapidly above 1000°C. This implies that 1000°C is the upper limit for the stability of microstructures in Nb/Nb_3Al microlaminates with 2μm thick layers. The Nb-Cr laminates show a good bit more stability. The $NbCr_2$ volume fraction in the $Nb/NbCr_2$ microlaminates did not drop significantly until temperatures above 1200°C were reached. Thus, the upper limit for microstructural stability in $Nb/NbCr_2$ microlaminates is 1200°C or higher. An additional concern with the Nb-Cr system, though, is the large variation of Cr solubility in Nb with temperature. Cr solubility in Nb increases from approximately 2 at% at 900°C to approximately 15 at% at 1600°C. Such variations in solubility with temperature can lead to unwanted precipitate formations and associated internal stresses as noted by Rowe et al. [37, 38].

Nb/Nb_5Si_3 microlaminates have also been investigated by several different groups. Kajuch, Short and Lewandowski [39, 40] studied the mechanical properties of these microlaminates by fabricating trilayer $Nb_5Si_3/Nb/Nb_5Si_3$ composites in a two-stage process. They first hot-pressed mechanically alloyed Nb_5Si_3 powders into 4mm thick layers. Then they sandwiched a 250μm thick Nb foil between two Nb_5Si_3 layers and vacuum hot pressed the trilayer structures at 10MPa and 1200°C for 5 hrs. The laminate composites showed significant increases in toughness compared to the single layers of hot-pressed mechanically alloyed Nb_5Si_3. The Nb layer blunted cracks within the composite, much the same way that the Nb particles blunted cracks in the *in situ* Nb/Nb_5Si_3 composites. The 8.6 MPa $\sqrt{m}$ fracture toughness that was measured for the laminated trilayer represents a five-fold increase over the toughness of monolithic Nb_5Si_3.

Much larger increases are very likely obtainable with vapor processing that can minimize the size of defects.

Provancher and Ghosh [43] took a somewhat similar approach to Kajuch, Short and Lewandowski and hot pressed elemental layers of Si and Nb at 1650°C and 27.6MPa for 8 hrs. This process relied on reaction synthesis to form a 0.30 to 0.36 volume fraction of Nb_5Si_3 in the 32 at% Si composite. The resulting 2.1mm thick laminates were tested in tension at 1100°C and showed approximately 2.0% ductility and an average UTS near 200MPa. The Nb_5Si_3 phase cracked first as expected and the remaining Nb acted as a bridging element. While the resulting strengths at 1100°C are low compared to the 261MPa measured for *in situ* Nb/Nb_5Si_3 composites at 1500°C, the finer microstructure in the microlaminates is a likely explanation.

In terms of the stability of Nb/Nb_5Si_3 microlaminates, little work has been reported. Bhattacharya, Rai, Mediratta, and Cheng [44] investigated solid state reactions of Nb and Si in evaporated layers of Nb, Si and Nb-Si. They found that 2000Å/2000Å bilayers of Nb and Si reacted to form $NbSi_2$ at 600°C, and then Nb_5Si_3 at 900°C during short isothermal anneals. The $NbSi_2$ grew at 35Å/min under diffusion limited conditions. They also noted that co-deposited Nb-Si is amorphous following deposition, and it remains amorphous during 600°C anneals. The amorphous structure does not begin to crystallize into Nb_5Si_3 until 900°C with grain size ranging from 50nm to only 300nm. This sluggish crystallization, the stability of the fine-grained Nb_5Si_3 (50-300nm grain size), and the sluggish compound formation in the Nb/Si bilayers suggests that equilibrium Nb/Nb_5Si_3 microlaminates will be stable well above 1000°C. This AFOSR project was designed to investigate the microstructural stability of Nb/Nb_5Si_3 microlaminates at temperatures ranging from 1200°C to 1600°C, as well as to gain an insight into their room temperature mechanical properties.

1.1. References For Section 1

1. P.R. Subramanian, M.G. Mendiratta, D.M. Dimiduk, and M.A. Stuck, *Mater. Sci. Eng.*, **A240** (1997) 1.

2. B.P. Bewlay, M.R. Jackson, and H.A. Lipsitt, *Metal. Mater. Trans.A*, **27A** (1996) 3801.

3. B.P. Bewlay, M.R. Jackson, and P.R. Subramanian, *JOM,* April 1999, 32.

4. D.P. Pope and R. Darolia, *MRS Bulletin*, May 1996, 30.

5. P.R. Subramanian, M.G. Mendiratta, and D.M. Dimiduk, *JOM,* January 1996, 33.

6. M.R. Jackson, B.P. Bewlay, R.G. Rowe, D.W. Skelly, and H.A. Lipsitt, *JOM*, January, 1996, 39.

7. D. M. Dimiduk, M.G. Mendiratta, and P.R. Subramanian, in *Structural Intermetallics*, TMS Proceedings edited by R. Darolia, J.J. Lewandowski, C.T. Liu, P.L. Martin, D.B. Miracle, and M.V. Nathal, (1993) 619.

8. P.R. Subramanian, M.G. Mendiratta, and D.M. Dimiduk, in *Mat. Res. Soc. Symp. Proc.*, **322** (1994) 491.

9. K. Sadananda and C.R. Feng, in *Mat. Res. Soc. Symp. Proc.*, **322** (1994) 157.

10. A.K. Vasudevan and J.J. Petrovic, *Mater. Sci. Eng.*, **A155** (1992) 1.

11. D.M. Shah, D. Berczik, D.L. Anton, and R. Hecht, *Mater. Sci. Eng.*, **A155** (1992) 45.

12. S.M. Wiederhorn, R.J. Gettings, D.E. Roberts, and C. Ostertag, *Mater. Sci. Eng.*, **A155** (1992) 209.

13. T.G. Nieh and J. Wadsworth, MRS Symposium Proceedings, edited by C.L. Briant, J.J. Petrovic, B.P. Bewlay, A.K. Vasudevan and H.A. Lipsitt, **322** (1994) 315.

14. C.L. Briant in MRS Symposium Proceedings, edited by C.L. Briant, J.J. Petrovic, B.P. Bewlay, A.K. Vasudevan and H.A. Lipsitt, **322** (1994) 305.

15. See MRS Symposium Proceedings, edited by C.L. Briant, J.J. Petrovic, B.P. Bewlay, A.K. Vasudevan and H.A. Lipsitt, **322** (1994).

16. Private Communication with Dr. Mel Jackson and Dr. Bernard Bewlay at General Electric Corporate, CRD, Schenectady, NY.

17. Private Communication with Dr. Doug Berczik at Pratt and Whitney Aircraft, West Palm Beach, FL.

18. AFOSR Metallic Materials Contractors Meeting, San Diego, CA, March 4-5, 1999.

19. M.G. Mendiratta and D.M. Dimiduk, *Scripta Met.*, **25** (1991) 237.

20. M.G. Mendiratta, J.J. Lewandowski and D.M. Dimiduk, *Metall. Trans.*, **22A**, (1991) 1573.

21. J.D. Rigney and J.J. Lewandosky, *Metall and Mater. Trans.*, **27A**, 3292 (1996).

22. M.G. Mendiratta and D.M. Dimiduk, *Met Trans, A,* **24A** (1993) 501.

23. P.R. Subramanian, M.G. Mediratta, and M.G. Mendiratta, in Mat. Res. Soc. Symp. Proc., 322, 491 (1994).

24. B.P. Bewlay, M.R. Jackson, and H.A. Lipsitt, in TMS Proceedings: *Processing and Design Issues in High Temperature Materials*, May 1996, 247.

25. M Thirukkonda, B. Cockeram, M. Saqlb, L.E. Matson, R. Srinvasan, and I. Weiss, *Scripta Metall & Mater.*, **27**, (1992) 711.

26. B. Cockeram, M. Saqib, R. Srinivasan, and I. Weiss, *Scripta Metall & Mater.*, **27**, (1992) 749.

27. B. Cockeram, R. Srinivasan, and I. Weiss, *Scripta Metall & Mater.*, **27**, (1992) 755.

28. J. Kajuch, J.D. Rigney and J.J. Lewandowski, *Mat. Sci. and Eng.*, **A155** (1992) 59.

29. J. Kajuch, J. Short, and J.J. Lewandowski, *Acta. metall. mater.*, **43** (1995) 1955.

30. W. Provancher and A.K. Ghosh, in MRS Proceedings, **364** (1994) 1071.

31. D. Van Heerden, C.H. Shang, A.J. Gavens, and T.P. Weihs in Proceedings of Fifth International Conference on Composites Engineering, edited by D. Hui, 909-10, July 1998.

32. D. Van Heerden, A.J. Gavens, T. Foecke, and T.P. Weihs, *Mat. Sci. and Eng. A.*, **A261**, (1999) 212

33. A.J. Gavens, D. Van Heerden, T. Foecke, and T.P. Weihs, *Metall. and Mater. Trans.* **30** (1999) 2959.

34. T.G. Nieh and J. Wadsworth, MRS Symposium Proceedings, edited by C.L. Briant, J.J. Petrovic, B.P. Bewlay, A.K. Vasudevan and H.A. Lipsitt, **322** (1994) 315.

35. C.L. Briant, MRS Symposium Proceedings, edited by C.L. Briant, J.J. Petrovic, B.P. Bewlay, A.K. Vasudevan and H.A. Lipsitt, **322** (1994) 305.

36. See MRS Symposium Proceedings, edited by C.L. Briant, J.J. Petrovic, B.P. Bewlay, A.K. Vasudevan and H.A. Lipsitt, **322** (1994).

37. R.G. Rowe, D.W. Skelly, M. Larsen, J. Heathcote, G.R. Odette, and G. Lucas, *Scripta Metall et Mater,* **31** (1994) 1487.

38. R.G. Rowe, D.W. Skelly, M. Larsen, J. Heathcote, G. Lucas, and G.R. Odette, MRS Symposium Proceedings, Edited by C.L. Briant, J.J. Petrovic, B.P. Bewlay, A.K. Vasudevan and H.A. Lipsitt, **322** (1994) 461.

39. J. Kajuch, J. Short, and J.J. Lewandowski, *Acta. metall. mater.*, **43** (1995) 1955.

40. J. Kajuch, J.D. Rigney and J.J. Lewandowski, *Mat. Sci. and Eng.*, **A155** (1992) 59.

41. H. Cao, J. P. A. Lofvander, A.G. Evans, R.G. Rowe, and D.W. Skelly, *Mater. Sci. and Eng.*, **A185** (1994) 87.

42. G.R. Odete, B. L. Chao, J.W. Sheckherd, and G.E. Lucas, *Acta. metall. mater.*, **40** (1992) 2381.

43. W. Provancher and A.K. Ghosh, MRS Proceedings, 1994, **364**.

44. R. S. Bhattacharya, A.K. Rai, M.G. Mediratta, and Y.T. Cheng, MRS Symposium Proceedings, **194** (1990) 71.

2. Processing of Microlaminates

An ideal microlaminate for structural applications would contain distinct, flat, and continuous layers with large equiaxed grains that lack a gross columnar microstructure or other deposition defects. The purpose of this study was to identify a method for fabricating Nb/Nb_5Si_3 microlaminates that resemble this ideal structure. Laminate phase geometries have been previously fabricated by hot pressing foils or by physical vapor deposition (PVD). In general, PVD produces laminate materials with fewer impurities at the layer interfaces and enables the production of components with complex geometries. A limited number of investigators have examined the PVD of Nb/Nb_5Si_3 laminates. Bhattacharya et al. evaporated Nb/Si nanolaminates by e-beam evaporation which, following a heat treatment, formed Nb/Nb_5Si_3 nanolaminates [1]. In contrast, Rawal et al. sputter deposited nanolaminates of Nb/Nb_5Si_3 directly onto heated substrates [2]. The heated substrates ensured that the Nb_5Si_3 layers were deposited in a crystalline state, thus eliminating the need for subsequent heat treatments. However, this deposition method resulted in a gross columnar microstructure that spans multiple layers, and would likely limit the room temperature fracture toughness and high temperature creep resistance of the laminate.

In this study we achieved a more ideal microlaminate structure by the room temperature magnetron sputter deposition of Nb and amorphous Nb-Si and a high temperature heat treatment to form crystalline layers of Nb and Nb_5Si_3. The Nb-Si layers were intentionally deposited amorphous to prevent the formation of a gross columnar structure from extending across the thickness of the microlaminate. The processing and

microstructure of these microlaminates is presented. Furthermore we describe a new technique in which fully-dense Nb/Nb_5Si_3 microlaminate composites can be fabricated by means of Self-Propagating High Temperature Synthesis.

2.1 Deposition methods

Microlaminate foils were deposited using three different magnetron sputter deposition methods as indicated in Figure 2. 1. In the first method, layers of Nb and Si (Nb/Si) were deposited from elemental targets with 99.95% and 99.999% purities, respectively. A heat treatment was then performed, during which Nb and Si interdiffused to form a layered structure of Nb and Nb_5Si_3. In the second method, Nb layers were deposited from a Nb target while amorphous Nb-37.5at%Si (Nb-Si) layers were codeposited from elemental Nb and Si targets. In comparison to the first method, no long-range diffusion was required to form the crystalline Nb_5Si_3 layers. In the third fabrication method, Nb layers were deposited from an elemental target and amorphous Nb-Si layers were deposited from a polycrystalline Nb_5Si_3 (99.95% purity) target. In this case, the composition of the silicide layer was determined primarily by the Nb_5Si_3 target rather than the deposition parameters, and again no long-range diffusion was necessary to crystallize the silicide phase.

The chamber base pressure prior to deposition was 1 x 10^{-7}Torr and the pressure of the high purity Ar during deposition was 5.0mTorr. The microlaminates were deposited onto polished <100> Si wafers that had been previously coated with approximately 0.3 μm of Ti followed by approximately 3.0 μm of Cu. The wafers were neither heated nor

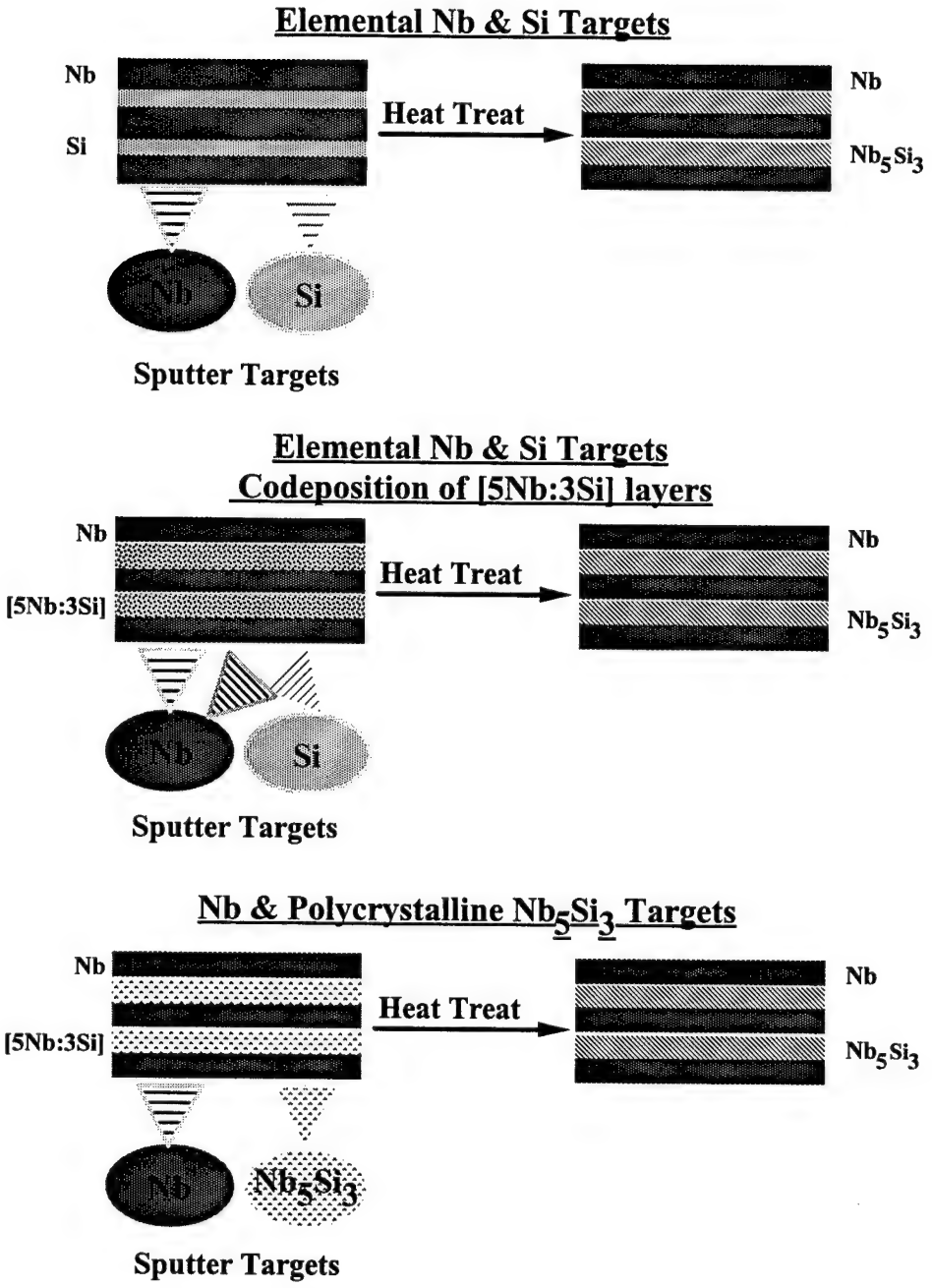

Figure 2. 1: Magnetron sputter deposition methods used to fabricate microlaminate foils of Nb/Nb_5Si_3.

cooled during the deposition. Microlaminate foils were deposited having bilayer thicknesses ranging from 0.57 μm to 20 μm, with volume fractions of Nb of 0.5 to 0.91 and total thicknesses of 50 μm to 70 μm. All of the microlaminates were capped with Nb on both surfaces. Following deposition, free-standing microlaminate foils were obtained by etching away the sacrificial Cu layer with nitric acid.

The layers of the as-deposited microlaminate foils appeared uniform, flat, and distinct as shown in Figure 2.2. The Nb layers had a strong <110> texture and the Nb grains were elongated with the longer axis normal to the layers, as shown in Figure 2.2 (b) and Figure 2.3. The Nb grains did not appear to traverse the entire layer and had an average diameter of 210 nm with an aspect ratio of approximately 4.7. The Si and Nb-Si layers were deposited amorphous as indicated by TEM and x-ray diffraction patterns (Figures 2.2 (b) and 2.3). The layer interfaces showed minimal grooving or roughness.

As anticipated the amorphous silicide layers prevented the formation of a gross columnar grain structure that was observed by Rawal et al. who sputter deposited onto heated substrates [2]. The amorphous layers forced grains in each new Nb layer to nucleate without any spatial correspondence with the grains in the previous Nb layers, thus eliminating the formation of a continuous or gross columnar structure. Additionally, there was no evidence of growth defects in the fracture surfaces of the microlaminates. Growth defects have been observed in other microlaminate alloys and are known to act as initiation sites for fracture and can significantly reduce the strength of microlaminates [3,4]. The lack of growth defects in the present samples suggests that particulate-free deposition onto clean, polished, single crystal Si substrates reduces the likelihood of defect formation.

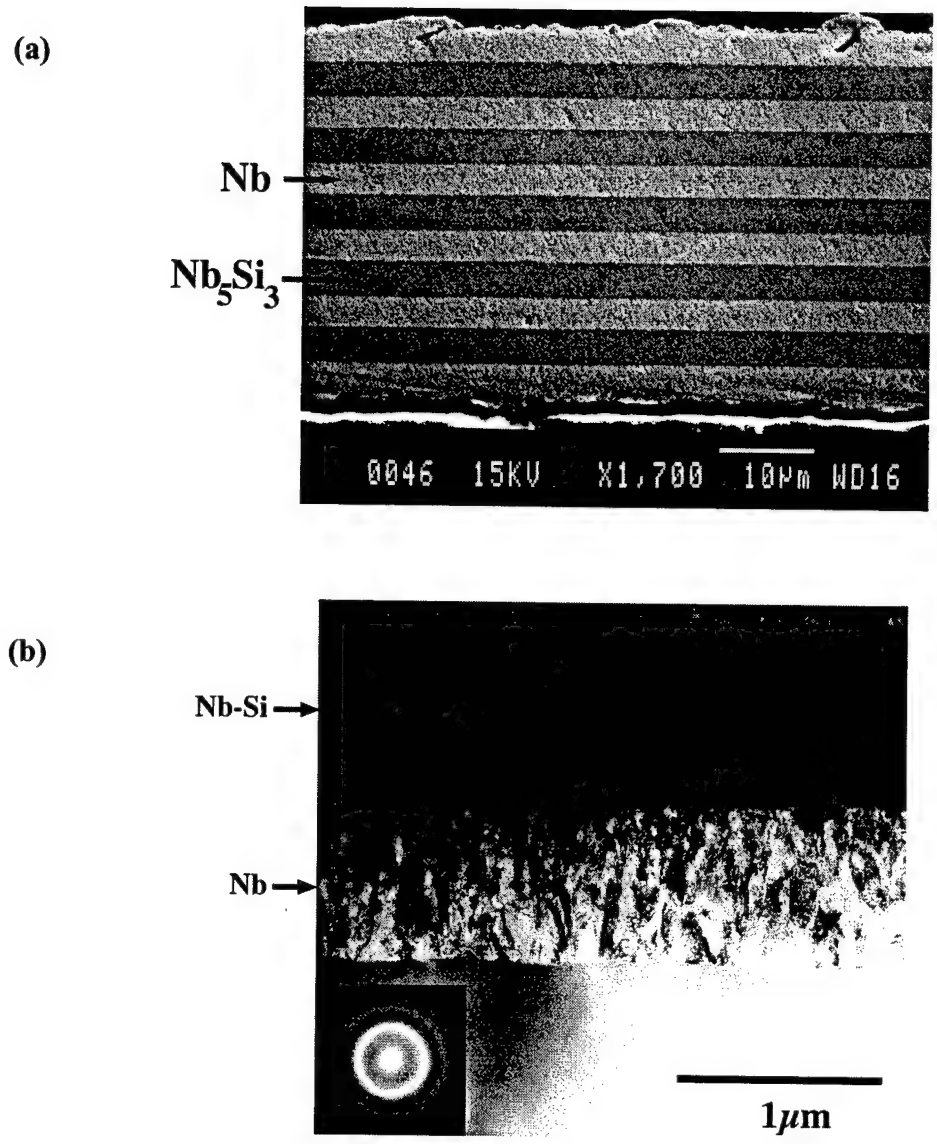

Figure 2. 2. (a) Cross-sectional SEM micrograph of an as-deposited Nb/Nb-Si microlaminate with a 10μm bilayer. (b) Cross-sectional TEM micrograph of an as-deposited Nb/Nb-Si microlaminate with a 2μm bilayer. The electron diffraction ring pattern was obtained from the amorphous Nb-Si layer. Note the columnar grain structure in the Nb layers.

2.2 Transformations on Annealing and Final Phases

Differential Thermal Analysis (DTA) was performed on the as-deposited foils using a Perkin Elmer DTA to determine the temperature at which solid state transformations occur. The foils were heated from room temperature to 1450°C at a rate of 10 °/min in flowing, gettered, high purity Ar. When the Nb/Nb-Si foils were heated in the DTA, one exothermic peak was observed for each sample. This exotherm initiated between 725°C and 840°C, depending on the deposition method and bilayer thickness. X-ray diffraction analysis of foils heated to temperatures just above the exotherm showed that this exotherm was due to the crystallization of the amorphous silicide phase into the crystalline αNb_5Si_3 phase. Typically, the exotherm was completed after reaching 900°C, suggesting that annealing the foils at 1000°C would result in the desired phases of Nb and Nb_5Si_3. A DTA analysis was not performed on the Nb/Si foils because, when heated, these foils delaminated within the amorphous Si layers.

The free-standing foils were heat treated in a vacuum furnace that was maintained in the low 10^{-5} Torr range. During the heat treatment, the foils were placed in a covered alumina crucible and held at temperatures ranging from 1000°C to 1200°C for 3 hours. X-ray diffraction traces of microlaminates deposited using a polycrystalline target and heat treated at 1000°C and 1200°C are shown in Figure 2.3. The 1000°C heat treatment produced a material consisting of Nb, Nb_5Si_3, and Nb_3Si. Increasing the heat treatment temperature to 1200°C yielded only the equilibrium phases of Nb and Nb_5Si_3. The higher temperature heat treatment, therefore, is clearly beneficial, since the transformation of

Nb_3Si to Nb_5Si_3 has been shown to be sluggish [5]. Similar results were observed in the foils with codeposited Nb-Si layers.

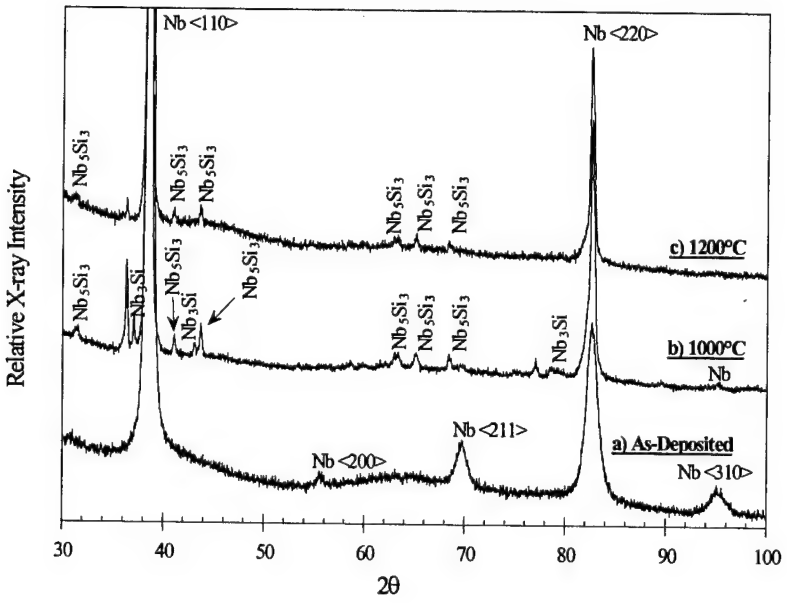

Figure 2. 3. X-ray diffraction pattern of Nb/Nb-Si microlaminate foils a) as-deposited, and heat treated for 3 hours at b) 1000°C, and c) 1200°C.

After the 1200°C heat treatment, the layers of the microlaminates remained intact without any significant indication of interface roughening (Figure 2. 4.). However, the average diameter of the Nb grains increased from 210nm to 750nm and the grains became more equiaxed with their aspect ratio decreasing from approximately 4.7 to approximately 2.2 and their <110> texture was enhanced. For the foils with thinner layers, the Nb grains extended across the individual layers, whereas for the foils with thicker layers, the Nb grains were often shorter than the thickness of the layers (Figure 2.4.(b)). Oxygen was not detected in the thicker Nb layers examined with an EDS system, which implies that there was minimal environmental contamination from the heat

treatment. The Nb_5Si_3 grains were relatively equiaxed and were typically less than 300nm in diameter.

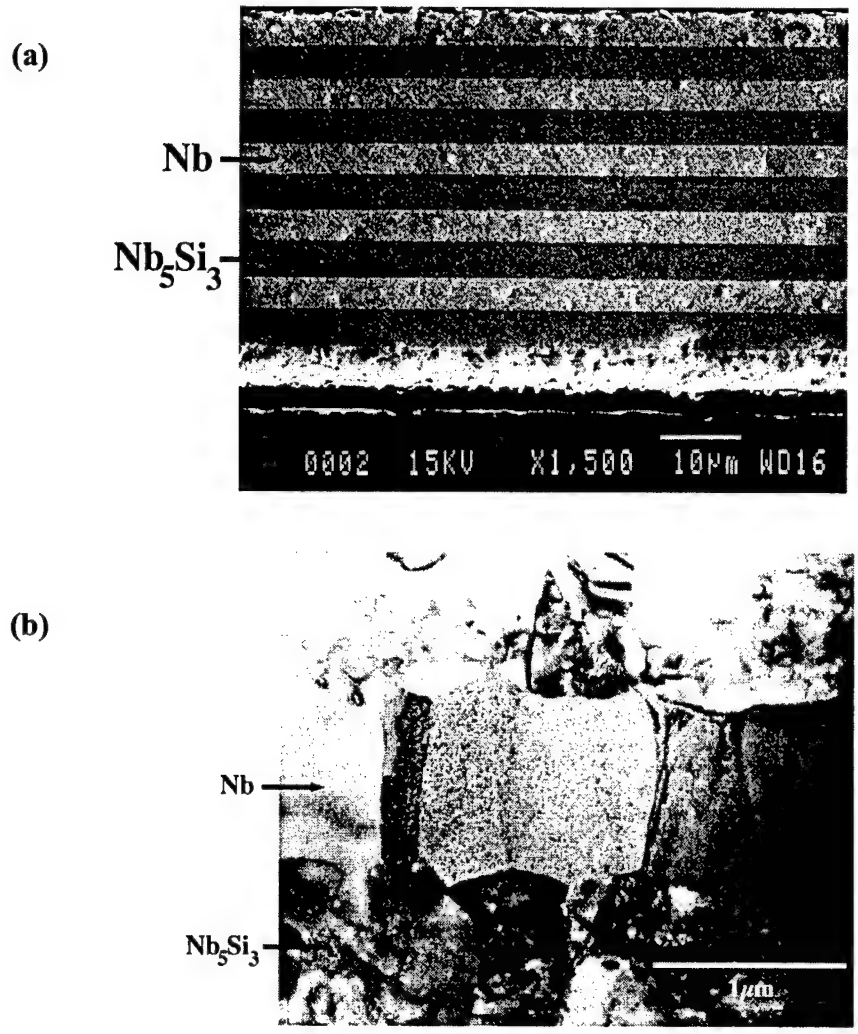

Figure 2. 4. Cross-sectional micrographs of a Nb/Nb_5Si_3 microlaminate heat treated for 3 hours at 1200°C (a) SEM micrograph and (b) TEM micrograph.

The DTA results indicate that the crystallization of Nb_5Si_3 initiates close to 800°C and is completed by approximately 900°C without the formation of additional silicide phases. However, isothermal heating in the vacuum furnace at 1000°C for 3 hours produced Nb, Nb_5Si_3, and the metastable cubic phase Nb_3Si. This observation is similar to the results of Bhattacharya et al. who observed the presence of additional phases at temperatures as high as 1050°C in nanolaminates of Nb and codeposited Nb_5Si_3 [1].

Only after 3 hours at 1200°C is the metastable Nb_3Si phase eliminated in the current microlaminates. The discrepancy that Nb_3Si appears after the 1000°C isothermal heat treatments but not after the abbreviated DTA scans to 900°C may be due partially to differences in heating rates. Additionally, since the DTA the samples were not held at temperature for an extended period of time, metastable Nb_3Si grains may have nucleated during the crystallization exotherm, but may have lacked the time and temperature to grow to a sufficient size or volume fraction to be detected by standard x-ray diffraction methods. In contrast to these results for microlaminate foils, Mendiratta and Dimiduk found that extended heat treatments at 1500°C were necessary to transform the metastable Nb_3Si phase to the stable Nb_5Si_3 phase in cast buttons and rapidly solidified ribbons [6]. The elimination of Nb_3Si at lower temperatures in microlaminate foils may be attributable to the finer microstructures and consequently shorter diffusion distances. Additionally, multiple liquid and solid phase transformations are necessary to cast Nb_5Si_3, whereas the transformations in the microlaminate foils occur completely in the solid state.

As previously indicated, the foils deposited with elemental Nb and Si layers delaminated when heated to 1000°C or 1200°C. The delamination was most likely driven by stresses resulting from the densification associated with the solid state mixing of Nb and Si. While the delaminations prevented further study of these foils, deposition from elemental targets may still be a viable option for fabricating Nb/Nb_5Si_3 microlaminates, and has several advantages: the elemental target materials are readily available and inexpensive, and the method can be adapted for e-beam evaporation. Pressing the Nb/Si foils during the heat treatment could prevent delaminations from occurring. Alternatively, Nb/Nb_5Si_3 microlaminates could be fabricated by depositing thick layers of Nb sandwiched between thin layers of Nb and Si. This technique was utilized by Bhattacharya et al., who sputter deposited a Nb layer followed by a thin

nanolaminate of Nb and Si [1]. Intact Nb/Nb_5Si_3 nanolaminates were formed in this case after a high temperature heat treatment.

The delaminations that plagued the Nb/Si foils during the heat treatments were not seen in the foils containing amorphous silicide layers. In these foils, the majority of the densification associated with mixing Nb and Si occurred during the deposition, thereby reducing stresses in subsequent heat treatments. The silicide layers were formed either by codeposition from elemental targets or by deposition from a polycrystalline Nb_5Si_3 target. Codeposition of the silicide layers from elemental targets has all of the advantages listed above for fabricating Nb/Si laminate foils, including the ability to be adapted to e-beam evaporation techniques. However, to ensure the stoichiometry of the silicide layers, the deposition rates from the Nb and Si targets must be controlled precisely. Depositing Nb-Si layers from a polycrystalline Nb_5Si_3 target fixes the stoichiometry of the silicide layer and thereby simplifies the fabrication process. While polycrystalline targets of Nb_5Si_3 are expensive and can not be used during e-beam evaporation (due to the large differences in the vapor pressure of Nb and Si) they are favored for sputter deposition of amorphous Nb-37.5at%Si layers. Since similar microstructures were obtained for foils deposited from either elemental or polycrystalline targets, all of the samples for mechanical evaluations were deposited using a polycrystalline Nb_5Si_3 target.

After heat treating at 1200°C for 3 hours, the layering of the microlaminates remained intact with limited grain boundary grooving at the interfaces between the Nb and Nb_5Si_3 layers (Figure 2. 4(b)) . Furthermore, there was no discernible change in volume fraction or position of the Nb and Nb_5Si_3 phases. This suggests that the equilibrium phases and their morphologies are relatively stable on heating to and cooling from 1200°C. In comparison, when $Nb/MoSi_2$ microlaminates where heated to 800°C,

multiple silicide phases formed and the laminate structure was eliminated [7]. Similarly, Nb/Nb_3Al and $Nb(Cr)/Cr_2Nb$ microlaminates developed intermetallic phases in the metal layers and the layering broke down at temperatures of 1000°C and 1200°C, respectively [8].

According to the Nb-Si equilibrium phase diagram, approximately 0.5 wt.%Si is soluble in Nb at 1200°C and decreases to a negligible value at room temperature [5]. Thus, Nb_5Si_3 precipitates could appear in the Nb layers on rapid cooling. However, no silicide precipitates were observed in the Nb layers at room temperature and the amount of Si in the Nb layers was below the detection limit of the EDS system used to examine the thicker Nb layers. The stability of the Nb/ Nb_5Si_3 microlaminates is due in part to the lower solubility of Si in Nb, as compared to the Nb-Al and Nb-Cr systems.

2.3 Reactive Formation of Microlaminates

2.3.1 Introduction to Self-propagating Exothermic Reactions

Niobium silicides, molybdenum silicides, and other refractory metal silicides are typically fabricated by alloy casting and pressure assisted sintering of prealloyed powders. However, more recently, other routes such as Self-propagating High-temperature Synthesis using elemental powders have been investigated [9]. These exothermic powder-based compact reactions offer much in terms of a simple and inexpensive fabrication route, yielding materials with very favorable high temperature properties. Similar exothermic reactions can also be ignited in sputter deposited multilayer foils [10-16]. The goal of this research was to investigate self-propagating formation reactions in Nb/Si multilayers and to demonstrate the feasibility of shaping

high temperature metal/silicide microlaminate foils by reacting foils that initially have a finer nanolaminate geometry.

While sputtered foils are more expensive to produce than elemental powders, they have a number of advantages over powder compacts that include fully dense products, minimal contaminants, and a high degree of control over the ratio of elements to be mixed [10,11]. The formation reactions, schematically shown in Figure 2.5, can be started with a small spark. Note that as the reaction propagates down the foil, atoms diffuse normal to the layers and heat diffuses parallel to the layers. This planar geometry simplifies both modeling and analysis compared to powder-based reactions. The speed with which an exothermic reaction propagates along a multilayer foil can range from ~0.1m/sec to ~50m/sec, and the maximum temperatures can reach well above 1000°C [10,11]. Self-propagating formation reactions can be engineered in multilayers in a number of ways. Decreasing the thickness of each layer decreases the diffusion distance, which in turn increases the reaction velocity. Premixing at the interfaces between the alternating layers, either as a result of fabrication or annealing, lowers the total heat available. This can have a drastic effect at small periods where the thickness of the intermixed layer can be a significant fraction of the multilayer period. In such cases the final reaction temperature is lower and the reaction velocity decreases [10,11]. The atomic ratio of the constituents determines the heat of the reaction and therefore yields an approximation of the maximum reaction temperature. It also determines the equilibrium phases obtained in the final product. All of these variables offer handles by which the reactions can be steered and tailored to suit the needs of future fabrication processes.

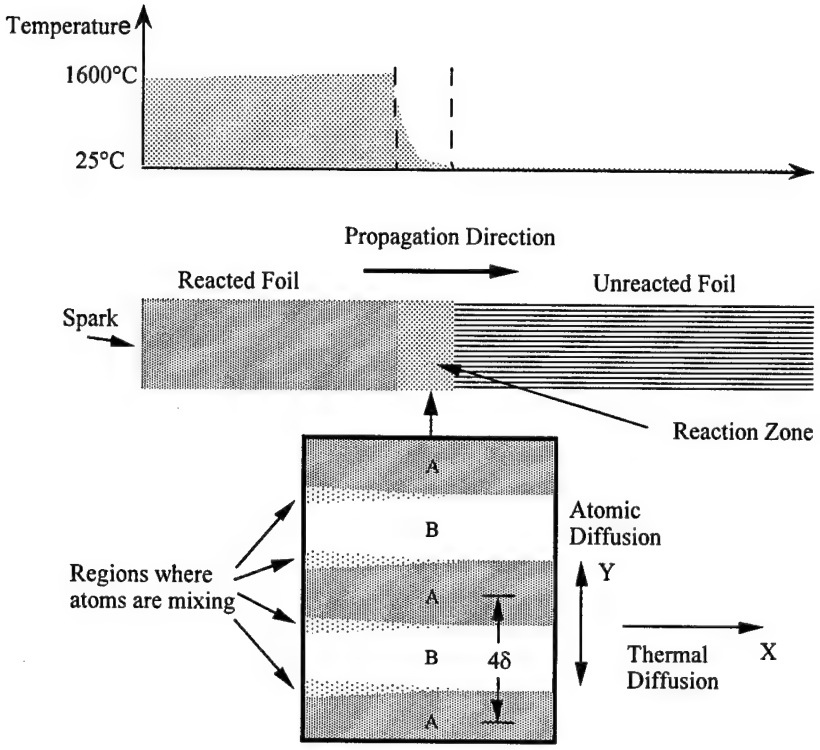

Figure 2. 5: A composite representation of a self-propagating reaction in a multilayer foil. The middle figure is a cross-sectional view of the reacting foil. The reaction was started at the left end of the foil and is propagating left to right. The elements in the alternating layers mix in a small region termed the reaction zone that is shown in detail in the bottom figure. The upper figure is a likely temperature profile as the reaction progresses down the foil.

Fabricating a structural silicide from a reactive multilayer foil must include some method of obtaining a final shape. Depositing foils with a complex geometry can be difficult using line-of-sight deposition processes. However, since the foils reach very high temperatures as they react, they become soft enough to shape with limited pressures. Barbee and Weihs reported the ability to form net shape intermetallic structures using metal/metal multilayer systems [10]. Here we attempt to show that Nb/Si foils can also be shaped into complex geometries when they are reacted. Further still we attempt to characterize the self-propagating formation reactions in these foils to demonstrate that the reactions can be tailored in order to control the rapid forming of structural silicides.

2.3.2 Processing and Characterization of Reactive Multilayer Foils

Nb/Si multilayers were fabricated by magnetron sputtering from high purity Nb and Si targets. The deposition rates from each gun were chosen such that after the Nb/Si multilayers reacted they would contain excess Nb with a *volume* ratio of 1 Nb to 2 Nb_5Si_3. Given the appropriate densities this yields an average composition of 26 at% Si. Four samples were fabricated with different multilayer periods: 39nm, 78nm, 156nm, and 312nm, but all foils had the same total thickness of 25μm. The smallest period films had more than 640 individual layers, while the largest period films had only 80 layers. During deposition the substrates were dithered over the sputter guns to enhance uniformity in thickness. Before multilayer deposition, a film of Cu was deposited onto the Si wafers to facilitate removal of the Nb/Si multilayers. After deposition the Cu was etched in nitric acid, leaving freestanding Nb/Si multilayer foils. Symmetric X-ray diffraction scans were performed on both the unreacted and reacted material to verify the phases present.

The velocities of the self-propagating formation reactions were measured using visible radiation emitted by the foils while they were at high temperature. The foils were ignited at one end by a spark from a simple 12-volt DC adapter (see Figure 2.6). As the reactions propagated down the length of the foils, emitted light was collected by a linear array of fibers that were separated from the foils by a thin piece of glass. The glass served to protect the fibers while still allowing close proximity to the foils. The fibers formed a circular bundle at the end that was furthest from the reaction. The light from the circular bundle was directed onto a Si PIN photodiode whose output was recorded by a digitizing oscilloscope.

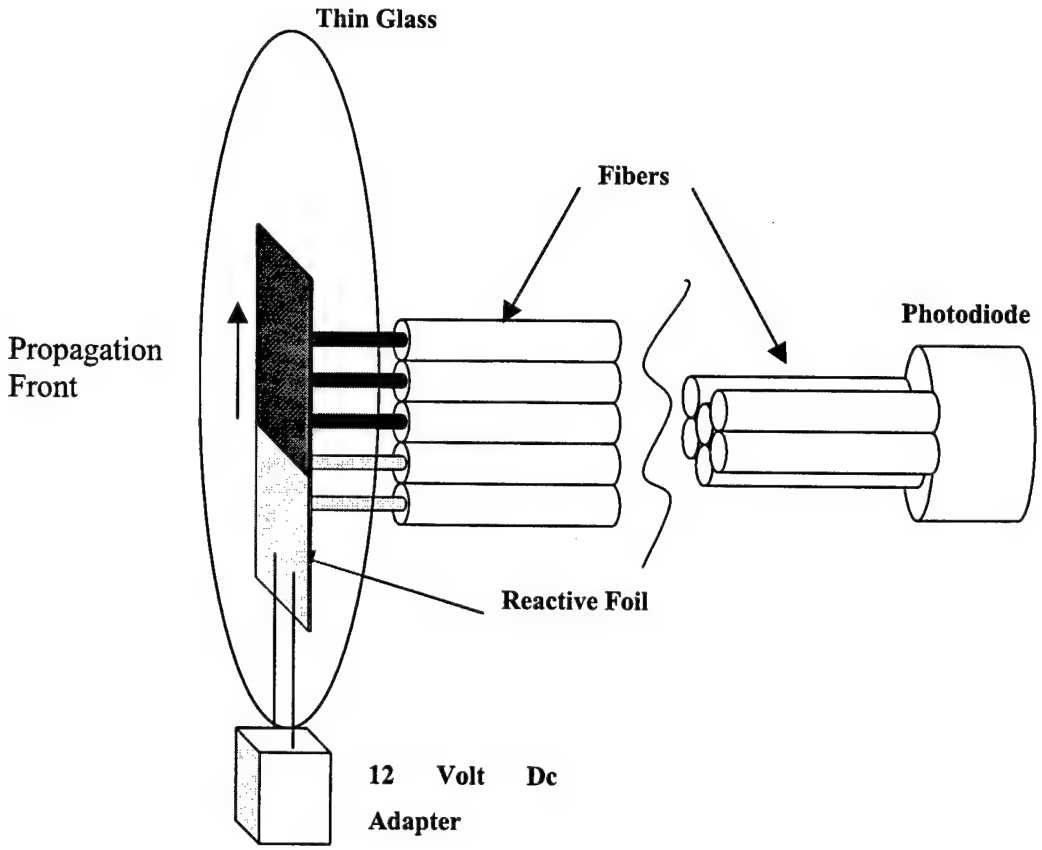

Figure 2. 6: This figure depicts the arrangement of the various components in the velocity measurement setup. A spark from the 12-volt adapter is used to ignite the foil. The array of fibers carries light to the photodiode. The array is created by stripping the buffer layers off the ends of the fibers and placing the fibers side by side so that fiber with buffer defines the spacing between fibers. The thin glass serves as a substrate to which the foil is taped and it protects the fibers from the reacting foils.

With the fibers spaced tightly, the resulting plots of intensity versus time had the staircase or stepped appearance seen in Figure 2. 7. If the fibers were sufficiently far apart, cooling behind the reaction front caused drops in intensity and a saw tooth pattern appeared. However, since configuring the experiment to yield a step trace allowed for significantly smaller sample sizes (2mm by 5mm strips), the majority of the data was collected in this manner. Once a foil was ignited and the emitted light was collected as a step trace, the velocity of the self-propagating reaction was quantified by determining the time between steps. The zero crossings of the second derivative of the step trace

provided an accurate and repeatable method of measuring the average time it took the reaction to traverse the distance between the fibers. The velocity was then calculated by dividing the distance between the fibers by the average time of travel.

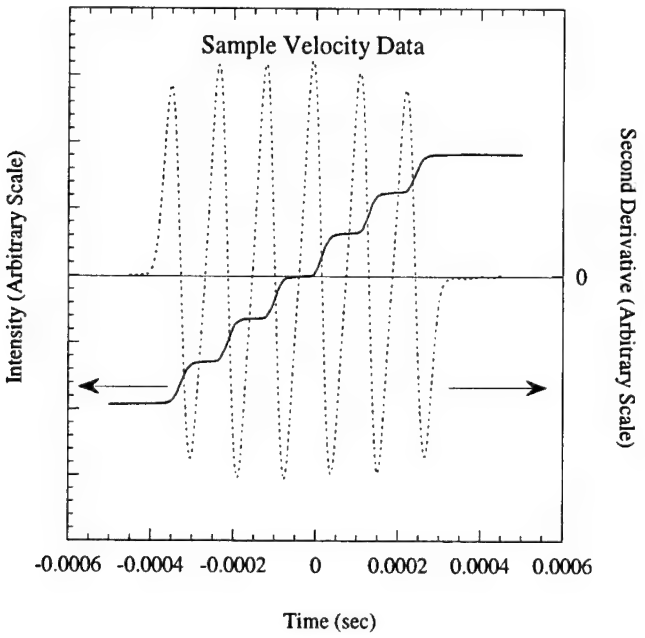

Figure 2. 7: The step trace in this figure is a representative data set that was acquired with the velocity measurement system. The dotted-line overlay is the second derivative of this trace. A zero crossing with a negative slope indicates the time at which the reaction front reached the center of a fiber. Averaging the elapsed time between these points and dividing by the separation distance yields velocity.

While the above method provided a reliable means for measuring reaction velocities we should note that the foils densified as they reacted causing wrinkling and shortening. This densification proved to be problematic in determining the difference between velocity in space and velocity in multilayer coordinate. In general, the foils changed shape by shortening along their length, in the direction of propagation. This could be noted by striations perpendicular to that direction. To minimize movement of the samples during their reaction, they were fixed to a glass substrate using thin strips of cellophane tape. The tape was placed along the outermost 0.5mm of the long edges of the samples. Strips of tape were also attached similarly to the bottom face of the sample.

The tape-foil-tape sandwich was then fixed to the glass substrate. This combination of tape raised the foil off the glass surface just enough to provide an escape route for air that was heated underneath the foil as it reacted. This sample geometry eliminated a significant pressure increase underneath the foil and avoided out-of-plane deformations of the foil. While suppressing contractions in length with tape may have some effect on the true reaction velocity by introducing stresses in the foil, the foils have little strength at their high reaction temperature (>1500°C), so any stresses are expected to be small.

To demonstrate that the foils soften enough to shape when they are reacted, a sample was cut into a circular geometry and mounted onto a glass substrate with tape. In this case all edges of the foil were sealed to the glass substrate in order to trap the air that is heated between the foil and the substrate. The multilayer was then ignited with a spark at one end, heating the trapped air as it reacted. Order of magnitude calculations concerning stress, strain, and strain rate were performed based on the gross shape changes observed between the unreacted and reacted foils.

2.3.3 Results and Discussion for Reactive Multilayer Foils

The results of the symmetric X-ray diffraction scans indicate that the unreacted foils are comprised of Nb and amorphous Si (Figure 2.8). The fact that the Si is amorphous is significant in that the total heat released as the foils react will be the sum of the heat of formation of Nb_5Si_3 in a Nb-rich matrix as well as the heat of crystallization of the amorphous Si. This yields a higher final temperature than predicted from just Nb_5Si_3's heat of formation. Once reacted, the foils proved to be predominantly Nb_5Si_3 and Nb as shown by the second XRD trace in Figure 2.8. However, there also appeared to be a small percentage of Nb_3Si, which is a metastable compound at room temperature.

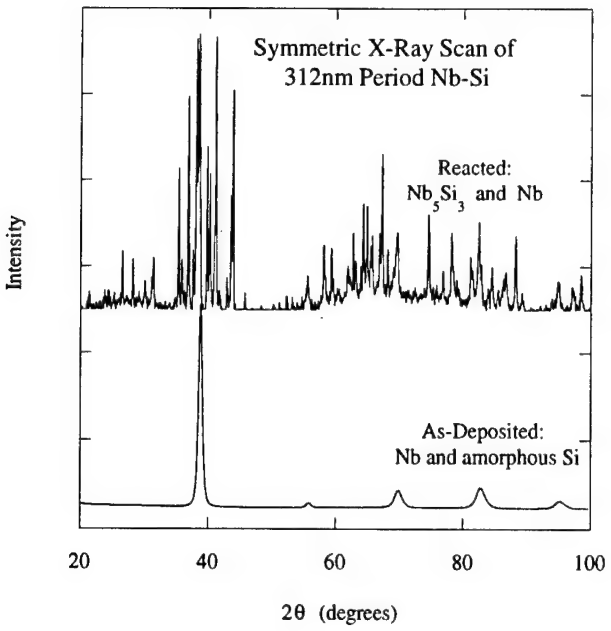

Figure 2. 8: This graph shows results from two symmetric X-ray scans. The peaks in the lower scan correspond to textured Nb in the as-deposited Nb-Si multilayer. The peaks in the upper scan correspond primarily to Nb and reacted Nb_5Si_3. Several small peaks do appear that correspond to a metastable compound, Nb_3Si.

Velocity data was compiled for all four samples from traces of relative intensity versus time (see Figure 2.7). Using end-point-smoothing routines where appropriate, the second derivative of the stored traces provided a consistent method of determining the time of flight for each sample. The measured velocities are plotted in Figure 2. 9. As expected, the values are much lower than the velocities that Clevenger et al. [14] measured for Ni/Si multilayers. The presence of excess Nb in these samples reduces the maximum possible reaction temperature and therefore slows the speed of the reaction. However, the important observation one can make in Figure 2. 9 is that reaction velocity decreases smoothly as multilayer period increases. While this trend has been observed in metallic multilayer systems [10,11,15,16], it was not observed in studies on Rh/Si [12], Zr/Si [13]], or Ni/Si [14] multilayers. The consistent decrease of reaction velocity with

individual layer thickness demonstrates that the speed of these reactions can be controlled and predicted for shape forming applications.

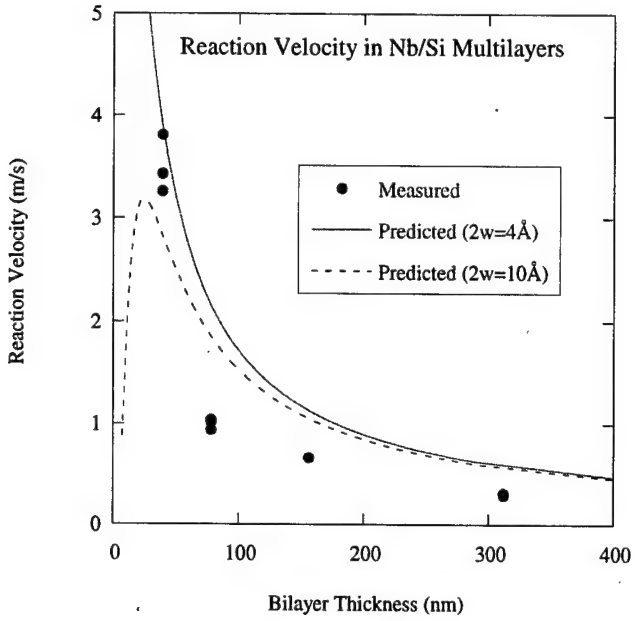

Figure 2. 9: Reaction velocity is plotted versus multilayer period. The fitted curves represent velocities that were predicted using the model derived by Mann et al [19]. 2w represents the thickness of the chemical intermixing between each Nb and Si layer in the as-deposited multilayers. Note that intermixing as thin as 1nm would produce a noticeable drop-off in velocity at small periods which was not observed in these samples.

The drop in reaction velocity with multilayer period in Figure 2. 9 conforms to relationships that Armstrong [17,18] predicted using a model for reactive multilayers with chemically distinct layers. He used one-dimensional thermal and mass transport equations to obtain his predictions. He also treated the chemical profiles across the thickness of the multilayers as ideal step functions. Mann et al. [19] derived similar equations to predict velocity as a function of period, but they allowed for non-ideal interfaces between the layers. By doing so they took into account the loss of heat due to premixing during fabrication. Qualitatively, their model predicts that velocity is

inversely proportional to multilayer period at large periods. This relationship holds until the layers become thin enough that the loss of heat due to premixing is significant. From that point the velocity drops off rapidly with decreasing period. (Similar trends have been predicted in more recent numerical studies [20]). A drop in velocity at small multilayer period does not appear to be present in these samples, indicating that intermixing at the Nb/Si interfaces is much smaller than the smallest period tested of 39nm. Thus, for these samples either analytical model could be used to predict reaction velocities when attempting to shape the foils as they react.

The feasibility of shaping Nb/Si multilayer foils as they react is demonstrated by the SEM image of a simple bubble in Figure 2.10. The Nb/Si foil in this image was deposited flat with a 39nm period and it was shaped by trapped air when it was reacted on a glass substrate. The air that was trapped between the foil and the glass was heated during the reaction, raising its pressure and thereby forcing the foil to deform as it softened. Note that the reacted foil has a smooth surface, void of cracks or holes. Thus, it appears to have deformed in a continuous manner with no obvious instabilities or discontinuities. The major ripples along its edges are thought to have been generated by lift-off of the tape at the foil's perimeter and a loss of constraint. These regions provided escape routes for some of the trapped air. Given the foils period of 39nm, we can predict that its exothermic reaction propagated across the sample at ~ 3.5m/s. Since the sample had a circular geometry and a 7.5mm diameter, the reaction propagated across the complete sample in approximately 2msec. Based on the intensity of the light emitted during the velocity measurements we know that the sample remains near or above 1500°C for nearly 30msec. Thus, the whole sample was heated rapidly in comparison to the time that it spent at high temperature. Knowing the change in sample geometry, the reaction velocities, heating times, and cooling times, we can make simple estimates of the stresses, strains and strain rates for the resulting plastic deformation.

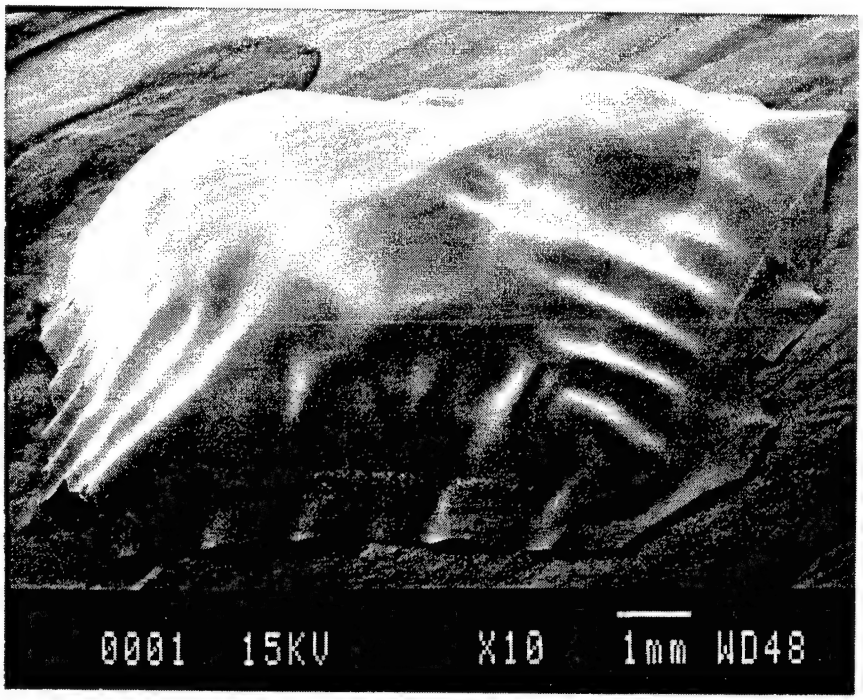

Figure 2. 10: An SEM image of a Nb/Si foil that was plastically deformed as it reacted. The edges of the foil were initially secured to a glass substrate with tape. After ignition the air trapped between the foil and the glass heated and rose high enough in pressure to expand the foil. Note that while the foil did not crack, air did escape at various points around its edges.

To evaluate the upper bounds for the stresses and strains present, the reaction is divided into two stages. The first stage is the initial bulge, an ideal situation in which the air is fully heated but the foil has just begun to deform. This stage will yield the maximum biaxial stress that can be applied to the foil. The second stage is the final bulge, a state in which the gas is still hot but the foil is cooling and losing its ability to deform easily. This stage will yield the maximum plastic strain that has been imparted to the foil. For the initial bulge stage, the Ideal Gas Law was used to approximate the maximum possible increase in pressure as the trapped gas is heated. Assuming a constant volume and a 1500°C change in temperature, the pressure of the trapped air could reach as high as 0.4MPa. Using an equation for thin film bulge tests [21] and a small initial

deflection of 0.1 mm, this pressure converts to a biaxial stress of approximately 5MPa. Although the change in geometry is out of the plane of the film, the stress can still be considered biaxial. While 5MPa is at best a gross estimate, it does provide an upper bound for the stress in the foil that will decay as the foil deforms.

The final plastic strain in the foil was estimated to be 15% based on the geometric changes of the originally flat foil. This value for strain was approximated by considering the change in line length of the original radius of the flat sample. The new line length was an arc from the center of the resulting spherical section, to its edge. An average plastic strain rate for the deformation was then calculated by dividing the plastic strain by the total time the foil retains a temperature near to or greater than 1500°C and is therefore soft enough to deform under small applied stresses. This simple estimate yields a very high plastic strain rate of 5 sec^{-1}. Additional experiments are needed to measure the applied pressures and the resulting deformations during the rapid formation reactions. Such measurements would enable one to examine the mechanisms that control deformation in the foils under these highly nonequilibrium conditions. This information will be critical to the development of shape forming of structural silicides from reactive multilayer foils.

2.4. Conclusions for Processing of Microlaminates

The results suggest that strong Nb/ Nb_5Si_3 microlaminates can be fabricated using magnetron sputtering and high temperature heat treatments. The most promising as-deposited structures consist of crystalline Nb layers and amorphous Nb-Si layers. During a 1200°C heat treatment, the silicide layers crystallize into Nb_5Si_3 and the layering

remains intact with distinct and flat interfaces. The heat treated foils have nearly equiaxed grains of Nb and submicron equiaxed grains of Nb_5Si_3. The gross microstructure of the laminate is not columnar and growth defects are not present, both of which can degrade mechanical properties.

Formation reactions have been shown to self-propagate in Nb/Si multilayers with nanoscale layers and an average composition of 26 at% Si. The velocities of the reactions were found to decrease smoothly from approximately 4m/s to 0.5m/s as the period of the Nb and Si layers increased from 39nm to 312nm. The final reaction product was predominantly Nb and Nb_5Si_3. To demonstrate that these foils can be shaped as they react, a circular foil was constrained on a glass substrate and then pressurized by the air trapped between the foil and the glass. The pressurized air forced the foil to plastically strain as much as 15% at a rate as high as 5 sec^{-1}. This simple experiment demonstrates that Nb/Si foils have the potential to be shaped as they react to form complex geometries for future, high-temperature structural applications.

2.5. References for Section 2

1. R. S. Bhattacharya, A. K. Rai, M. G. Mendiratta, and Y. T. Cheng: *Intermetallic Matrix Composites, Mat. Res. Soc. Symp. Proc.*, San Francisco, CA, Materials Research Society, Pittsburgh, PA, 1990, vol. 194, pp. 71-78.

2. S. P. Rawal, G. M. Swanson, and W. C. Moshier: *J. Mater. Res.*, **10** (1995), 1721.

3. H. Cao, J. P. A. Löfvander, A. G. Evans, R. G. Rowe, and D. W. Skelly: *Mater. Sci. Eng.*, **A185**, (1994), 87.

4 D. Josell, D. Van Heerden, D. Read, J. Bonevich, and D. Shechtman: *J. Mater. Res.*, **13**, (1998) 2902.

5. M. G. Mendiratta and D. M. Dimiduk: *Scripta Metall. Mater.* , **25**, (1991) 237.

6. M. G. Mendiratta and D. M. Dimiduk: *High Temperature Ordered Intermetallic Alloys III, Mat. Res. Soc. Symp. Proc.*, Boston, MA, Materials Research Society, Pittsburgh, PA, 1989, vol. 133, pp. 441-446.

7. T. C. Chou, T. G. Nieh, T. Y. Tsui, G. M. Pharr, and W. C. Oliver: *J. Mater. Res.*, **7**, (1992) 2765.

8. R. G. Rowe, D. W. Skelly, M. Larsen, J. Heathcote, G. Lucas, and G. R. Odette: *High Temperature Silicides and Refractory Alloys, Mat. Res. Soc. Symp. Proc.*, Boston, MA, Materials Research Society, Pittsburgh, PA, 1994, vol. 322, pp. 461-472.

9. Z. A. Munir and J. B. Holt, eds., Combustion and Plasma Synthesis of High-Temperature Materials, VCH Publishers, NY, 1990.

10. T. W. Barbee, Jr. and T. P. Weihs, U.S. Patent 5,538,795, issued July 23, 1996.

11. T. P. Weihs, chapter in Handbook of Thin Film Process Technology, IOP Publishing, 1998.

12. J. A. Floro, *J. Vac. Sci. Technol. A*, **4** (1986) 631.

13. C. E. Wickersham, Jr. and J. E. Poole, *J. Vac. Sci. Technol. A*, **6** (1988) 1699.

14. L. A. Clevenger, C. V. Thompson, and K. N. Tu, *J. Appl. Phys.*, **67** (1990) 28.

15. T. S. Dyer, Z.A. Munir, and V. Ruth, *Scripta Met.*, **30** (1994) 1281.

16. T. P. Weihs, A. J. Gavens, M. E. Reiss, D. van Heerden, A. Draffin, and D. Stanfield in Chemistry and Physics of Nanostructures, 75-87 (TMS Publishing, 1997).

17. R. Armstrong, *Combust. Sci. and Tech.*, **71** (1990) 155.

18. R. Armstrong, *Met. Trans.*, **23A** (1992) 2339.

19. A. B. Mann, A. J. Gavens, M. E. Reiss, D. van Heerden, G. Bao, and T. P. Weihs, *J. Appl Phys.*, **82** (1997) 1178.

20. S. Jayaraman, A. B. Mann, O.M. Knio, G. Bao, and T. P. Weihs, Vol. 481, Mat. Res. Soc. Symp. Proceedings, edited by M. Atzmon, E. Ma, P. Bellon, and R. Trivedi, Fall 1997.

21. Richard P. Vinci, Joost J. Vlassak, *Annu. Rev. Mater. Sci.*, **26** (1996) 431.

3. Residual Stresses and Bending Stresses in Nb/Nb_5Si_3 Microlaminates

3.1 Introduction

When free-standing Nb/Nb_5Si_3 microlaminates are fabricated several mechanisms can lead to significant residual stresses. First, when the foils are vapor deposited at room temperature, the high effective quench rates and low atomic mobilities inherent to this process can lead to large growth stresses. Second, when the as-deposited microlaminates are annealed at high temperatures, grain growth or phase transformations can result in densification. If this densification is restricted by a substrate or a surrounding layer, significant residual stresses can arise. Lastly, if the adjacent layers in a free-standing microlaminate expand at different rates on heating, thermal stresses can also develop. Since residual stresses can impact the yield and fracture of microlaminates, it is important to characterize them in conjunction with standard fracture tests and tension tests. For mechanical tests such as these, it is also important to assess the flatness of the microlaminate foils. If a foil has even a small curvature after fabrication, bending moments will arise when it is loaded in tension and significant bending stresses will appear. This paper characterizes both residual stresses and bending stresses in Nb/Nb_5Si_3 microlaminate foils at room temperature.

3.2 Sample Preparation and X-ray Characterization

Nb/Nb_5Si_3 microlaminate foils tested here were sputter deposited onto Si wafers near room temperature as alternating layers of polycrystalline Nb and amorphous Nb-Si. Following

deposition the foils were removed from their substrates and then annealed in vacuum (10^{-6} Torr.) at 1200 °C for 3 hours. At the end of each anneal, the samples were furnace cooled to room temperature under vacuum. The temperature of the samples decreased from 1200 °C to 800 °C at approximately 100 °C/min, but decreased more slowly at lower temperatures. The resulting layering and microstructures have been shown earlier in Figure 2.4. Note from the cross-sectional scanning electron micrograph in Figure 2.4(a) that the layers are very flat and distinct following the 1200 °C anneals. The cross-sectional transmission electron micrograph in Figure 2.4(b) shows that the Nb phase has a relatively large equiaxed grain structure that spans the layer thickness, while the Nb_5Si_3 phase has a smaller equiaxed grain structure with an average diameter near 0.3 μm. For this study we selected two samples. Both foils contained a total of 51 layers: twenty-six 1μm layers of Nb and twenty-five 1μm layers of Nb_5Si_3. The first sample was placed flat on the bottom of an alumina crucible for the 1200 °C anneal and showed no signs of curvature following the anneal. The second sample was positioned to lean against the wall of the crucible and due to creep deformation, developed a small curvature along its vertical axis during the anneal.

To quantify the crystalline texture and planar spacings in the Nb and Nb_5Si_3 layers, we used a four-circle X-ray diffractometer (Philips, X'Pert-MRD), powered at 45 kV and 40 mA. Because the bilayer period of 2 μm is comparable in thickness to the effective Cu K_α penetration depth, most of the scattered X-ray signal comes from the top two layers of the microlaminate. In addition, the intensity of the peaks for the underlying silicide layer will be low because most of the X-rays diffracted by this layer will be absorbed by the outer Nb layer. Figure 3.1 shows the

results of a symmetric X-ray diffraction scan. The data within the inset reveals a very strong out-of-plane <110> texture for the Nb laminates while the multiple smaller peaks for the Nb_5Si_3 phase match predictions for a randomly oriented polycrystalline sample. A pole figure analysis on the same sample revealed a weak two-fold, in-plane texture for the Nb laminates.

3.3 Analysis of Stresses in Microlaminate Foils

The Nb/Nb_5Si_3 microlaminate foils that were examined here are known to possess a limited resistance to creep deformation at 1200 °C, based on preliminary experiments [1]. This surprising result is attributed to the fact that the silicide phase has a very fine grain size (Figure 2.4(b)) and therefore is susceptible to Coble creep. Assuming both the Nb and Nb_5Si_3 layers can deform easily at 1200 °C, the individual layers are expected to relax during the three hour anneals at this temperature, thereby reducing the growth stresses and any residual stresses that appeared on heating to 1200 °C. However, on cooling to room temperature, residual stresses can develop again due to the mismatch in the thermal contraction of the Nb and Nb_5Si_3 layers.

The average coefficient of thermal expansion (CTE) on cooling from 1200 °C to room temperature is 8.5×10^{-6} K^{-1} for Nb and it is 6.3×10^{-6} K^{-1} for Nb_5Si_3 [2,3]. (Note: the CTE for Nb_5Si_3 is averaged over its volume given this phase is tetragonal.) Thus, when cooling these free-standing microlaminates, the Nb layers will want to contract more than the silicide layers and therefore will develop tensile stresses while the silicide layers will develop compressive stresses. Because temperature decreases rapidly from 1200 °C to 800 °C after annealing, the individual

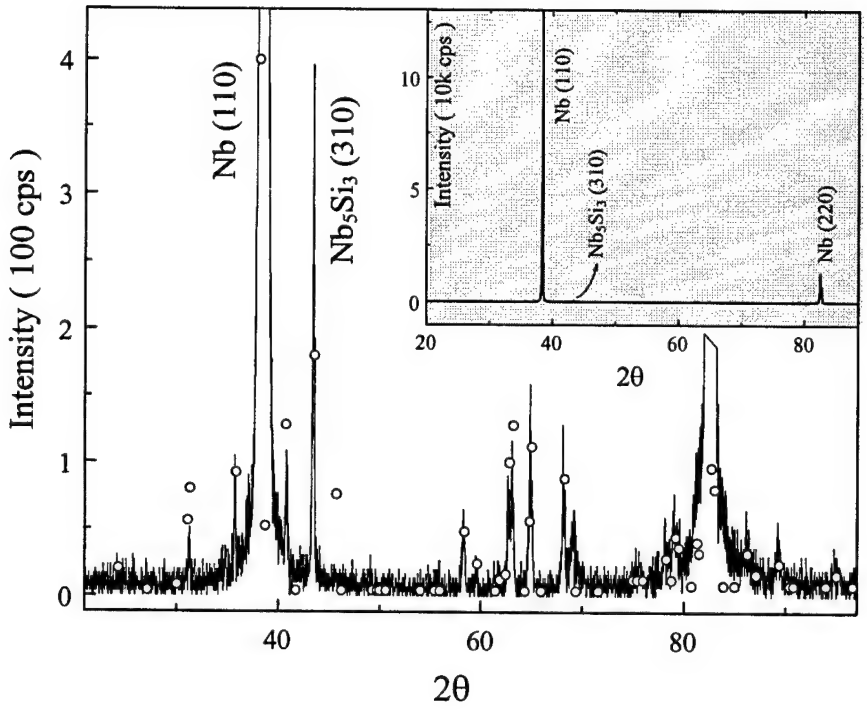

Figure 3.1: Symmetric X-ray diffraction scan for a Nb/Nb_5Si_3 microlaminate after heat treatment at 1200°C for 3 hours. The inset is an overview, indicating strong <110> out-of-plane texture for Nb. Phase identification reveals that except for the two strong Nb peaks indicated in the inset, all other peaks come from the tetragonal Nb_5Si_3. Open circles show the predicted peak positions and relative heights for the Nb_5Si_3 of random orientations. Note that some Nb_5Si_3 diffraction peaks, including the strongest one located at $2\theta = 38.1°$, cannot be seen because they overlap with the Nb peaks.

layers will have little time to relax via creep mechanisms. Thus, the thermal stresses that are induced on cooling are likely to persist. Assuming there is no relaxation on cooling, one can estimate the final residual thermal stresses for a free-standing microlaminate with layers of equal thickness. Using the equilibrium condition:

$$M_1\varepsilon_1 + M_2\varepsilon_2 = 0 \tag{3.1}$$

where M_i and ε_i are the biaxial modulus and biaxial strain for layer *i*, and using the linear thermal expansion term, $k_i = \alpha_i \Delta T$ where α_i is the CTE for layer i and ΔT is the change in temperature, the residual thermal stress, σ^{th}, is predicted to be

$$\sigma^{th} = \frac{(k_1 - k_2) M_1 M_2}{M_1(1+k_1) + M_2(1+k_2)} \tag{3.2}$$

For the isotropic Nb_5Si_3 layer, M_{Nb5Si3} was calculated to be 409 GPa using $M_{Nb5Si3} = E/(1-\nu)$, E=327 GPa [4] and ν=0.2 [5]. For the Nb layer, an average value of M_{Nb} was calculated by neglecting the minor in-plane crystallographic texture and integrating M_{Nb} over all possible in-plane orientations [6],

$$M_{Nb} = \frac{1}{2\pi} \int_0^{2\pi} \left[\frac{2s_{11} + 6s_{12} - s_{44}}{4} + \left(\frac{s_{44}}{2} + \frac{2s_{11} - 2s_{12} - s_{44}}{4} \sin^2 \phi \right) \right]^{-1} d\phi$$

$$M_{Nb} = 2 / \sqrt{(s_{11} + s_{12})(2s_{11} + 6s_{12} + s_{44})} \tag{3.3}$$

Using s_{11}=6.56 $(TPa)^{-1}$, s_{12}= -2.29 $(TPa)^{-1}$, and s_{44} = 35.2 $(TPa)^{-1}$ [7], M_{Nb} = 164.6 GPa. By substituting the appropriate values of M, α and ΔT into Equation (3.2), the thermal stresses are predicted to be ± 300 MPa on cooling from 1200 °C.

The actual residual stresses, σ, in the individual Nb and Nb_5Si_3 layers were quantified using X-ray diffraction techniques. The spacings of specific sets of crystallographic planes were measured [8], and elastic strains were calculated by comparing the measured planar spacings (*d*) with the strain-free lattice spacings (d_0). We then used the appropriate elastic constants to calculate the residual stresses. The particular analysis that was used, though, depended on

whether the individual layers can be treated as elastically isotropic or elastically anisotropic solids.

3.3.1. The Nb_5Si_3 Layers – Elastically Isotropic Solids

The silicide layers in the microlaminates have a fine-grained structure that is randomly oriented as shown in Figure 2.4(b). Thus, even though the Nb_5Si_3 crystals are each elastically anisotropic, the silicide layers themselves can be treated as an isotropic solid. Starting with the assumption of an equal biaxial stress state, one can obtain an equation for strain at an angle ψ relative to the sample normal as shown in Figure 3.2(a),

$$\varepsilon_\psi = \frac{d_\psi - d_0}{d_0} = \frac{1+\nu}{E}\sigma \sin^2\psi - \frac{2\nu\sigma}{E} \qquad (3.4)$$

where σ, E and ν are residual stress, Young's Modulus and Poisson's ratio, respectively. This is the well-known d-$\sin^2\psi$ equation for isotropic materials [8]. Note that the lattice spacing d_ψ varies linearly with $\sin^2\psi$ and that the strain-free planar spacing, d_0, can be found at $\sin^2\psi_0 = 2\nu/(1+\nu)$. Equation (3.4) can be used to determine the in-plane strains in the silicide layers at $\psi = 90°$. Using this strain and the biaxial modulus, M_{Nb5Si3}, the residual biaxial stress, σ, is obtained. However, if uniaxial bending is present in the layers and the stress state is not equal-biaxial, the above equation must be re-derived using a modified stress state as described earlier by Noyan and Cohen [8].

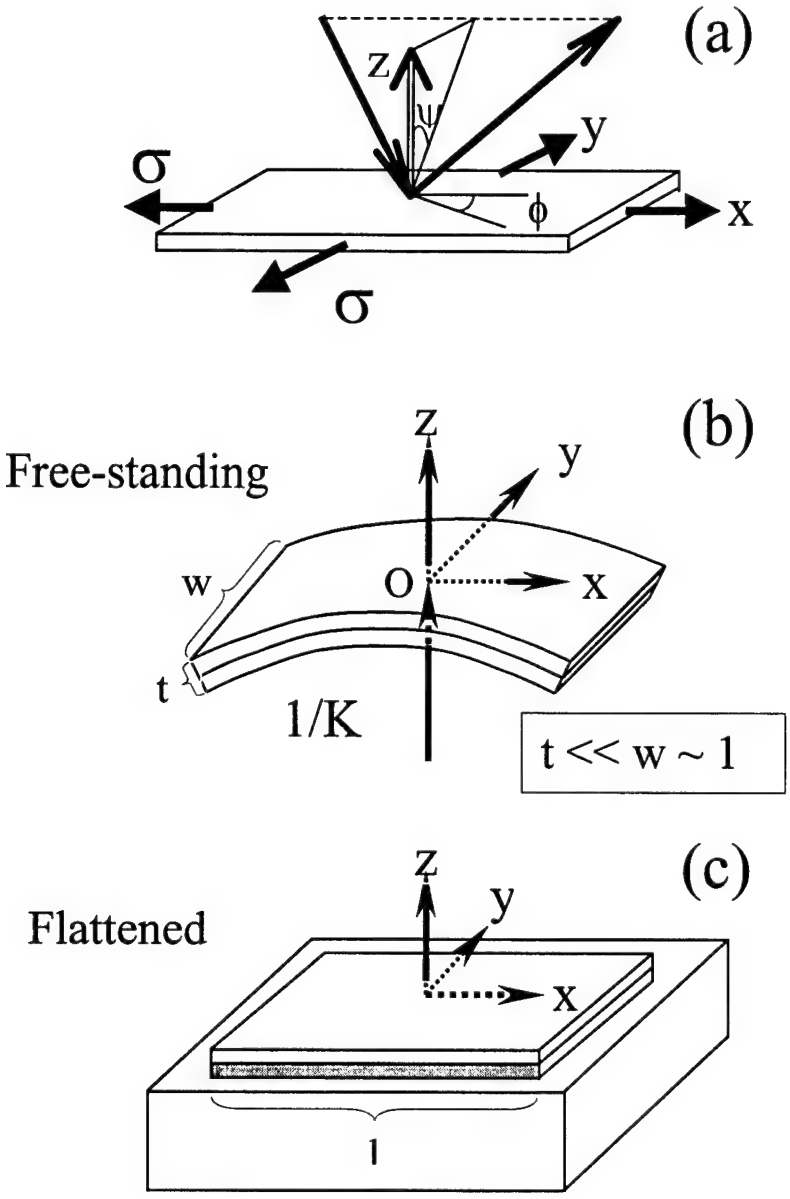

Figure 3.2: Schematic plot showing (a) diffraction geometry for asymmetric X-ray stress analysis, (b) a curved, free-standing microlaminate foil, and (c) the sample flattened for an X-ray diffraction study (b). The coordinate system originates at the middle of the sample with x aligned along the bending axis and z through the thickness.

To characterize stress in the presence of bending moments, we begin by assuming that we have a free-standing beam with a curvature K as shown in Figure 3.2(b) and equal but opposite

thermal stresses in each of the layers. Furthermore, we assume that the beam is flattened elastically for an X-ray analysis as indicated in Figure 3.2(c). Given this elastic deformation, a uniaxial bending stress σ^b will develop along the x-axis of the beam. An additional uniaxial stress will also develop along the y-axis because the Poisson's strain in the *y* direction will be inhibited by the fact that the beam is much wider than it is thick. These bending stresses will simply add to the equal-biaxial residual stress, σ. The full stress state is given by,

$$\begin{cases} \sigma_x = \sigma + \sigma^b \\ \sigma_y = \sigma + \nu\sigma^b \\ \sigma_z = 0 \end{cases} \tag{3.5}$$

The elastic strain in any direction (ϕ,ψ) can be given as a sum of the principal strains in the x, y, and z directions, using the appropriate direction cosines,

$$\varepsilon_{\phi\psi} = a_x{}^2\varepsilon_x + a_y{}^2\varepsilon_y + a_z{}^2\varepsilon_z \tag{3.6}$$

where $a_x = \sin\psi\cos\phi$, $a_y = \sin\psi\sin\phi$, $a_z = \cos\phi$. The principle strains can be related to the applied stress state using the isotropic form of Hooke's law,

$$\begin{cases} \varepsilon_x = \dfrac{1}{E}\left[\sigma_x - \nu(\sigma_y + \sigma_z)\right] \\ \varepsilon_y = \dfrac{1}{E}\left[\sigma_y - \nu(\sigma_z + \sigma_x)\right] \\ \varepsilon_z = \dfrac{1}{E}\left[\sigma_z - \nu(\sigma_x + \sigma_y)\right] \end{cases} \tag{3.7}$$

By substituting Equations (3.5) and (3.7) into Equation (3.6), we obtain,

$$\varepsilon_{\phi\psi} = \frac{1+\nu}{E}\left[\sigma + \sigma^b(\cos^2\phi + \nu\sin^2\phi)\right]\sin^2\psi - \frac{\nu}{E}\left[2\sigma + (1+\nu)\sigma^b\right] \tag{3.8}$$

Equation (3.8) is similar to the one obtained by Noyan and Cohen [8] and shows that when bending stresses are present, the strain $\varepsilon_{\phi\psi}$ is dependent on the in-plane angle ϕ. Along the bending axis at $\phi = 0$, we obtain,

$$\varepsilon_{\phi\psi}\Big|_{\phi=0} = \frac{1+\nu}{E}\left(\sigma + \sigma^b\right)\sin^2\psi - \frac{\nu}{E}\left[2\sigma + (1+\nu)\sigma^b\right] \tag{3.9}$$

and the zero-strain lattice plane is located at,

$$\sin^2\psi_0 = \frac{\nu}{1+\nu}\frac{2\sigma + (1+\nu)\sigma^b}{\sigma + \sigma^b} \tag{3.10}$$

Note that strain and $d_{\phi\psi}$ still vary linearly with $\sin^2\psi$ in Equation (3.9) and this equation reverts to Equation (3.4) if $\sigma^b = 0$.

3.3.2 The Nb Layers – Elastically Anisotropic Solids

Unlike the Nb_5Si_3 laminates, the Nb layers have a very strong <110> fiber texture as shown in Figure 3.1. Thus, the stresses in these layers cannot be quantified using an isotropic analysis. Instead we follow the procedure that was detailed by Clemens and Bain [6] for studying stresses in textured thin films. They utilized an elastic analysis for single crystals and applied it to textured thin films. For the case of a cubic thin film with a <110> out-of-plane fiber texture, the strain under equal biaxial stress conditions is given by,

$$\hat{\varepsilon}_{\phi\psi}^{n//[110]} = \frac{d_{\phi\psi} - d_0}{d_0} = \sigma\left[\frac{2s_{11} + 6s_{12} - s_{44}}{4} + \left(\frac{s_{44}}{2} + \frac{2s_{11} - 2s_{12} - s_{44}}{4}\sin^2\phi\right)\sin^2\psi\right] \tag{3.11}$$

where the s_{ij}'s are the compliances for the material under study. Note in Equation (3.11) that the measured strain, $\varepsilon_{\phi\psi}$, depends on the in-plane angle ϕ and no longer varies linearly with $\sin^2\psi$. This is because the (110) plane of almost all cubic materials is not isotropic. Thus, when measuring the variation in spacing of a particular plane with the tilting angle ψ, one must be careful to account for the specific ϕ orientation of that plane. In addition, one cannot use a linear variation of d_ψ versus $\sin^2\psi$ to determine the in-plane strain at $\psi = 90°$, as described above for the isotropic analysis. Instead, one can use diffraction data from two specific planes to calculate the in-plane strain as suggested by Clemens and Bain [6]. However, it is desirable to use data from more than two planes in a given family of planes to determine an average value for the in-plane strain.

Here we consider a simple alternative to the procedure of Clemens and Bain [6] that averages over many diffraction planes at once. We begin by noting that all of the terms in the brackets in Equation (3.11) are fixed for a given plane with particular values of ψ and ϕ. If one sets the terms in the brackets equal to κ,

$$\kappa = \left[\frac{2s_{11} + 6s_{12} - s_{44}}{4} + \left(\frac{s_{44}}{2} + \frac{2s_{11} - 2s_{12} - s_{44}}{4} \sin^2\phi \right) \sin^2\psi \right] \tag{3.12}$$

then Equation (3.11) simplifies to,

$$d_{\phi\psi} = d_0 + d_0 \sigma \kappa = A + B\kappa \tag{3.13}$$

Equation (3.13) now yields a linear variation of $d_{\phi\psi}$ versus $\kappa(\psi, \phi)$, and residual stress can be determined using the ratio of the slope to the intercept ($\sigma = B/A$) for the line determined by

Equation (3.13). This methodology allows one to obtain a value of stress that averages over several data points for a given set of diffraction planes. Statistically, it provides a more precise determination of stress than solving for σ using two data points and Equation (3.11).

3.4 Results

3.4.1 Residual Stresses:

Residual stresses were quantified in a free-standing Nb/Nb_5Si_3 microlaminate that showed no signs of curvature after processing at 1200 °C and therefore was assumed to be flat prior to mounting for X-ray analysis. Spacings of {211} Nb planes and {310} Nb_5Si_3 planes were determined from X-ray scans and are plotted versus $\sin^2\psi$ in Figure 3.3. The positive slope in Figure 3.3(a) implies that the Nb layers are in tension, while the negative slope in Figure 3.3(b) implies that the Nb_5Si_3 layers are in compression. This result is consistent with the predictions made earlier for the thermal stresses that can appear on cooling from a high-temperature anneal.

Using the isotropic analysis for the Nb_5Si_3 layers, d_0 was determined to be 0.20806 nm at $\sin^2\psi_0 = 2\nu/(1+\nu) = 0.333$. The in-plane biaxial strain was then calculated at $\psi = 90°$ to be -7.57×10^{-4}. Using the silicide's biaxial modulus of 409 GPa, we determined that the residual biaxial stress for this layer was compressive and equal to -309 MPa. This value is very close to the -300 MPa thermal stress that was predicted for the silicide layers on cooling.

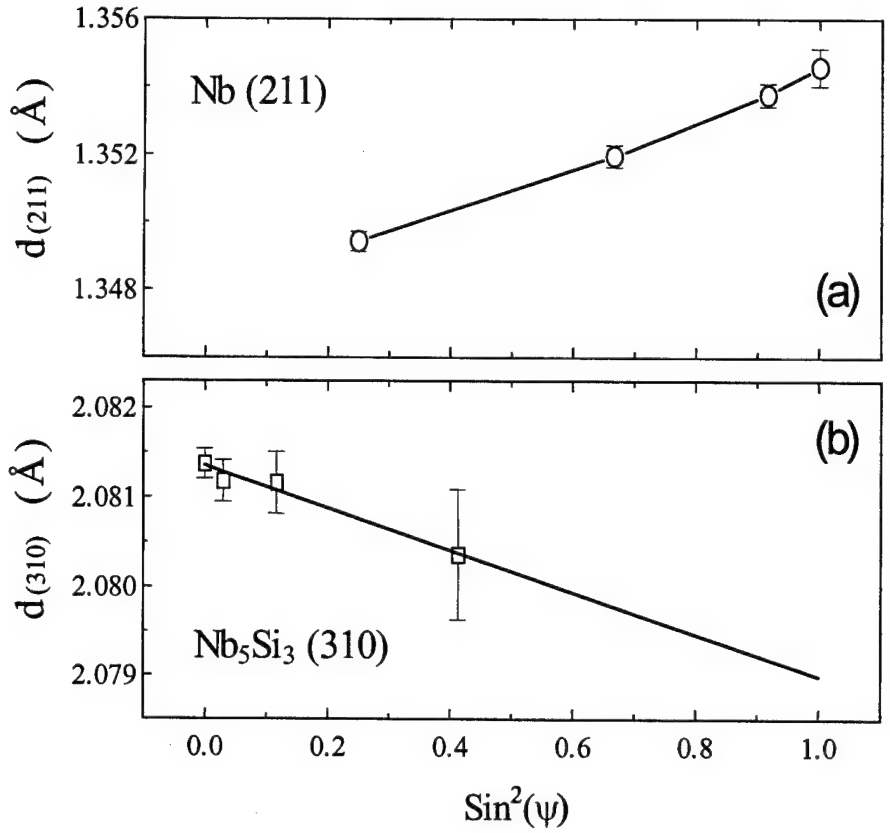

Figure 3.3: Planar spacing (d) versus $\sin^2 \psi$ for a nearly flat microlaminate, indicating that the Nb layers are in tension and the Nb_5Si_3 layers are in compression. The lines are (a) a visual guide, and (b) a linear fit, respectively.

Given the positive slope for the {211} planar spacings in Figure 3.3(a), the residual stresses in the Nb layers should be tensile and positive, as noted above. The magnitude of the stresses was first determined using six different pairs of {211} planes and Equation (3.11). Five pairs of planes yielded positive stresses that range from 202 MPa to 362 MPa, but one pair yielded a negative or compressive stress of -846 MPa. This extreme negative stress is attributed to the fact that the values of ψ for the two planes in this pair are very close in value. In such a case even limited scatter in the data can lead to significant errors in the calculated stresses. The pairs taken from planes with very different values of ψ are positive and tensile as expected.

Due to the scatter in the above measurements, the residual stresses in the Nb layers were also analyzed using two additional crystallographic planes, namely {310} and {321} planes. Plots of all three planar spacings are shown versus $\sin^2\psi$ in Figure 3.4(a) – (c), and the calculated stresses are plotted in Figure 3.5. Using all possible pairs of {211}, {310} and {321} planes, all but two of the calculated stresses were positive and the values ranged from 89 MPa to 516 MPa. Averages of the positive stresses for each family of planes are plotted in Figure 3.5 for comparison.

To help minimize the scatter in the calculation of residual stresses, we also plotted planar spacings versus $\kappa(\psi,\phi)$ as shown in Figures 3.4(d)-(f)), and we analyzed these values using Equation (3.13). Note that the planar spacings vary in a more linear fashion versus $\kappa(\psi,\phi)$ in Figures 3.4(d)-(f) than versus $\sin^2\psi$ in Figures 3.4(a)-(c). The slopes and intercepts of the linear fits in Figures 3.4(d)-(f) were used along with Equation (3.13) to compute average stresses for the Nb layers. The stresses obtained using the {211}, {310} and {321} planes are 299 ± 47 MPa, 220 ± 72 MPa, and 153 ± 11 MPa, respectively, and are shown in Figure 3.5.

3.4.2 Bending Stresses:

To characterize the magnitude of bending stresses that can be induced in free-standing microlaminate foils during mechanical testing, we performed an X-ray analysis on a second sample that developed curvature along one axis during the 1200 °C anneal. To induce bending stresses in this curved sample, it was pressed flat and mounted on a substrate for testing as shown

in Figures 3.2(b) and (c). Spacings for {310} Nb_5Si_3 planes and {321} Nb planes are plotted in Figure 3.6 versus $\sin^2\psi$. Note that the two data sets have negative slopes implying that both the top Nb layer and the top Nb_5Si_3 layer are in compression. This is quite different from the case for the first sample, which lacked an initial curvature (Figure 3.3).

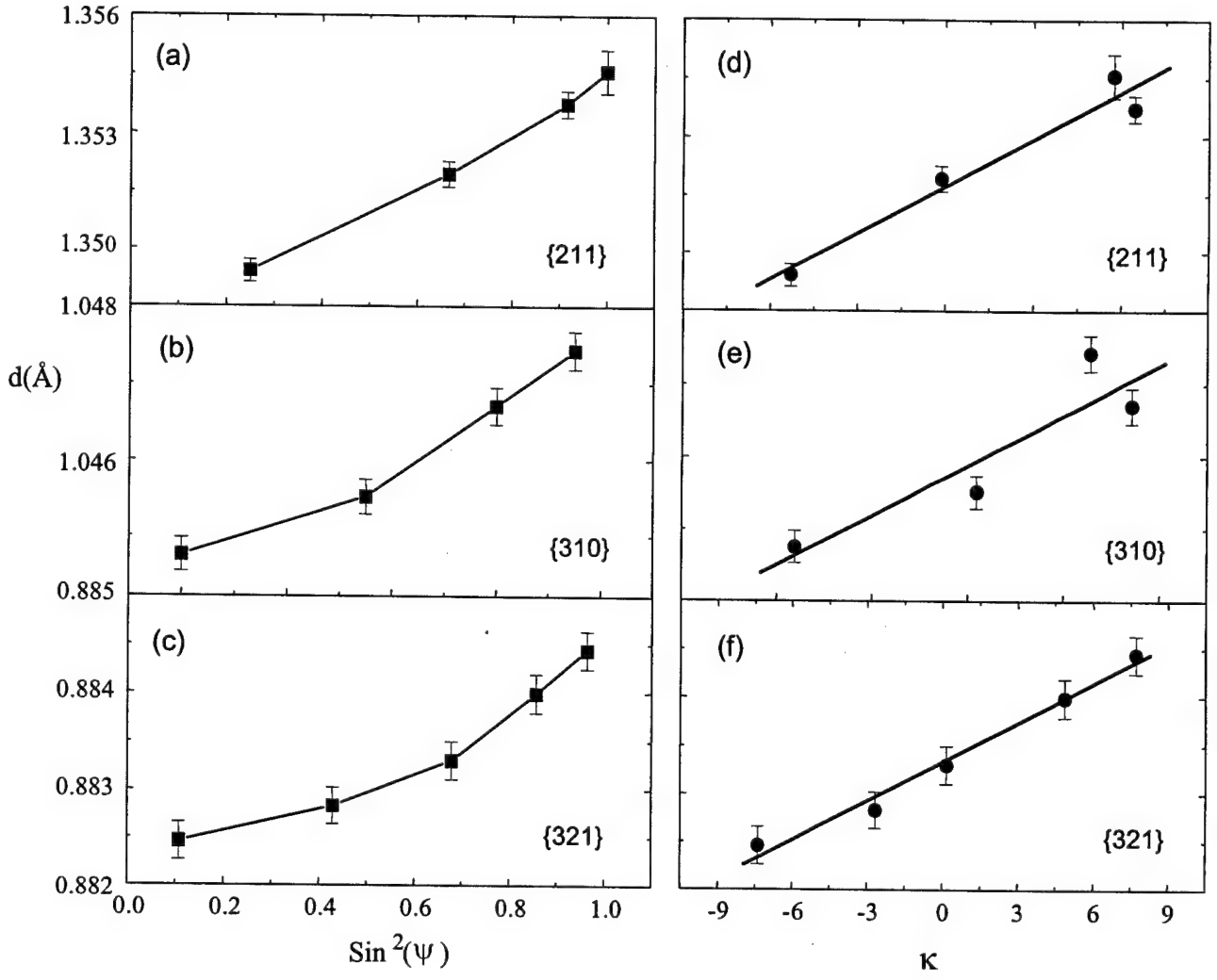

Figure 3.4: Stress analyses for anisotropic Nb. (a)-(c): planar spacing, d, versus $\sin^2\psi$, and (d)-(f): planar spacing, d, versus $\kappa(\psi,\phi)$.

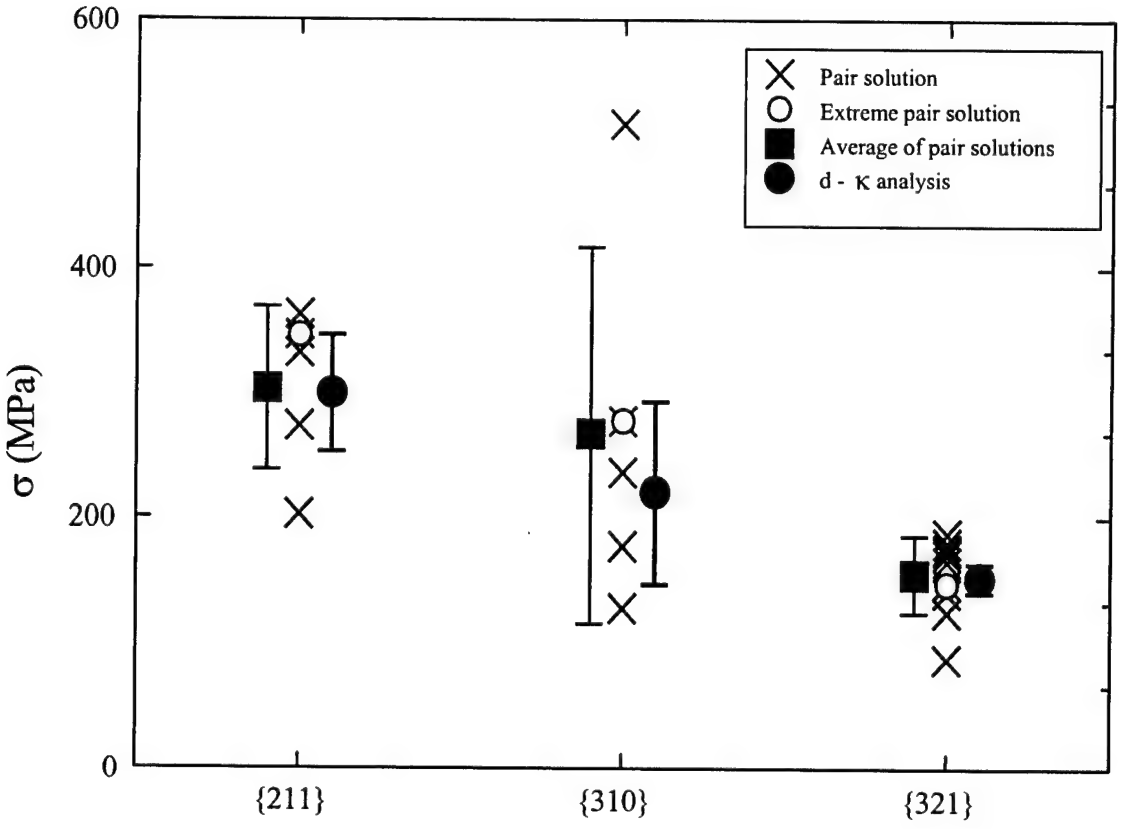

Figure 3.5: Stress values versus diffraction plane indexes for the anisotropic Nb layers. The crosses represent the pair solutions based on the method of Clemens and Bain [6]; open circles are the pair solutions obtained using the two extreme values of $\sin^2\psi$, and solid squares are the averages of all positive pair solutions. Stresses obtained using the d-$\kappa(\psi,\phi)$ method are shown as solid circles. The error bars represent the standard deviations.

To calculate the magnitude of the bending stress in the upper silicide layer, we note that Equation (3.9), in which $\varepsilon_{\phi\psi} = (d_{\phi\psi} - d_0)/d_0$, can be rewritten as $d_{\phi\psi}\big|_{\phi=0} = \alpha + \beta \sin^2\psi$. Using the linear fit in Figure 3.6, one can then solve for the bending stress, σ^b,

$$\sigma^b = \frac{E - \sigma[2\nu + (1+\nu)\alpha/\beta]}{(\alpha/\beta + \nu)(1+\nu)} \tag{3.14}$$

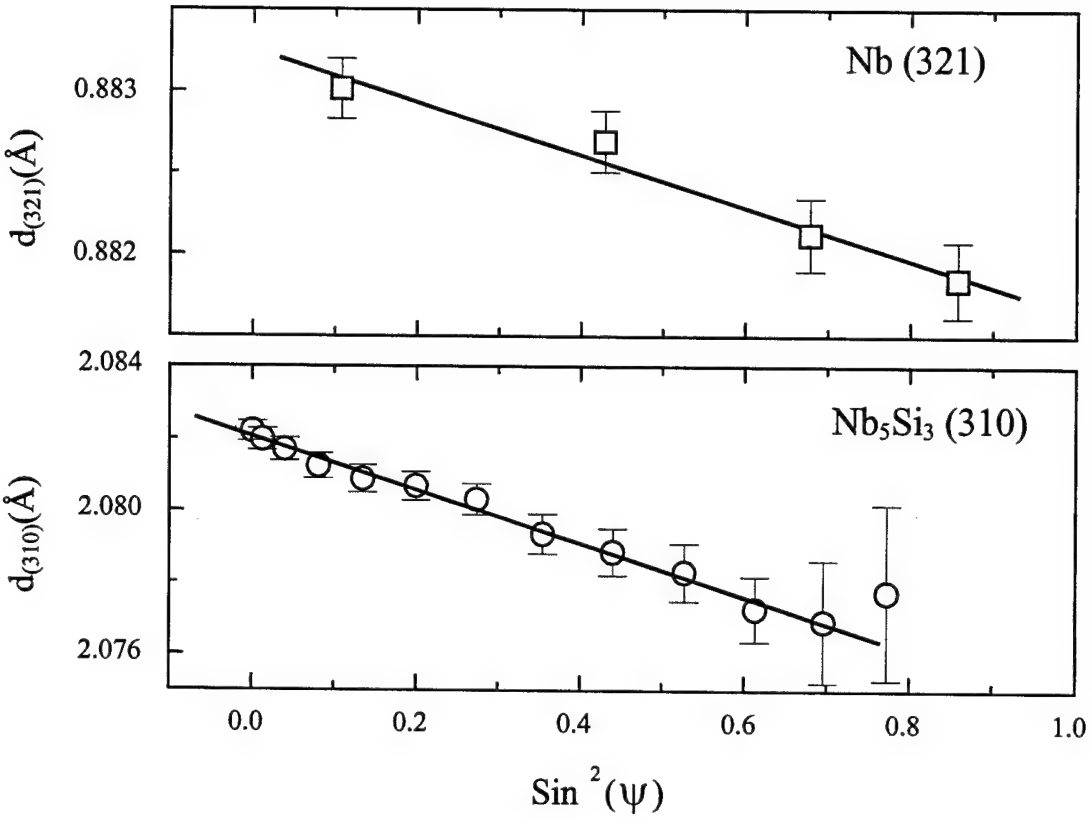

Figure 3.6: Planar spacing (*d*) versus $\sin^2\psi$ for a curved microlaminate that has been flattened, indicating both Nb and Nb_5Si_3 layers are in compression. The lines are linear fits.

Based on the data for the Nb_5Si_3 (310) planes in Figure 3.6, α=0.208206 nm and β= -7.4×10^{-4} nm. If we assume a residual stress of -300 MPa is present in the silicide layers, as measured for the flat sample, the bending stress in the silicide layer is -673 ± 50 MPa. To confirm this magnitude of bending stress, the second sample was removed from its mounting and the curvature along its bending axis was measured to be -76.9 m^{-1} [9]. Using this curvature, the bending stress that was induced in the top Nb_5Si_3 layer can be calculated using a simple beam bending equation,

$$\sigma^{b}_{\text{Curvature}} = \frac{E}{1-\nu^2} Kz = -628 \pm 10 \text{ (MPa)} \quad (3.15)$$

This second calculation of bending stress falls well within the standard deviation of the value determined by X-ray analysis, thereby supporting the X-ray measurements as well as the assumption of a -300 MPa residual stress in the silicide layer

3.5 Discussion

The X-ray diffraction data indicates that when Nb/Nb_5Si_3 microlaminates are cooled relatively quickly from 1200 °C, significant thermal stresses are induced in the alternating layers due to their mismatch in thermal contraction. As expected, the silicide layers are in compression and the Nb layers are in tension. However, the magnitudes of the stresses are not equal as one would expect for samples with equal layer thicknesses. The residual thermal stresses in the silicide layer are -309 MPa while the residual thermal stresses in the Nb layer range from 153MPa to 299MPa. Several factors could account for this difference in magnitude.

First, because there are 25 Nb layers and only 24 Nb_5Si_3 layers in the microlaminates, the stress in the Nb layers should be approximately 4% less than the stress in the silicide layers, assuming equal layer thicknesses. But, if we combine the average stresses obtained using the three different Nb planes, the overall average stress in the Nb layers is 224 MPa, which is 27.5% less than the 309 MPa for the silicide layer, not 4%. Another possible cause for the difference is unequal layer thicknesses for the Nb and Nb_5Si_3 layers. However, based on detailed cross-sectional microscopy, the layer thicknesses differ by less than 5 %. Therefore, while unequal

numbers and unequal thicknesses of layers can account for some of the difference in magnitude, together they still cannot account for the full difference.

A second and more likely source of the difference in magnitude is the presence of small bending stresses. As seen for the second sample, a noticeable and easily measured curvature produces a large bending stress. Thus, a very small curvature, that is not easily detected, could produce compressive stresses in the upper laminates; these would act to reduce the tensile stress in the Nb layer and increase the compressive stress in the silicide layer. In fact, a hardly visible curvature with a radius of 200 mm can raise the compressive stress in the silicide layer by 42 MPa and lower the tensile stress in the Nb layer by 24 MPa, when a sample of 6×6 mm^2 in size is flattened for testing. These bending stresses, along with the unequal numbers and thicknesses of layers, could account for the full difference in the magnitude of the thermal stresses.

A third discrepancy that warrants examination is the large variation in the residual stresses that were measured for the Nb layers using the three different families of planes. To examine this difference, we first review the elastic analyses that were used to calculate stresses in the silicide and Nb layers. The method used to quantify stresses in the silicide layer is a standard d-$\sin^2\psi$ technique for isotropic materials. The use of an isotropic analysis was justified by the fact that the silicide layers have a small grain size and limited crystallographic texture. This assumption appears to be reasonable given the plots of d versus $\sin^2\psi$ in Figures 3.3 and 3.6 are linear. Earlier reports have shown that crystallographic texture and the resultant elastic anisotropies yield nonlinear d-$\sin^2\psi$ curves [10]. The applicability of an isotropic analysis is

also supported by the consistency of the results for the two samples. When a compressive residual stress of –300 MPa was assumed in Equation (3.13) for the silicide layers, the bending stress in the upper silicide layer was calculated to be -673 MPa in the curved sample. This number is similar to the bending stress (-628 MPa) that was predicted using the initial curvature of the sample and isotropic beam bending equations. Thus, the isotropic analysis of residual stresses in the silicide layers appears to be self-consistent.

In contrast to the silicide layers, the Nb layers are strongly textured and elastically anisotropic. Therefore, we utilized the analysis proposed by Clemens and Bain [6] for <110> fiber textured films that is designed to account for this elastic anisotropy. Applying Equation (3.11) to pairs of planar spacings in Figures 3.4(a)-(c), we obtained positive stress values in most cases, but the variation of measured stresses in Figure 3.5 is large for the Nb layers. Some of this variation can be attributed to experimental scatter. The stresses that were measured using planes with very similar values of ψ are more susceptible to experimental errors and yielded large variations from the average values. This can be minimized by calculating stresses using families of planes that have very different values of ψ. For example, if one uses the data points with the lowest and highest values of $\sin^2\psi$ in Figures 3.4(a) - (c), the calculated residual stresses are close to the average values, as shown by the open circles in Figure 3.5. Thus, scatter can be reduced by carefully selecting pairs of planes with very different ψ values. However, one would still prefer to average over many planes and $\sin^2\psi$ values without sacrificing precision.

Plotting planar spacings versus the constant $\kappa(\psi,\phi)$ instead of $\sin^2\psi$ provides an alternative method for averaging over a full range of $\sin^2\psi$ values. For all three sets of crystallographic planes shown in Figures 3.4(d) - (e), the linear fits to the d versus $\kappa(\psi,\phi)$ plots include the data for four or five specific planes, with particular values of ψ and ϕ. Note that the average stresses determined from the slopes and intercepts of these linear fits are close to the averages calculated using the pairs of planes. However, they have lower standard deviations, as indicated by the shorter error bars in Figure 3.5, even though the same families of planes have been used. In fact, the difference in standard deviations would have been even larger if the negative values of stresses had also been included in the average of the pairs of planes.

Regardless of which technique was used to calculate residual stresses in the Nb layers, though, the {211}, {310} and {321} planes all yield different residual stresses. One possible source for this discrepancy is the fact that the Nb grains are likely to experience a nonequal biaxial stress state instead of the equal biaxial stress state that was assumed in the Clemens and Bain's analysis [6]. To assess the effect of this nonuniformity of in-plane stress, we consider the constraints that the alternating layers impose on each other. We begin by assuming the silicide layer is isotropic. We also assume the Nb layers are isotropic in-plane because their in-plane texture is limited. Given this in-plane isotropy, each layer will force the other into a state of equal biaxial strain to accommodate the mismatch in thermal contraction on cooling. However, the biaxial strain state for each Nb grain may be different. If the individual Nb grains are much wider than they are thick, i.e. in a "pancake grain" geometry, then each Nb grain will behave like the Nb layers and will deform equally in all directions. .In this case, each grain experiences a state

of equal biaxial strain, not equal biaxial stress as was assumed [6]. Under equal biaxial strain conditions, stresses will vary with in-plane direction because the (110) plane is not elastically isotropic in Nb. Young's modulus varies from a high of 154.2 GPa for the [001] direction to a low of 80.7 GPa for the $[1\,\bar{1}\,1]$ direction. In-plane stresses will follow a similar trend showing higher stresses in stiffer directions.

The opposite extreme to the above geometry is the case of columnar grains that are much thicker than they are wide. In this case the surrounding silicide layers place only limited constraints on each Nb grain and equal biaxial stress conditions are likely to prevail. The Nb grains tested here are approximately equiaxed, as shown in Figure 2.4(b). For this geometry, the surrounding silicide layers place only moderate constraints on each Nb grain and the in-plane conditions on each grain are likely to fall somewhere between the equal biaxial strain and equal biaxial stress conditions describe above. Therefore, the most likely in-plane stress state is one of nonequal biaxial stresses.

To determine whether a nonequal biaxial stress state could produce variations in the residual stresses measured for each of the three families of planes, we consider the case of individual X-ray diffraction scans. During the measurement of a given planar spacing, the X-ray scan samples a unique set of Nb grains with a specific in-plane orientation, ϕ. If the in-plane stiffness of these grains is high in the direction in which the in-plane strain is measured (such as the y-axis in Figure 3.2), then the residual stresses that are measured are likely to be high as well. In Figure 3.7, the average measured stresses are plotted versus the average in-plane values of E

for the three different families of planes. While there is not a substantial variation in the average in-plane value of E for the grains that were sampled for the {211}, {310} and {321} planes, the average stresses do scale with the average in-plane stiffnesses. This supports the hypothesis that a nonequal biaxial stress state in the Nb grains may account for at least some of the variation in the residual stresses that are shown in Figure 3.5.

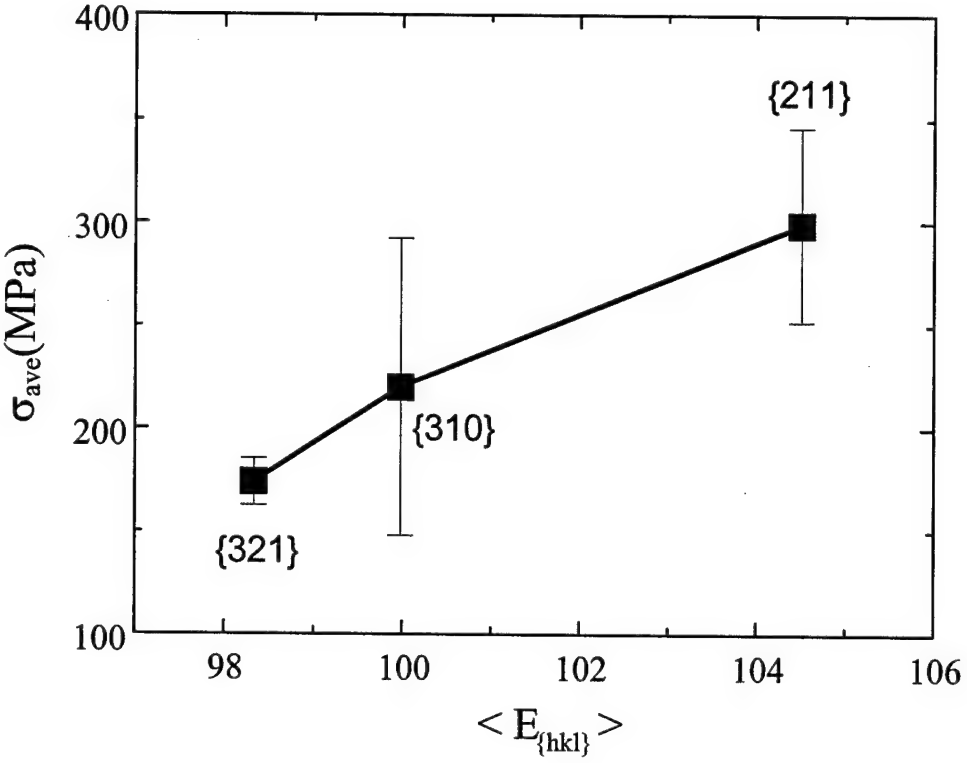

Figure 3.7: Average stress versus average in-plane Young's modulus for <110> fiber-textured Nb laminate.

As for the bending stresses in these free-standing microlaminates, our experimental observations suggest that even moderate curvatures can produce significant stresses when the samples are flattened for testing. Here, a curvature of -76.9 m^{-1} produced a bending stress of -628 MPa. Similarly, a much smaller curvature with a radius of one meter would produce a bending stress of 8.2 MPa. Thicker samples would experience even higher stresses for similar curvatures. Thus, care must be taken when fabricating and testing microlaminate foils to ensure bending stresses are minimized.

The presence of residual stresses as high as 300 MPa, and the possible addition of bending stresses with similar magnitudes, is very significant in that microlaminates such as these yield or fracture when stresses as low as 500 MPa are applied to them at room temperature. Thus, residual stresses and bending stresses can dramatically enhance or retard deformation in each laminate, depending on the stress state. For example, in simple tension tests, the residual tensile stresses in the Nb layers will lower the applied stress at which dislocations will begin to move in these layers. In contrast, the residual compression in the Nb_5Si_3 layers will raise the applied stress needed to drive fracture in these layers. Thus, depending on which layer controls the onset of inelastic deformation, the residual thermal stresses can either enhance or retard that onset.

Based on room temperature tension tests of these Nb/Nb_5Si_3 microlaminates, cracking of the silicide phase appears to limit their strength as discussed in the next chapter. Thus, the residual compressive stresses in the silicide layers should raise the overall strength of the foils. Furthermore, the thinner the silicide layers are relative to the Nb layers, the larger the residual

compressive stresses and the greater the enhancement in strength. Similar trends should appear in many metal/ceramic or metal/metal microlaminates that contain significant residual stresses. In addition, residual thermal stresses should also impact the mechanical performance of *in situ* metal/silicide composites that have elongated phases and similar mismatches in thermal contraction.

3.6 Conclusions

Residual stresses in both flat and curved Nb/Nb_5Si_3 microlaminates were analyzed and measured using asymmetrical X-ray diffraction. For the Nb_5Si_3 layers, a standard d-sin$^2\psi$ analysis for isotropic materials was used and a residual compressive stress of -309 MPa was measured. This technique was also modified to account for uniaxial bending stresses. The stresses in the Nb layers were quantified using an anisotropic elastic analysis, three different families of planes, and a new graphical analysis of the resulting planar spacings. The three families of planes produced a range of residual tensile stresses with an average of 224 MPa. The residual stresses in the Nb_5Si_3 and Nb layers are attributed to a mismatch in the thermal contraction of Nb and Nb_5Si_3 on cooling from 1200 °C.

In quantifying residual stresses in the {110} textured, elastically anisotropic Nb layers, a new graphical method was introduced. For a given family of planes, four to five measured planar spacings were plotted versus $\kappa(\psi,\phi)$ and the intercept and slope of the resulting line were used to determine the residual stress. By considering many different planes in a

given family all at once, this method yielded average values with lower standard deviations than those obtained by averaging data from several pairs of planes.

Besides the residual stresses, very large bending stress were also detected in a second sample that developed curvature during annealing and then was flattened for X-ray analysis. For this sample, with an initial curvature of 79 m^{-1}, bending stresses were measured to be as large as -673 MPa in the top Nb_5Si_3 layer. Given the magnitude of these stresses, care must be taken to account for both residual stresses and bending stresses when quantifying mechanical properties of microlaminates at room temperature.

3.7 References for Section 3

1. D. Van Heerden and T.P. Weihs, (unpublished).

2. A. Goldsmith, T.E. Waterman, and H.J. Hirschhorn, in *Thermophysical Properties of Solid Materials*, WADC Technique Report 58-476, Vol.**1**, (August 1960).

3. G.V. Samsonov, L.A. Dvorina, and B.M. Bud', Silitsydy (Silicides) Moscow, *Metallurgiya*, (1979) 272.

4. J.D. Rigney and J.J. Lewandowski, *Metall. Mater. Trans.* **27A**, 3292 (1996)

5. M.G. Mendiratta and D.M. Dimiduk, *Scripta Metall. Mater.* **25**, 237 (1991)

6. B.M Clemens and J.A. Bain, Materials Research Society Bulletin, (July, 1992) p.46.

7. *Landolt-Boenstein Numerical Data and Functional Relationships in Science and Technology*, Edited by O. Madelung and D.F. Nelson, New Series III, Volume **29**, p.14, p.302, (1990) Springer-Verlag.

8. I.C. Noyan and I.B. Cohen, *Residual Stresses*, Springer, New York (1987)

9. We used optical microscopy to obtain a low magnification image of the sample's cross-section, and then fit the image to a circle to obtain the sample's curvature. The relative error is approximately 5% for the curvature.

10. P.V. Houtte and L.D. Buyser, *Acta. Metall. Mater.* **41**, (1993) 323.

4. Room Temperature Mechanical Properties

4.1. Preparation of samples for Mechanical Testing of Free-standing Foils

Microlaminate foils for room temperature tensile testing were sputter deposited from Nb and Nb_5Si_3 targets at a pressure of 5.0mTorr. Large 5" x 12" sputter guns were used to increase the uniformity and number of samples produced. Detailed information on these foils is listed in Table 4.1. After deposition the foils were removed from their substrates and annealed at 1200°C for 3hours to obtain the desired Nb/Nb_5Si_3 laminate structure. Once the Nb/Nb_5Si_3 microlaminates were fabricated, they were shaped into tensile specimens by electron discharge machining or CNC milling. The tensile specimens have a dog bone shape with a uniform gauge section that is 10mm long and 9mm wide. Prior to mechanical testing the edges of the specimens were polished to a 0.1μm finish and Al tabs were glued to the ends of the specimens to facilitate gripping in the test machine. The tensile tests were performed on a screw-driven, Instron test machine with a cross-head displacement rate of 0.01 mm/sec (a strain rate of 0.001 /sec). For some specimens, an LVDT was attached to the grips to measure displacement. The fracture surfaces of several of the specimens were examined using an SEM.

Table 4.1. Sputter deposited microlaminate samples

Material #	Bilayer (μm)	Nb Thickness (μm)	Nb_5Si_3 Thickness (μm)	V_{Nb}	Atomic Fraction Nb
W98-025	20.0	10.0	10.0	0.50	0.81
W98-023	15.0	10.0	5.0	0.67	0.87
97-035D	14.2	12.1	2.1	0.86	0.95
W98-022	11.0	10.0	1.0	0.91	0.97
97-035A	10.0	5.0	5.0	0.50	0.81
W98-027	10.0	5.0	5.0	0.50	0.81
97-041D	2.8	2.4	0.4	0.86	0.95
97-041A	2.0	1.0	1.0	0.50	0.81
L98-04	2.0	1.0	1.0	0.50	0.81
98-002D	0.57	0.49	0.08	0.86	0.95

4.2. Experimental Results

Stress/strain curves for three different microlaminate foils are shown in Figure 4. 1. The results for these samples show the range of plastic behavior that was observed. Many of the samples failed abruptly with no signs of plasticity while approximately 40% of the samples exhibited some non-linearity in the stress/strain curves prior to failure. The non-linearities are associated with cracking of the silicide layer and ductile bridging of these cracks by the Nb layers. Cracks in the silicide layers could be seen on the edge of these specimens as shown in Figure 4. 2. We also observed fine lines on the surface of many of the specimens due to the localize plasticity associated with the bridging in the Nb layers. Edge cracks and surface lines were not present in the specimens that exhibited linear stress/strain curves to failure.

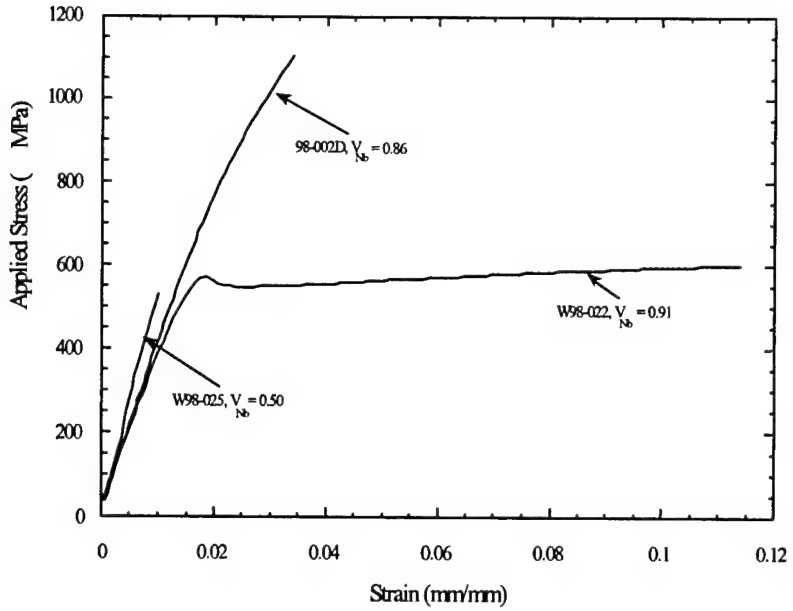

Figure 4. 1: Typical stress/strain curves for microlaminate foils of Nb/Nb_5Si_3 having V_{Nb} of 0.91, 0.86, and 0.50.

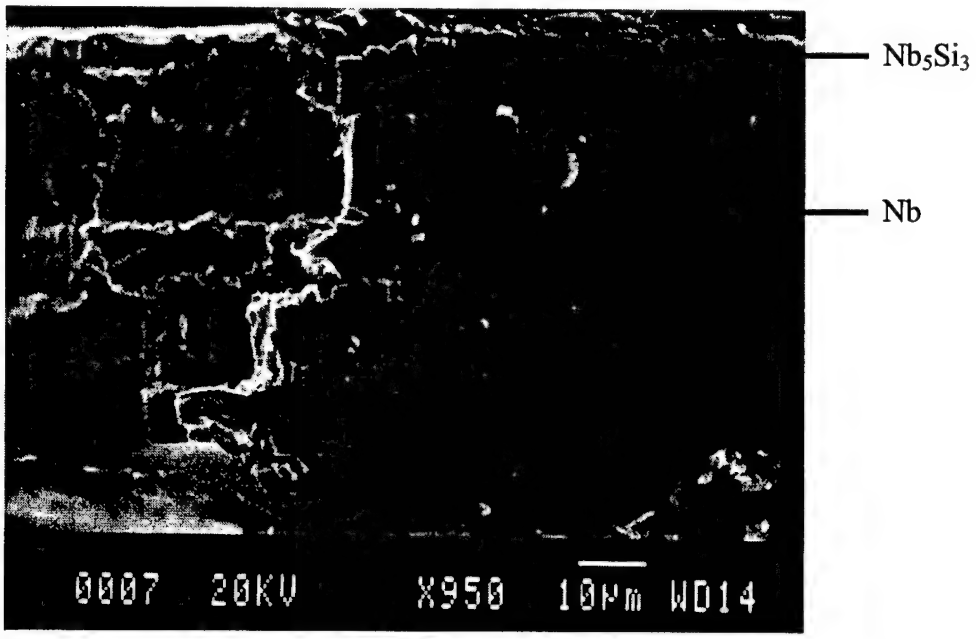

Figure 4. 2: SEM micrograph of the edge of the 14μm thick bilayer Nb/Nb_5Si_3 microlaminate tensile specimen following failure in tension. Note the multiple edge cracks in the thinner silicide layers.

Table 4.2: Room Temperature Tensile Test Results for Nb/Nb_5Si_3 Microlaminate Foils

Material #	Bilayer (μm)	V_{Nb}	σ_{el} (MPa)	σ_{uts} (MPa)
W98-025	20	0.50	396	396
			530	530
			486	486
		Average	**471±68**	**471±68**
W98-023	15	0.67	548	548
			481	481
			443	443
			554	554
			574	574
		Average	**520±55**	**520±55**
97-035D	14.2	0.86	418	677
			652	698
		Average	**535**	**688**
W98-022	11	0.91	436	600
			415	582
		Average	**426**	**591**
97-035A	10	0.50	643	643
W98-027	10	0.50	477	477
		Average 10 μm	**560**	**560**
97-041D	2.8	0.86	**972**	**972**
97-041A	2.0	0.50	563	563
			732	732
L98-04	2.0	0.50	559	559
		Average 27.0 μm	**618±99**	**618±99**
98-002D	0.57	0.86	**582**	**1101**

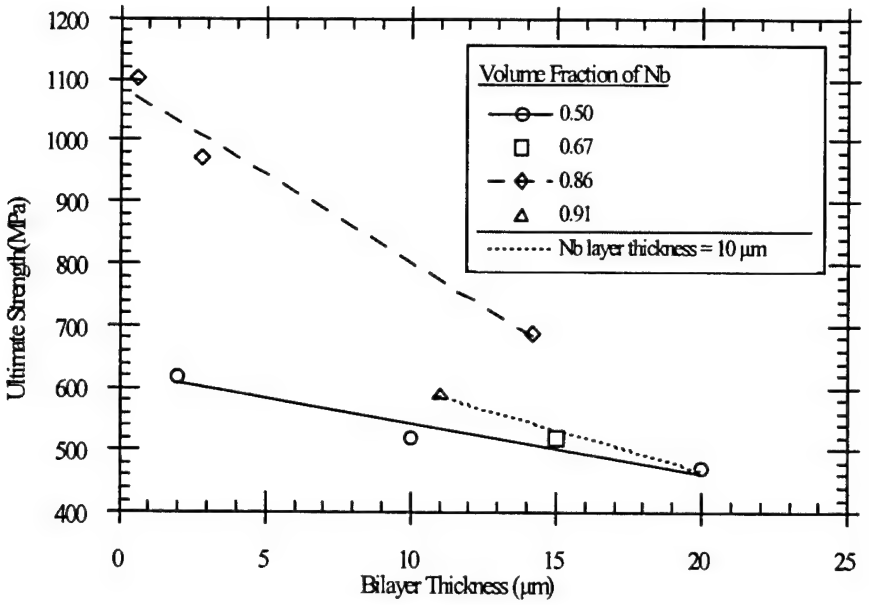

Figure 4. 3: The ultimate tensile strength measured for Nb/Nb_5Si_3 foils as a function of bilayer thickness, volume fraction of Nb, and Nb layer thickness.

The room temperature strengths of the laminates ranged from 396 MPa to 1101 MPa and varied with bilayer thickness and the volume fraction of Nb. Values for elastic limits and ultimate tensile strengths are listed in Table 4.2 and the UTS's are plotted in Figure 4. 3. Note the strong dependence of the UTS on both volume fraction and bilayer thickness.

Almost all of the specimens failed within their gage sections, with fracture surfaces running normal to the loading direction. Based on SEM observations of fracture surfaces (for specimens with bilayer thicknesses of 2μm, 2.8μm, 10μm, and 14.2μm), the Nb_5Si_3 layers always fractured in a brittle manner (Figure 4. 4). The fracture characteristics of the Nb layers, though, depended on layer thickness. For the 2 μm thick bilayer foils (Figure 4. 4(a)), the 1 μm Nb layers deformed and failed with chisel point features running parallel to the layers. In contrast, the foils with thicker Nb layers (Figure 4. 4(b)) displayed a quasi-cleavage like failure with the fracture characteristics

occurring primarily normal to the layering. For all of the microlaminates, cracks observed in the Nb_5Si_3 did not propagate into the Nb and typically did not approach the interface of the Nb and Nb_5Si_3 layers. No interfacial delamination was observed in any of the specimens.

a) 2μm

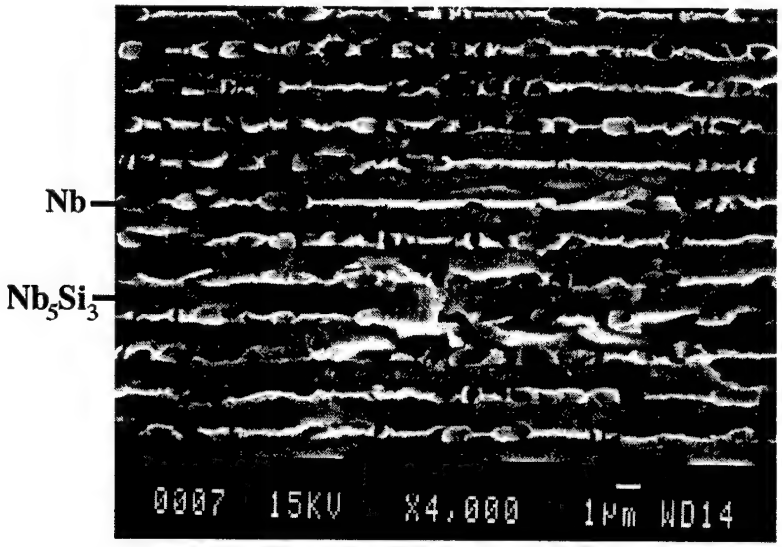

b) 10μm

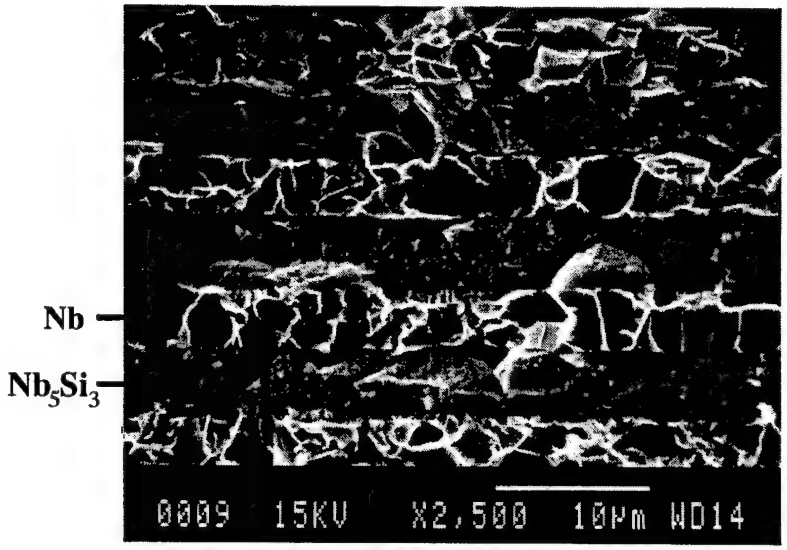

Figure 4. 4: SEM micrographs of fracture surfaces of Nb/Nb_5Si_3 foils with bilayer thicknesses of a) 2μm and b) 10μm.

4.3. Discussion

4.3.1 Fracture of the Microlaminates

When the microlaminates failed in tension, the fracture surface of the Nb layers was dependent on layer thicknesses, as shown in Figure 4. 4. The thicker Nb layers exhibited a quasi-cleavage type of tensile failure, whereas the thinner Nb layers deformed to a chisel point. Rigney and Lewandowski observed a similar result in Nb/Nb_5Si_3 *in situ* composites, where the large "primary" Nb particles failed by cleavage and the smaller "secondary" Nb particles in the silicide matrix always failed in a ductile manner [1]. The change in fracture mode can be attributed to changes in the constraint of the Nb layers during crack propagation [2-5].

Just prior to catastrophic failure of the microlaminate, the Nb_5Si_3 layers crack and are bridged by Nb ligaments, as shown in Figure 4. 2. The constraint on the Nb ligament remains high because there are no delaminations along the Nb/Nb_5Si_3 interfaces. For the same crack opening in the silicide layers, thicker Nb ligaments will tend toward a state of plane strain and a more brittle fracture mode, whereas thinner Nb ligaments will tend toward a state of plane stress and a more ductile fracture mode. The resulting fracture surfaces are consistent with the experimental observations.

In addition to the edge cracks observed in the silicide layers in Figure 4. 2, a small number of intralamellar cracks were found running parallel to the layering within the Nb_5Si_3 layers, as shown in Figure 4. 4(a). However, most of the intralamellar cracks did not propagate toward the Nb layers. Typically, the intralamellar cracks could be caused by the out-of-plane Poisson contraction of the Nb layers during loading [6]. The few

cracks that did propagate toward the Nb were blunted and arrested. Thus the Nb layers not only bridged the cracks in the Nb_5Si_3 layers, they also prevented cracks from propagating to adjacent layers.

Most of the foils exhibited some deviation from linearity in the stress/strain curves prior to failure. In these foils, lines were seen on the flat surfaces of the specimens and multiple edge cracks were observed in the Nb_5Si_3 layers, by optical microscopy and SEM (Figure 4. 2). In all cases stable edge cracks were bridged by Nb ligaments. Similar edge cracks were seen by Provancher and Ghosh in Nb/Nb_5Si_3 laminates with much thicker layers [7]. In Nb/Al_2O_3 microlaminates, multiple cracking of the brittle phase is known to generate nonlinearities in the force-displacement curves [8]. Thus, the nonlinearity in the stress/strain curves for these samples were assumed to mark the onset of fracture in the Nb_5Si_3 layers. The presence of these edge cracks implies that stable crack growth occurs prior to catastrophic failure.

4.3.2. Strength or Elastic Limit

The strength of microlaminate foils should depend on the volume fraction of the phases (we use volume fraction of Nb - V_{Nb}), the bilayer thickness (δ), and cracks or flaws in any brittle phases such as the Nb_5Si_3 tested here. In general, strength should increase as: 1) the volume fraction of the stronger or tougher material is increased, 2) the thickness of ductile layers decrease due to a higher constraint of dislocation motion ($\sigma_y \propto 1/(\lambda)^{1/2}$), and 3) the size of flaws in the brittle (silicide) layers is reduced ($\sigma_f \propto 1/(a)^{1/2}$). However, determining which of these parameters controls the strength of a particular set of microlaminate foils is difficult because the parameters are interrelated. If one wants to reduce the thickness of just one layer, volume fraction also changes, and the size of flaws present in that layer may decrease as well.

The strength of the microlaminate should also be influenced by residual stresses. For these samples, the Nb layers are under residual tension and the silicide layers are under residual compression as noted in Chapter 3. For samples with equal layer thicknesses (V_{Nb} = 0.50), the residual thermal stresses can range from 200MPa to 300MPa, and for samples with higher volume fractions of Nb, the residual compressive stresses in the thinner silicide layers can be several times larger. Since the magnitude of these residual stresses are similar to some of the elastic limits listed in Table 4.2, they are very likely to influence the onset of deformation in the microlaminates. The residual tensile stresses in the Nb layers will lower the average applied stress that is necessary to start plastic deformation in the Nb layers. In contrast, the residual compressive stresses in the silicide layers will raise the average applied stress that is necessary to initiate fracture in the silicide layers.

To analyze the onset of plastic deformation in the microlaminates we utilize the fact that the samples were loaded in uniaxial tension under isostrain conditions. Thus, the first phase to reach a yield or fracture strain should determine the elastic limit of the microlaminate. The strain that is applied to the Nb and Nb_5Si_3 layers can be estimated as

$$\varepsilon_{laminate} = \frac{\sigma_{el}}{E_{laminate}} \tag{4.1}$$

where

$$E_{laminate} = V_{Nb}E_{Nb} + (1 - V_{Nb})E_{Nb_5Si_3} \tag{4.2}$$

The applied stress in either layer is then simply the product of the average strain and the Young's Modulus for that layer. For the silicide layers, the applied stress at the elastic limit is given by:

$$\sigma_{Nb_5Si_3} = \varepsilon_{laminate} E_{Nb_5Si_3} \quad (4.3)$$

where $\varepsilon_{laminate}$ is the strain in the laminate at the elastic limit. A similar equation can be given for the Nb layers. For the silicide phase we assumed a Young's Modulus of 365GPa while for the Nb layer a modulus of 120 GPa was calculated by integrating E over all directions on the (110) plane.

Since the total strain in each layer will determine the onset of plasticity, not just the applied strain, the residual thermal strains must be considered when predicting which layer yields or fractures first. The residual thermal strains were estimated using Equation 3.2, the coefficients of thermal expansion, and the biaxial moduli described in Chapter 3. The total stress in each layer was then calculated by summing the applied stresses and the residual stresses and the results are included in Figure 4. 5(a) and (b) for all specimens. Note that the magnitude of the total stresses are quite similar in both layers. It is relatively constant for most layer thicknesses and may rise sharply at small layer thicknesses.

Comparing the total stresses in the Nb layers to the yield strength of bulk Nb [9, 10], one might expect that the Nb layers begin to yield before the silicide layers fracture. In this case plasticity in the Nb layer would determine the elastic limit. However, the Nb layers are highly constrained by the surrounding silicide layers and are likely to have much higher yield strengths than bulk Nb. To check this hypothesis we performed a series of nanoindentation experiments. Arrays of nanoindentations were made on polished cross-sectional samples with thick individual layers. An example of an array with very large nanoindentations is shown in Figure 4. 6. Most arrays had much smaller indentations so

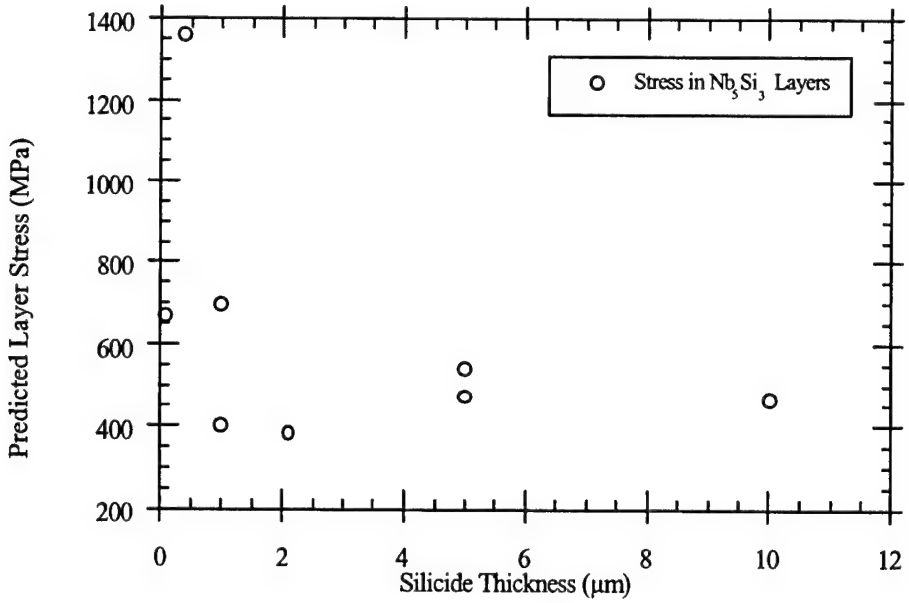

Figure 4. 5: (a) Stress in Nb_5Si_3 layers predicted from the strain at the average elastic limit as a function of silicide layer thickness. The stress is a combination of the applied stress and a thermal residual stress due to a 900°C temperature differential.

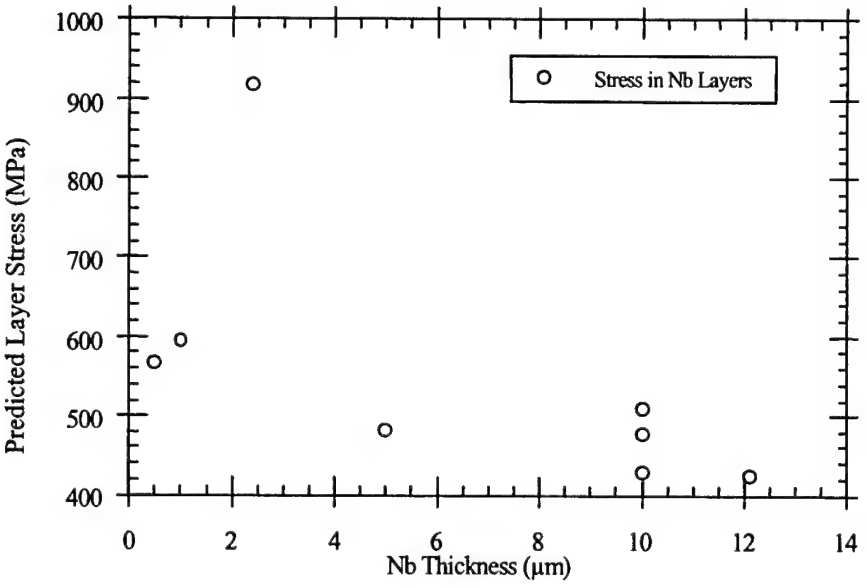

Figure 4. 5: (b) Stress in Nb layers predicted from the strain at the average elastic limit as a function of Nb layer thickness. The stress is a combination of the applied stress and a thermal residual stress due to a 900°C temperature differential.

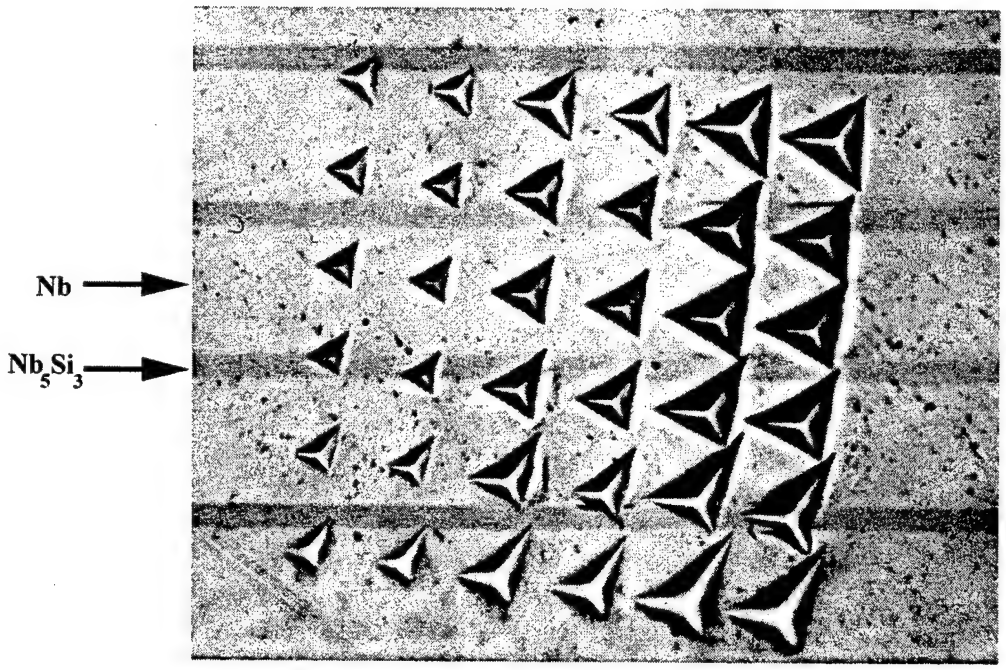

Figure 4. 6: Nanoindentation of Nb/Nb_5Si_3 Microlaminate (δ=14.2 μm). The indents were performed at depths of 500, 750, and 1000 nm.

that the properties of single layers could be measured. Using a Berkovich indenter, the methodology of Pharr and Oliver [11], and small indentations in thick layers, the hardness (H) of Nb was measured to be 5.38±0.52 GPa

A hardness of 5.38 GPa compares well with the results of Ji et al. who obtained a value of 6 GPa for Nb thin films [12]. However, it is much larger than the 1.6 GPa Vickers microhardness reported for the large "primary" Nb particles (12.7 μm) in cast and extruded Nb/Nb_5Si_3 alloys [1]. The higher hardness of the Nb in the Nb/Nb_5Si_3 microlaminates can be attributed to the smaller grain size and small Nb layer thicknesses,

both of which act to restrain dislocation motion in the Nb layers. Using this value of hardness and the Tabor relation ($H=3.2\sigma_y$), the yield strength of Nb was estimated to be 1.68 GPa which is much higher than any of the applied or total stresses in Figure 4. 3 and Figure 4. 5. Thus, yielding of the Nb layers does not appear to control the elastic limit of these microlaminates. A more likely source is fracture of the silicide layers.

To estimate when the silicide layers will fracture, we followed the work of He et al. on crack growth in layered materials [13]. Here, though, we adopt a very simple, linear elastic fracture mechanic model, and assume that tunneling edge cracks in the silicide layers are loaded in a mode I geometry, similar to the edge cracks seen in Figure 4. 2. When the stress intensity at the tip of a tunneling edge crack exceeds K_{IC} for the silicide, the silicide layers will begin to crack and the elastic limit will be reached.

$$\left(\sigma_{applied} + \sigma_{thermal}\right)_{Nb_5Si_3} \sqrt{\pi a_{crit}} \geq K_{IC,Nb_5Si_3} \tag{4.4}$$

Since the edges of all samples were polished, the largest flaws are most likely to be cracks along grain boundaries in the silicide layer. We assume that the largest flaws scale with the largest Nb_5Si_3 grains and a_{crit} is estimated to be 1.5μm. However, for the thinnest silicide layers, these flaws will be smaller because the maximum grain size will be limited to the thickness of the silicide layer, t_{Nb5Si3}. Thus, $a_{crit} = t_{Nb5Si3}$. Using these conditions, a value of 1 MPa($m^{1/2}$) for K_{IC} [1], and a thermal stress based on a ΔT of 900°C and $V_{Nb} = 0.50$, we estimated the elastic limit for the microlaminates as a function of silicide layer thickness. The calculated values are plotted in Figure 4. 7 along with the average experimental results.

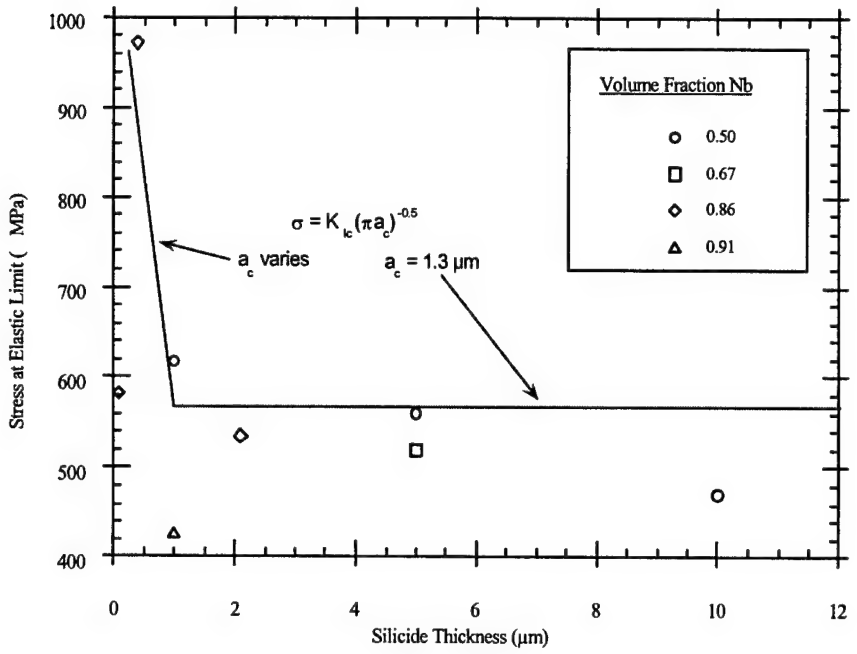

Figure 4. 7: The average stress applied to the Nb/Nb_5Si_3 foils at the elastic limit as a function of silicide layer thickness.

As shown in Figure 4. 7, the average elastic limit is predicted to be constant (~560 MPa for V_{Nb} = 0.50) for most silicide layer thicknesses. When the silicide layer thickness drops below 1.5μm, though, the maximum flaw size is limited and the average elastic limit increases. Most of the experimental data follows this predicted trend [13] and supports this general analysis. However, there is significant scatter in the data, and more data points are needed to verify the predicted trends, particularly at the smallest layer thicknesses. In addition, more experiments are needed to understand by the predicted trend in the elastic limit does not vary with volume fractions as expected. Samples with higher volume fractions of Nb should have larger residual compressive stresses in their silicide layers than samples with lower volume fractions. The larger residual compressive stresses should lead to higher elastic limits for a given silicide layer

thickness, assuming the silicide layer is controlling the onset of inelastic deformation. Clearly, this variation is not seen in Figure 4. 7.

4.3.3 Ultimate Tensile Strength:

Based on the data in Figure 4. 3 the ultimate tensile strength of the Nb/Nb_5Si_3 microlaminates clearly increases as bilayer thickness decreases. This variation is very common in microlaminates and nanolaminates and can be attributed to two factors. The first, and most common factor is that reducing layer thickness limits dislocation motion in metallic layers and therefore increases the stresses needed to drive plastic flow. A second factor is that the average flaw size in the silicide layers (not the largest flaw size, which controls the elastic limit) is likely to decrease as silicide layer thickness decreases.

Besides bilayer thickness, Figure 4. 3 also shows that increasing V_{Nb} from 0.50 to 0.86 increases the ultimate strength of the foils. This increase is also attributed to two factors. The first is an enhancement in the ductile phase toughening due to the Nb ligament. The greater the volume fraction of Nb ligaments, the greater the toughening of the microlaminate and the higher the UTS. The second is an increase in the residual compressive stresses within the silicide layer as V_{Nb} rises from 0.50 to 0.86. While residual stresses were not measured in microlaminates with a Nb volume fraction of 0.86, force equilibrium requires that the ratio of stresses in the Nb and Nb_5Si_3 layers scales with the ratio of layer thicknesses: t_{Nb}/t_{Nb5Si3}. Thus, as V_{Nb} jumps from 0.50 to 0.86, the residual stresses in the silicide layers could increase dramatically. This would limit crack growth in the silicide layers and thereby increase the UTS for the microlaminate.

Figure 4. 8 shows that besides bilayer thickness and volume fraction of Nb, the UTS for the microlaminates also correlates well with the silicide layer thickness. Note in

Figure 4. 8 that the UTS increases steadily as silicide layer thickness decreases. This trend supports the earlier argument that the average flaw size in the silicide layer will decrease as layer thickness decreases, thereby enabling higher UTS's to be obtained. This agrees with the arguments of He et al. [13] who reported that strength of metal/ceramic microlaminates can increase substantially as the ceramic layer thickness decreases below a critical value. Note also in Figure 4. 8 that the increase in UTS is sharper for the samples with $V_{Nb} = 0.86$ than for the samples with $V_{Nb} = 0.50$. This difference supports that idea that a larger volume percentage of Nb enhances crack bridging and microlaminate toughness and thereby leads to higher ultimate strengths.

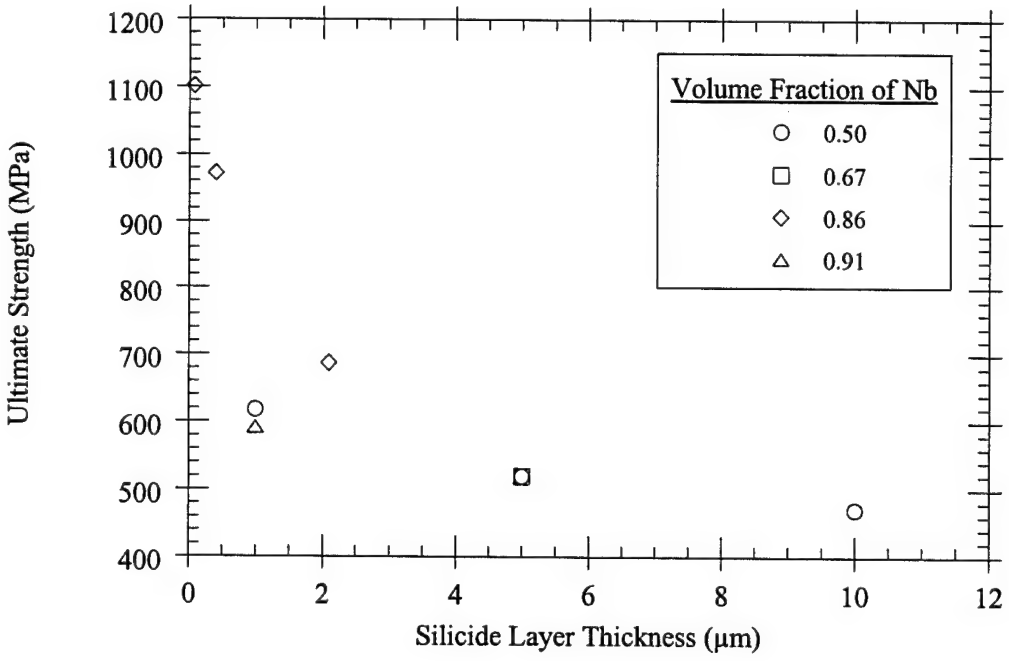

Figure 4. 8: The ultimate tensile strength of Nb/Nb_5Si_3 foils for each volume fraction of Nb as a function of silicide layer thickness.

4.4. Conclusions Regarding Room Temperature Mechanical Behavior

The Nb/Nb_5Si_3 microlaminate foils showed high strengths and small plastic elongations when tested in tension. The silicide layers fractured in a brittle manner and the Nb layers showed considerable local plasticity when blunting and bridging cracks during failures. The elastic limit for most samples was constant, near 560MPa, and appears to be controlled by fracture of the silicide layer. For samples with very small silicide layer thicknesses, there is some indication that the elastic limit increases substantially. The ultimate tensile strength of the microlaminates varied from 471MPa to 1101MPa. Generally, the UTS increased as bilayer thickness and silicide layer thickness decreased and as volume fraction of the Nb increased.

4.5. References for Section 4

1. J. D. Rigney and J. J. Lewandowski, *Metall. Mater. Trans. A* **27A,** 3292-3306 (1996).

2. R. G. Rowe, D. W. Skelly, M. Larsen, J. Heathcote, G. Lucas, and G. R. Odette, in *Properties of Microlaminated Intermetallic-Refractory Metal Composites*, Boston, MA, 1994 (Materials Research Society), p. 461-472.

3. L. Shaw and R. Abbaschian, *Acta metall. mater.* **42,** 213-223 (1994).

4. D. R. Bloyer, K. T. Venkateswara Rao, and R. O. Ritchie, in *Toughness and Subcritical Crack Growth in Nb/Nb3Al Layered Materials*, San Francisco, CA, 1996 (Materials Research Society), p. 243-248.

5. J. Heathcote, G. R. Odette, G. E. Lucas, R. G. Rowe, and D. W. Skelly, *Acta metall. Mater.* **44,** 4289-4299 (1996).

6. J. Rawers and K. Perry, *J. Mat. Sci.* **31,** 3501-3506 (1996).

7. W. Provancher and A. K. Ghosh, in *High Temperature Mechanical Behavior of Nb_5Si_3/Nb Laminates*, Boston, MA, 1995 (Materials Research Society), p. 1071-1076.

8. J. T. Beals and V. C. Nardone, *J. Mat. Sci.* **29,** 2526-2530 (1994).

9. A.V. Samat and J.J. Lewendowski, Metall. *Mater. Trans.* **28A**, 389-399 (1997).

10. M.G. Mendiratta R. Goetz, D.M. Dimiduk and J.J. Lewandowski, *Metall. Mater. Trans.* **26A**, 1767-1776 (1995).

11. W. C. Oliver and G. M. Pharr, *J. Mater. Res.* **7,** 1564-1583 (1992).

12. H. Ji, G. S. Was, and J. W. Jones, in *Synthesis and mechanical properties of niobium films by ion beam deposition*, San Francisco, CA, 1996 (Materials Research Society), p. 153-158.

13. M.Y. He, F.E. Heredia, D.J. Wissuchek, M.C. Shaw, and A.G. Evans *Acta metall. mater*, **41** 1223-1228 (1993).

5. High Temperature Microstructural Evolution and Breakdown

5.1. Introduction and Experimental Methods

The microstructural stability and the mechanisms by which microlaminates break down will be critical to the use of microlaminates in high temperature applications. However, the high temperature stability and breakdown mechanisms in microlaminates are not well documented.

In one of the few published studies of high temperature breakdown of microlaminates, Rowe et al. [1,2] and Cao et al. [3,4] examined the phase stability of Nb/Nb_3Al and $Nb/NbCr_2$ microlaminates. They found that these two sets of microlaminates broke down above 1000°C, primarily because the volume fraction of the two phases in each composite varied dramatically with temperature. In Nb/Nb_3Al microlaminates there was a sharp decline in the volume fraction of the Nb_3Al intermetallic at 1000°C, due to dissolution of Al from the intermetallic phase into the Nb. For the $Nb/NbCr_2$ microlaminates significant dissolution of $NbCr_2$ occurred above 1200°C. The dissolution of Al and Cr leads to both the deterioration of the high temperature properties of the composite and to the undesirable precipitation of Nb_3Al and $NbCr_2$ particles in the Nb layers on cooling to room temperature [1,2].

Besides the loss of phase stability in microlaminates at high temperatures, the microstructure of laminated composites can also break down by various other

mechanisms including grain growth, pore formation, and grain boundary grooving. The latter is particularly important in microlaminates in which the continuity of one of the layers is imperative to the creep properties of the composite [5].

The degree of grooving in polycrystalline microlaminates is controlled by the ratio of grain boundary and interfacial free energies. Consider the polycrystalline layers of materials A and B in Figure 5. 1. At the interfacial triple point in Figure 5. 1 (a), the equilibrium groove angle (2θ) is given by [6,7]:

$$2\cos(\theta) = \gamma_{gb}/\gamma_{int} \tag{5.1}$$

When the ratio of the grain boundary energy to the A-B interfacial free energy γ_{gb}/γ_{int} is small, a *shallow groove* results as shown for the A layers in Figure 5. 1 (b). In this case, the groove is unlikely to extend through the A layer, and pinch-off should not occur. In contrast when the ratio is large, *deep grooves* can extend completely through the layers resulting in pinch-off (as shown for the B layers in Figure 5. 1 (b)). This pinch-off destroys the layering and eventually leads to a gross coarsening of the microstructure. If the B-layers are designed to provide creep resistance for the microlaminate, pinch-off will be extremely detrimental to material's high-temperature mechanical properties [5]. Thus, both phase stability and microstructural stability are critical to the high temperature performance of these microlaminates.

Here we examine the phase stability, the microstructural stability, as well as the

chemical stability of Nb/Nb_5Si_3 microlaminate foils at elevated temperatures. The intention of the study is to attain a fundamental insight into both the stability of microlaminates as well as the relative importance of the various potential breakdown mechanisms. This will allow us to assess the feasibility of using microlaminates as high temperature materials as well as to identify how microlaminate stability can be enhanced by improving processing conditions.

(a)

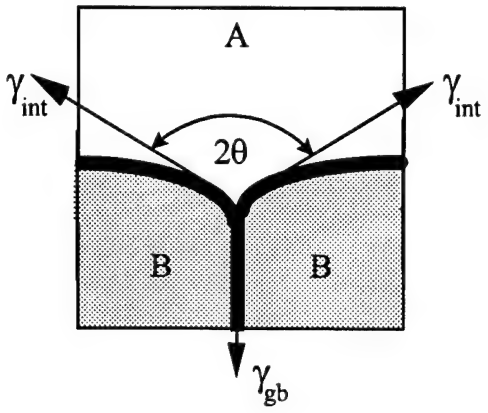

(b)

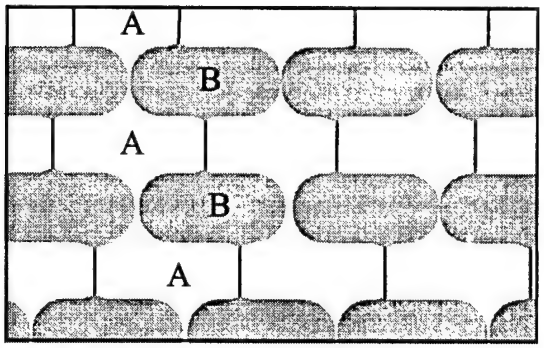

Figure 5. 1: (a) An enlarged view of a grain boundary groove at an interface between two phases A and B. The angle and depth of the groove are determined by the ratio of the grain boundary and interface free energies, γ_{gb}/γ_{int}. (b) Cross-sectional schematic of a microlaminate in which the constituent layers exhibit different grooving characteristics. In the B layers the γ_{gb}/γ_{int} ratio is large and there is significant grooving at the boundaries and layer pinch-off and layer break-down are likely. However, in the A layers γ_{gb}/γ_{int} is small and there is little grooving at the grain boundaries and the layers are stable.

To assess high temperature stability, free-standing microlaminate foils consisting of alternating 5 μm thick layers of Nb and Nb_5Si_3 (sputter deposited under conditions described previously) were heated under vacuum in the low 10^{-5}Torr range. To minimize contamination the samples were placed in a covered, alumina crucible during heat treatment. Additional anneals were also carried out in a tube furnace under purified, flowing Ar. During the Ar anneals the microlaminate foils were placed in a Ta box to limit environmental contamination.

The phases present in the foils after annealing were determined using X-ray diffraction, while the microstructural evolution after annealing was characterized using cross-sectional Scanning Electron Microscopy (SEM) and Transmission Electron Microscopy (TEM). The composition of the microlaminate was examined as a function of depth from the outermost surface using a sequential combination of ion milling and Auger analysis. The ion milling rate was such that an Auger scan was taken every 2.5nm with a 3 KeV beam.

5.2. Experimental Results

5.2.1. Annealing in Vacuum

Our previous experiments (Section 2) showed that annealing the as-deposited

microlaminates at 1200°C in vacuum for three hours crystallized the silicide layers, resulting in alternating layers of only the equilibrium phases: Nb and Nb_5Si_3; [8, 9] a typical cross-section of an annealed sample is shown in Figure 2.4. Note that the layering is completely intact with little interfacial roughening (Figure 2.4(a)). There is no evidence of porosity in either of the layers. TEM examination of the Nb_5Si_3 layers, though, revealed small second phase particles (Figure 2.4(b) and Figure 5. 3) situated predominantly at the grain boundaries and at triple points. EDS analysis showed that these particles are Si and Oxygen rich and electron diffraction from the particles produced only diffuse patterns. This suggests that the small grain boundary phase is an amorphous oxide.

Annealing in vacuum at 1400°C for three hours resulted in breakdown of the outer silicide layers of the microlaminate, apparently due to the loss of Si via sublimation (Figure 5. 2). Note in Figure 5. 2 that voids formed in the outer silicide layers, and that one side of the microlaminate foil lost considerably more Si than the other. This difference is attributed to the fact that one side of the microlaminate foil was in direct contact with the alumina crucible, apparently limiting Si loss, while the other side was exposed to vacuum. There is no evidence of porosity in the silicide layers in the interior of the microlaminate foil. Furthermore, within the microlaminate the layers exhibit little evidence of interfacial grooving. X-ray diffraction (coupled with electron diffraction studies) confirmed that the only crystalline phases present in the microlaminate foil are Nb and Nb_5Si_3. Heating to higher temperatures in vacuum resulted in more extensive losses of Si, and eventually to a complete breakdown of the silicide layers.

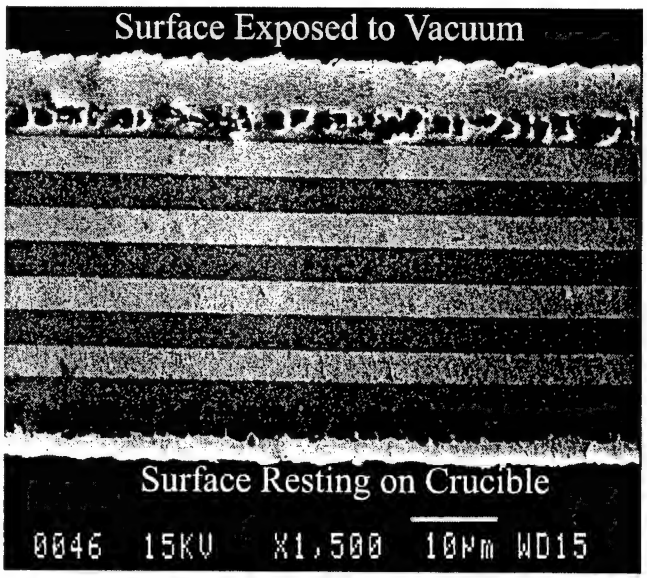

Figure 5. 2: Cross-section of a Nb/Nb_5Si_3 microlaminate annealed at 1400°C for 3 hours in vacuum. Notice that the silicide layer on the "vacuum side" of the microlaminate broke down completely, while the silicide layer on the "crucible side" is relatively intact

In order to suppress the loss of Si by sublimation, further anneals were carried out in vacuum in a Si-rich atmosphere. This was achieved by incorporating Nb_5Si_3 pellets in the covered alumina crucible during the vacuum anneals. The samples were suspended from alumina rods to prevent direct physical contact with the pellets. Using this technique it was found that silicon loss is completely suppressed even on annealing for 100 hours at 1400°C (Figure 5. 3 (a)). After 100 hours there is relatively little porosity in the silicide, and the only phases present were Nb and Nb_5Si_3. The layering is intact throughout the microlaminate with little additional grooving at the Nb/Nb_5Si_3 interfaces.

When anneals were conducted at 1500°C for 3 hours, the Si-rich environment was no longer able to suppress the loss of Si, resulting in extensive porosity in the outermost silicide layers (Figure 5. 4). Interestingly, the breakdown is far more extensive near the

ends of the microlaminate foil (which were exposed directly to the atmosphere) than near the surfaces of the sample. Annealing at 1600°C resulted in catastrophic breakdown of the microstructure, even at positions distant from the edges of the sample, with almost no Si remaining in the structure.

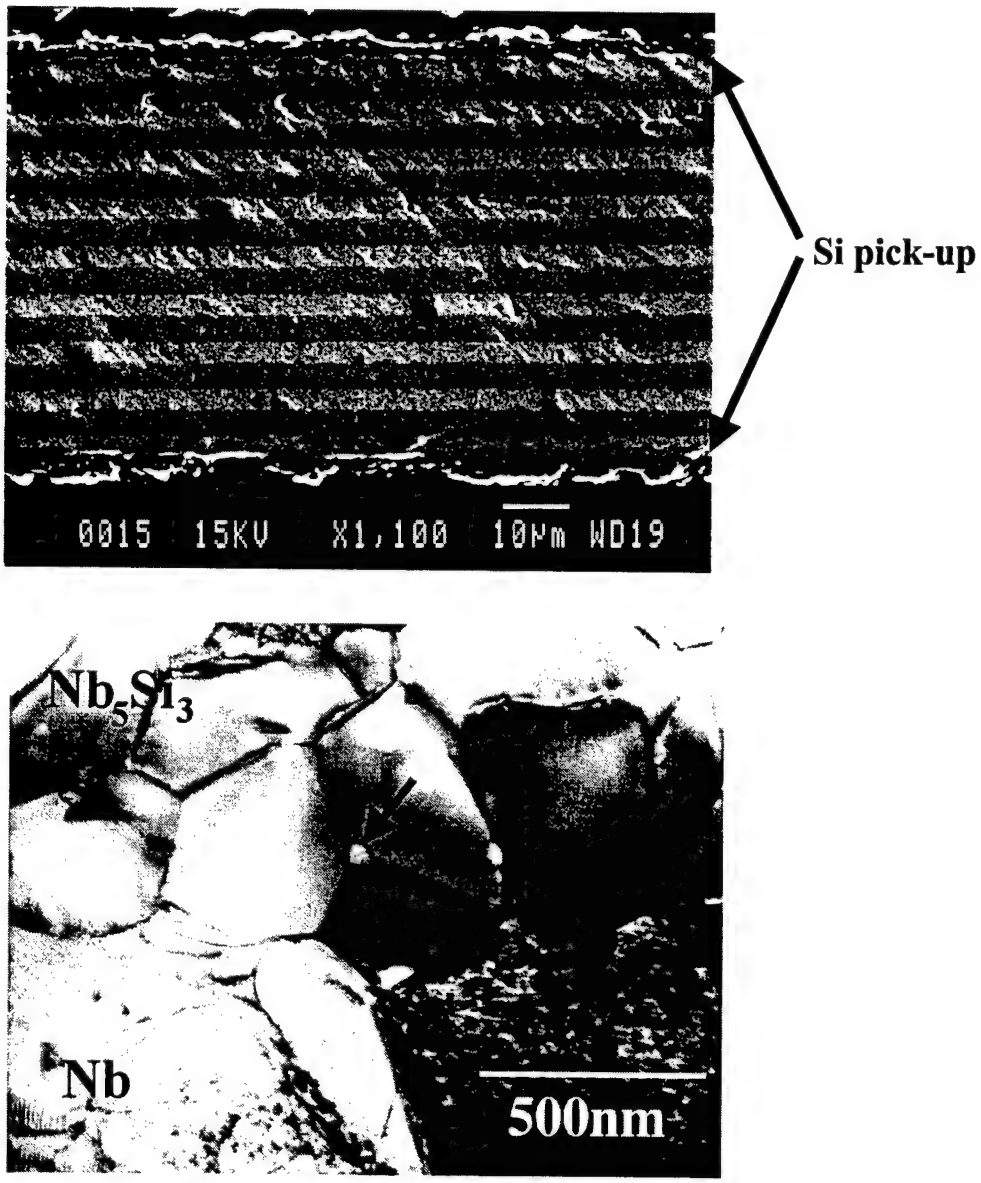

Figure 5. 3: Nb/Nb_5Si_3 microlaminate annealed at 1400°C for 100 hours under vacuum in a Si-rich atmosphere (a) SEM micrograph, (b) TEM micrograph. The Si-rich atmosphere suppressed the Si loss evident in Figure 5. 2 and in fact there is evidence of net Si pick-up by the outermost Nb layers (arrowed in (a)). An example of an amorphous oxygen-rich intergranular particle in the Nb_5Si_3 layers is arrowed in (b).

End of multilayer exposed to vacuum

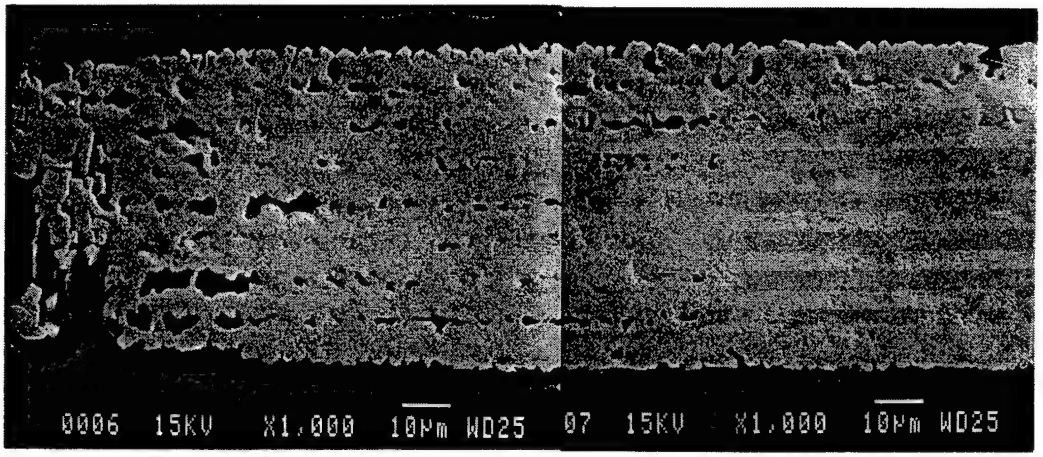

Figure 5. 4: Cross-section of the end of a Nb/Nb_5Si_3 microlaminate annealed at 1500°C for 3 hours in a Si-rich atmosphere. The porosity observed results from Si loss from the silicide layers. Notice that Si is lost from the ends of the silicide layers more rapidly than perpendicular to the layering (SEM micrograph).

5.2.2. Ar Atmosphere

In order to further suppress the loss of Si, anneals were carried out under flowing Ar. Annealing at 1500°C for 3 hours under these conditions yielded minimal Si losses (Figure 5. 5 (a)). Note in Figure 5. 5 (a) that the layering is still intact and there is relatively little grooving at the Nb/Nb_5Si_3 interfaces. However, more pores had formed within the interior silicide layers than is evident on annealing for 100 hours at 1400°C in vacuum (Figure 5. 3(a)). This increased porosity could not be associate with surface sublimation of Si because the outer silicide layers showed no loss of Si. In addition, there is only minimal loss of Si from the ends of the silicide layers (Figure 5. 5(b)).

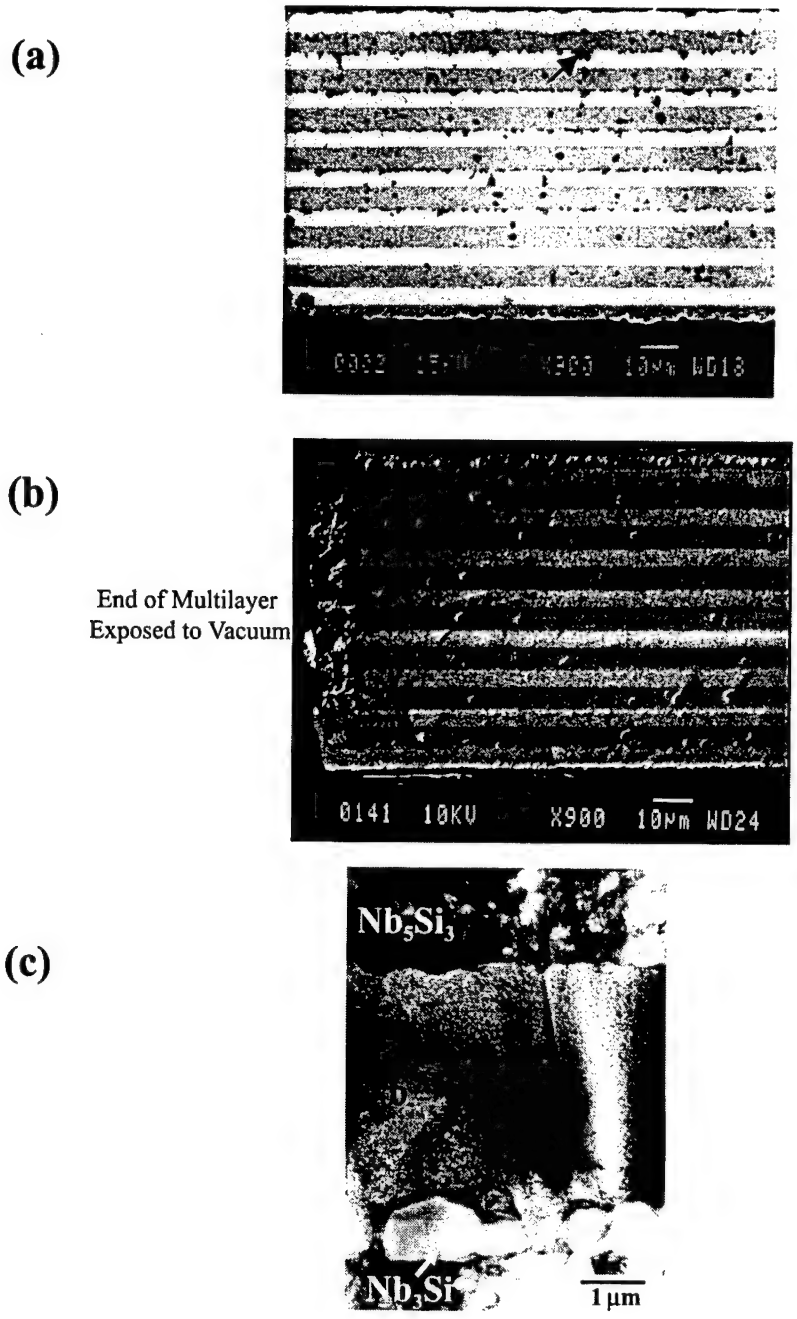

Figure 5. 5. Nb/Nb_5Si_3 microlaminate annealed at 1500°C for 3 hours in an Ar overpressure (a) Back-scattered electron image showing the formation of an interfacial Nb_3Si phase (arrowed). Notice that the interfacial phase nucleates predominantly on the lower Nb/Nb_5Si_3 interface in each Nb layer. (b) SEM cross-section of the end of the annealed microlaminate showing that virtually no breakdown of the silicide layers occurred via Si sublimation during annealing. (c) TEM image of a microlaminate cross-section showing the metastable Nb_3Si interfacial phase.

(a)

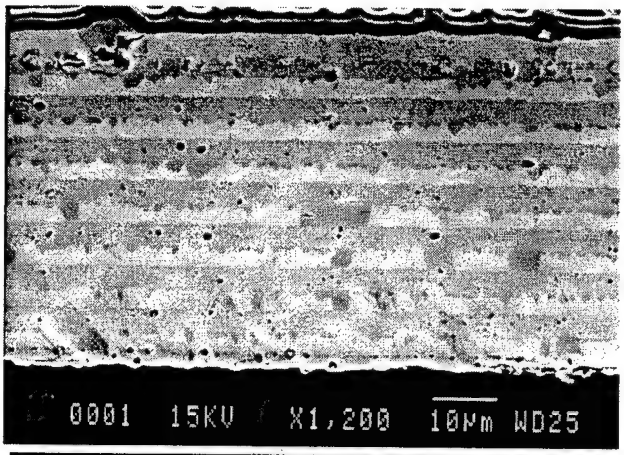

(b)

End of Multilayer Exposed to Vacuum

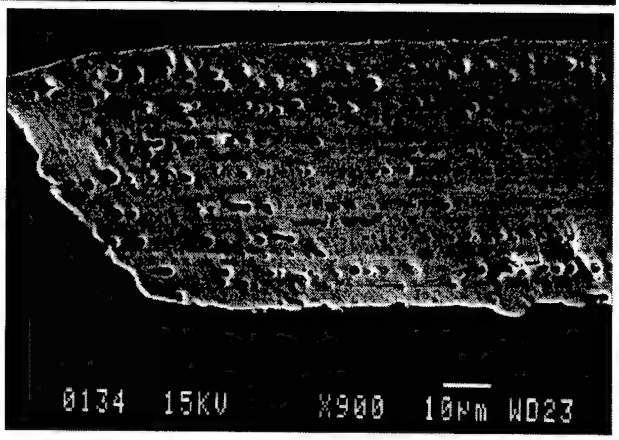

(c)

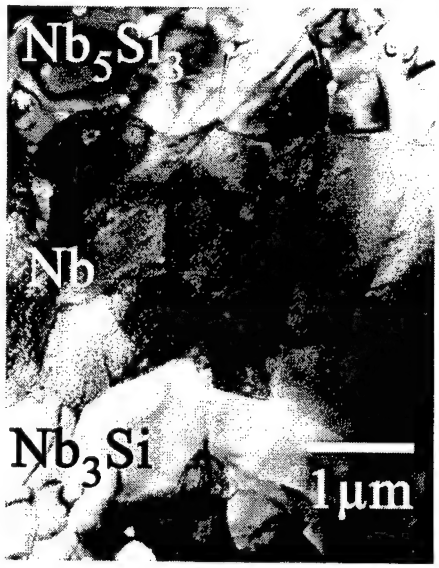

Figure 5. 6: Nb/Nb_5Si_3 microlaminate annealed for 3 hours at 1600°C in an Ar overpressure (a) SEM cross-section of the microlaminate showing the Nb_3Si phase as well as breakdown of the outermost silicide layers. (b) SEM of cross-section of end of microlaminate showing extensive loss of Si from the silicide layers. (c) TEM micrograph showing the formation of a metastable Nb_3Si interfacial phase. Notice that on annealing at this temperature significant grain growth occurred in the silicide layers (relative to Figure 2.4(b)).

Examination of Figure 5. 5 (a) and (c) reveals that an interfacial phase formed when annealing at 1500°C. Interestingly, Figure 5. 5 (c) suggests that the presence of this phase is largely limited to one side of each Nb layer. Using TEM the interfacial phase was identified as cubic ($L1_2$) Nb_3Si, a metastable form of the high temperature equilibrium ($P4_2/n$) Nb_3Si phase [10,11].

When annealing the Nb/Nb_5Si_3 microlaminates at 1600°C under Ar (Figure 5. 6) the degree of interfacial grooving did not increase compared to annealing at 1500°C in Ar (Figure 5. 5). However, there is a higher volume fraction of interfacial phase and an increased loss of Si via sublimation (Figure 5. 6 (a) and (c)). Si was lost from both the outermost silicide layers (Figure 5. 6(a)), as well as from the exposed ends of the microlaminate sample by direct sublimation from the silicide phase (Figure 5. 6(b)).

5.3. Discussion

Three types of instabilities or breakdown mechanisms were detailed in the previous section, namely chemical instabilities, phase instabilities and microstructural instabilities. The predominant chemical instability is the loss of Si via sublimation. Phase instabilities include the dissolution of Si from the Nb_5Si_3 layers, the presence of an amorphous intergranular phase in the Nb_5Si_3 layers, and the formation of a metastable interfacial phase. The microstructural instabilities encompass interfacial grooving, the formation of porosity, and grain growth. In this section we consider each of these instabilities as well as their overall impact on the structural integrity of the

microlaminates. We also consider how these breakdown mechanisms can be minimized through improved processing.

5.3.1. Chemical Instability

The major chemical instability observed on annealing Nb/Nb_5Si_3 microlaminate foils was the loss of Si via sublimation at temperatures exceeding 1200°C. There are two distinct paths in the microlaminate geometry through which the Si is lost. In one path Si diffuses perpendicular to the layering and sublimes into the surrounding environment at the surface of the outermost Nb layer. In the other path, Si is lost parallel to the layering via direct sublimation to the environment from the exposed ends of the Nb_5Si_3 layers.

The rate at which Si is lost perpendicular to the layering is determined by at least one of several factors that include: the equilibrium vapor pressure of Si, the diffusion rate of Si through the outer Nb layers, and the sublimation rate of Si from the surface during the anneals. The first two factors will be examined using vapor pressure and diffusion data for Si, but since the sublimation of Si is highly dependent on the chemistry of the Nb surface and the presence of any surface oxides, this third factor will not be considered here.

Using the literature values for the diffusivity of Si in Nb (Q=201.6 kJ/mol and $D_0= 5.1x10^{-7}m^2/sec$) [12], we estimated the time that would be required for all of the Si in the outermost Nb_5Si_3 layers to diffuse through the outermost Nb layers. The required

time is 77 hours at 1200°C, 2.7 hours at 1400°C, 1.1 hours at 1500°C and 0.38 hours at 1600°C. These calculations suggest that only 4% of the Si in the outermost silicide layers would be lost after a 3 hour anneal at 1200°C. This prediction is consistent with the apparent stability of the silicide layers shown in Figure 2.2. The calculations also imply that 3 hour anneals at 1400°C and higher would lead to a complete loss of Si from the outer silicide layers as observed in Figure 5. 2.

In the above calculations we assumed that Si sublimation from the Nb free surface is not a rate-limiting factor. However, sublimation can be influenced by the partial pressure of Si in the immediate vicinity of the surface. Assuming that the Nb layers are fully saturated with Si at any given temperature (i.e. they contain the equilibrium solubility limit of Si), the calculated equilibrium partial pressure of Si is shown in Figure 5. 7 [13]. From the diagram it can be seen that the equilibrium vapor pressure of Si for the Nb alloy varies from approximately 10^{-8} Torr at 1200°C to 10^{-4}Torr at 1600°C. The low partial pressure at 1200°C implies that the equilibrium vapor pressure of Si could be obtained in the closed crucible, thereby eliminating the thermodynamic driving force for the sublimation of Si from the outermost Nb layers at this temperature. Thus, both the build-up of Si in the surrounding environment, as well as the relatively low diffusion rate of Si through the outermost Nb layer, could impede Si loss at 1200°C. At 1400°C suppressing the sublimation of Si would require a Si partial pressure of approximately 10^{-6} Torr. This higher pressure could not be maintained in the crucible as evidenced by the degradation shown in Figure 5. 2. However, it could be maintained in the small micro-environment that developed between the foil and the bottom of the crucible. Note that the side of the

foil which rested on the base of the crucible did not loose extensive amounts of Si while the side exposed to the atmosphere of the crucible lost extensive amounts of Si in its outer silicide layer. This particular result suggests that the degree of Si loss is controlled by the partial pressure of Si and not the rate at which it diffuses through the outer Nb layer.

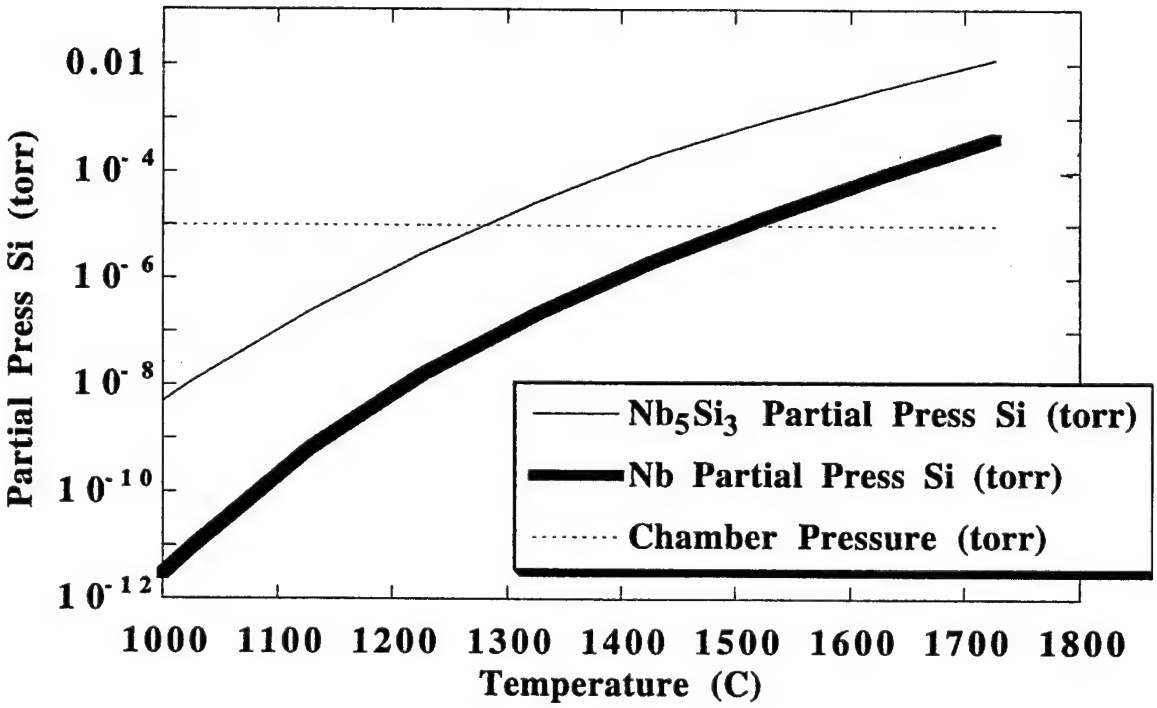

Figure 5. 7: Calculated vapor pressure of Si on the surface of a saturated Nb alloy, and from Nb_5Si_3 as a function of temperature (based on data in [13]).

To suppress Si loss when annealing in vacuum at temperatures above 1200°C, we artificially raised the Si partial pressure in the crucible by including pellets of Nb_5Si_3 within the crucible. Figure 5. 7 shows that at 1400°C the equilibrium Si vapor pressure from the Nb_5Si_3 pellets is approximately 10^{-4} Torr, 100 times higher than the partial

pressure above the Nb layers. Thus, by including Nb_5Si_3 pellets in the crucible, one can generate a Si-rich environment that suppresses Si loss from the microlaminates for up to 100 hours at 1400°C (Figure 5. 3). In fact, the outer Nb layers now act as a sink for Si and there is a net gain of Si as shown in Figure 5. 3(a). However, at 1500°C and 1600°C this technique was unable to sustain the partial pressures of Si that were needed (roughly 10^{-5}Torr at 1500°C and 10^{-4}Torr at 1600°C) to prevent the sublimation of Si from the microlaminates. The lack of a Si "overpressure" led to the catastrophic breakdown of the silicide layers in the microlaminates.

In contrast to the vacuum-based experiments, the loss of Si by sublimation at 1500°C could be suppressed by annealing in flowing Ar. The Ar atmosphere does not reduce the equilibrium vapor pressure of Si, but it does dramatically change the kinetics for the sublimation of Si from the surface. Furthermore, these anneals were carried out with the samples wrapped in Ta foil which may have enabled a sharp increase in the local Si vapor pressure, thereby reducing or eliminating its sublimation. Nevertheless, at 1600°C even these conditions could not prevent Si loss (Figure 5. 6).

While Si loss perpendicular to the layering via diffusion through the Nb layers is relatively slow and limited to the sequential loss of layers, the loss of Si parallel to the layers is rapid (Figure 5. 4 and Figure 5. 6(b)). Indeed, on annealing at 1500°C in a Si-rich atmosphere the Si loss occurred approximately seven times faster parallel to the layering than perpendicular to it (Figure 5. 4(a)). Furthermore, it is apparent from Figure 5. 4 that the breakdown of the silicide results in a interconnected series of pores which

facilitates the loss of Si to much greater depths than might otherwise have been possible. These results suggest that the design of microlaminates for turbine blade applications should prevent the direct exposure of Nb-based silicide phases to the environment. The use of protective coatings to prevent chemical instabilities will clearly be important.

5.3.2. Phase Instability

One of the major mechanisms by which phases breakdown in refractory metal/intermetallic microlaminate systems was identified to be the dissolution of the intermetallic phase into the refractory metal [1,2]. In our system this breakdown mechanism would be manifested by the dissolution of Si from the Nb_5Si_3 into the Nb when annealing at high temperatures. However, Figure 5. 3(a), Figure 5. 5 (a) and Figure 5. 6 (a)), show that the silicide layers have not thinned significantly on annealing at elevated temperatures even though there was sufficient time at temperature to establish the equilibrium concentration of Si in the 5μm thick Nb layers [12]. This apparent lack of significant dissolution is consistent with the Nb-Si phase diagram that predicts a limited increase in the solubility of Si in Nb with temperature. In fact, solubility is only expected to increase from 0.6at% at 1300°C to 1.3at% at 1700°C, which translates to a 2.3% decrease in the thickness of the Nb_5Si_3 layer on going from 1300°C to 1700°C [14]. Such a limited reduction in thickness would be difficult to detect in these experiments.

WDS confirmed that the Si content in the Nb layers was consistent with the values predicted in the Nb-Si equilibrium phase diagram. For example on cooling from

1400°C, 0.4at% Si was measured in the Nb layers. However, no silicide precipitates were observed in the Nb layers after annealing at 1400°C. This suggests that unlike the Nb-Al and Nb-Cr systems examined previously by Rowe et al., the equilibrium phases in the Nb/Nb_5Si_5 phases are relatively stable and remain in their distinct layers.

The second mechanism by which phase instabilities can arise is the formation of metastable phases. When the microlaminates were annealed at 1500°C a Nb_3Si phase formed on the Nb/Nb_5Si_3 interfaces (Figure 5. 5). Due to its (anticipated) lower melting point, Nb_3Si is likely to exhibit poor creep resistance compared to Nb_5Si_3. Thus, the presence of Nb_3Si is likely to have an adverse effect on the creep properties of the microlaminates. We consider two possible sources for the formation of this interfacial metastable phase, namely impurities and stresses.

Based on the method of deposition the highest concentrations of impurities in this system are likely to exist at the interfaces between the layers. As the substrates are rotated from one sputter gun to the other to achieve layering, the freshly deposited Nb and silicide surfaces are exposed to background gases and hence impurities for approximately 1 second. Since the Nb surfaces are considerably more reactive than the Nb_5Si_3 surfaces, they are likely to have a higher "sticking coefficient" for contaminants. Therefore, the greatest concentration of impurities should appear along the interfaces at which silicide layers were deposited onto Nb layers. However, examination of Figure 5. 5(a) reveals that the Nb_3Si phase formed along the opposite interfaces, those at which Nb was deposited onto Nb_5Si_3. Thus, the interfaces that are most likely to be contaminated

with impurities contained little or no Nb_3Si. This suggests that the Nb_3Si metastable phase was not impurity stabilized. This conclusion is further supported by the Auger depth-profiling analysis. The 3 KeV electron beam used for acquiring the Auger spectrum beam gives a compositional sampling depth similar to the 2.5nm that was milled off during each successive ion milling stage. Thus any discrete interfacial contamination layers should have been detected during this analysis. However, Auger depth profiling produced no evidence of any contamination (i.e. oxygen, carbon or nitrogen) at any of the interfaces. Additional studies using SIMS will be required to confirm these observations.

The second potential driving force for the presence of the metastable Nb_3Si phase is stress. Nb has a density of 8.534g/cm^3, the observed ($L1_2$) Nb_3Si has a density of 6.823g/ cm^3, and Nb_5Si_3 has a density of 7.150g/ cm^3. The significance of these densities to the stresses present is best considered by comparing the relative atomic packing efficiencies in each of these phases. The densities translate to a volume/atom ratio (normalized to Nb) of 1: 1.03: 0.88 for Nb: Nb_3Si: Nb_5Si_3. Thus the atomic packing in Nb_3Si is less dense than in either Nb or Nb_5Si_3 and consequently tensile stresses would tend to favor the formation of Nb_3Si over Nb_5Si_3. Examination of Figures 5.5 and 5.6 reveals that the Nb_3Si phase forms predominantly on the Nb side of the interfaces, suggesting that if it's presence is stress induced, the Nb layers must be under tension during its formation. At elevated temperatures the sources of stress in the microlaminate are likely to be thermal mismatch between the layers and densification due to grain growth in the Nb_5Si_3 layers. The former would tend to dominate, and generate

compressive stresses of several hundred MPa in the Nb layers and equal tensile stresses in the Nb_5Si_3 layers. While these stresses will decay at elevated temperatures, the compressivel stresses in the Nb layers will inhibit the formation of Nb_3Si.

However, tensile stresses would be generated in the Nb layers on cooling. During extended anneals at elevated temperatures the stresses in the microlaminate will decay to nearly zero. On subsequent cooling the differences in CTE will result in tensile stresses being generated in the Nb, creating a driving force for the formation of Nb_3Si. Furthermore, on cooling the Nb layers would become supersaturated with Si, creating a driving force for the formation of precipitates. On the basis of the existing equilibrium Nb/Si binary phase diagram, Nb_5Si_3 should precipitate on cooling due to supersaturation. However, the precipitation of Nb_3Si from a Nb-Si solid solution (containing 4.8% Si) would generate approximately 5% more volume than the precipitation of Nb_5Si_3, and therefore may be partially stabilized by reducing elastic strain energy in the Nb layers. The assertion that the Nb_3Si forms on cooling from the supersaturated Nb layers is supported by the observation that the amount of Nb_3Si observed in Figures 5.5(a) and 5.6(a) increases from 2.8(areal) % in the microlaminate annealed at 1500°C to 7.3(areal)% in the sample annealed at 1600°C. Assuming that the observed Nb_3Si formed from precipitation of Si from supersaturated Nb, this would require a Si solubility in the Nb of roughly 3.5at% Si at 1600°C and 1.5at% at 1500°C. These solubilities are consistent with older versions of the Nb/Si phase diagram [15], but higher than those reported more recently by Mendiratta and Dimiduk [14]. The fact that the phase nucleates predominantly on one interface in both foils is likely either the result of

bending stresses being generated in the foil, or possible residual compositional or morphological differences between the interfaces.

The third observed phase instability was the presence of an oxygen-rich amorphous phase that appears as small particles at grain boundary triple points in the Nb_5Si_3 layers (Figure 5. 3(b)). The presence of this phase is likely the result of an incorporation of oxygen in the silicide target, rather than contamination during processing. Glassy grain boundary phases such as these are deleterious to the creep properties of silicides [16, 17] and need to be eliminated by depositing from higher purity targets or by alloying.

5.3.3. Microstructural Instabilities

The microstructure of the individual laminates can change at elevated temperatures as interfaces groove, pores form, and grains grow. Here we consider each of these microstructral instabilities.

The stability of the interface between two layered materials depends on the degree of grooving that occurs when grain boundaries intersect these interfaces as shown in Figure 5. 1. The most stable interfaces will have large groove angles because their interfacial free energy is higher than the energy of the corresponding grain boundary. Examination of the interfaces between the Nb and Nb_5Si_3 in Figure 5. 6(b) reveals that the average groove angle made when a Nb grain boundary intersects an Nb/Nb_5Si_3

interface (2θ in Figure 5. 1) is 84° (see Figure 5. 8(a)). This implies that the ratio of interfacial free energies is $\gamma_{gb}/\gamma_{int} = 1.49$ based on equation (5.1). The angle subtended by a Nb_5Si_3 grain at a Nb/Nb_5Si_3 interface is harder to determine because of the small grain size of the silicide phase. However, it would appear that the average angle made by a Nb_5Si_3 grain boundary at the Nb/Nb_5Si_3 interface is approximately 120° (Figure 5. 8(b)), implying that $\gamma_{gb}/\gamma_{int} = 1$. Notice in Figure 5. 8(b), however, that there are glassy phase particles at virtually all of the Nb_5Si_3/Nb grain boundary triple points. The glassy phase alters the force balance at the triple points, distorting the relative values. Nevertheless, for our Nb/Nb_5Si_3 microlaminates, based on the above analysis, the grooving of the Nb grains into the silicide is more significant than the grooving of the silicide into the Nb layers. Consequently, the Nb layers are more likely to break down by pinch-off than the silicide layers. Thus, the breakdown would resemble that shown in Figure 5. 1(b) with the layers labeled B in the figure representing the Nb and the layers labeled A representing Nb_5Si_3. The fact that the silicide layers are more likely to remain continuous is important given they can provide creep resistance at high temperatures; discontinuities in the silicide layers would drop creep resistance dramatically.

Grain growth is the second microstructural instability in the microlaminates. The as-deposited Nb grains recrystallize on heating to 1200°C and form a stable grain structure during all of the high temperature anneals. However, the silicide grains crystallize at 800°C and then grow larger with each increase in annealing temperature. The dependence of the grain size on annealing temperature is given in Table 5.1. The average grain size ranges from 200nm at 1200°C to approximately 1000nm at 1600°C.

These small grain sizes will offer limited creep resistance and need to be enhanced via alternate processing techniques.

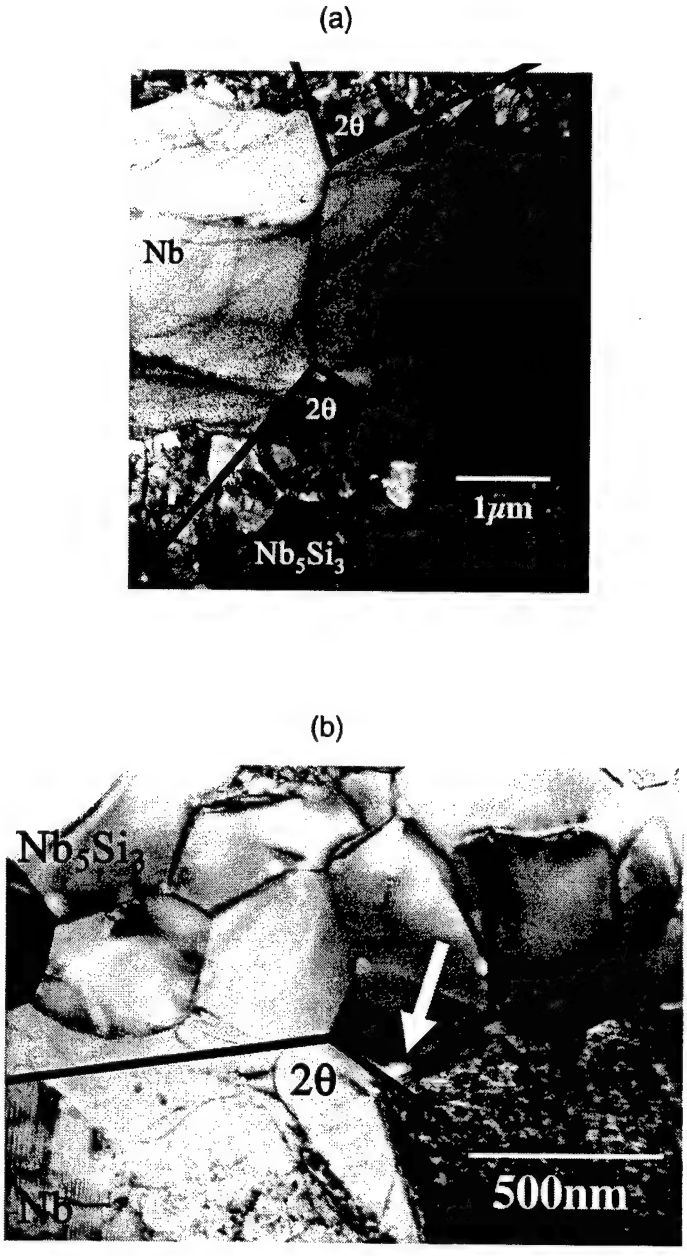

Figure 5. 8: Grain boundary grooving at a Nb/Nb_5Si_3 interface showing the grooving angles along (a) a Nb grain boundary and (b) a Nb_5Si_3 grain boundary. The angles measured in (b) are probably influenced by the presence of amorphous particles present at the interface, an example is arrowed in (b).

Table 5.1. Microstructural Characterisitics of the Nb_5Si_3 layers as a Function of Heat Treatment.

Heat treatment	Measured Porosity	Theoretically* Predicted Porosity	Silicide Grain Size (nm)
As-deposited	0%	0%	N/A
1200°C/3hours	0.05%	0%	200
1400°C/100 hours	1.28%	0.5%	300
1500°C/3hours	1.2%	1.2%	500
1600°C/3hours	1.4%	1.8%	1000

* Predicted based on the excess volume generated by the observed grain growth in the silicide layers (after [18]).

The third mechanism by which microstructures degraded was the formation of pores in the inner silicide layers of the microlaminate. The area percentage of pores in the silicide layers was measured using image processing to be 0.05% after the 1200°C anneal, 1.28% porosity after the 1400°C anneal, 1.2% porosity after the 1500°C anneal and 1.4% after the 1600°C anneal. These pores are not associated with the surface sublimation of Si as they are distributed uniformly in all of the silicide layers. Nor could they be generated by the coalescence of Ar that was trapped during sputter deposition of the foils as there is no porosity in the Nb layers. The formation of these pores is most likely driven by tensile stresses in the silicide layers that arise on annealing. These stresses are generated by volume changes that are associated with crystallization, thermal expansion, and grain growth, as discussed earlier. Since the porosity increases with increasing temperature, the latter two sources are the most likely ones because the magnitudes of their driving forces are temperature dependent.

To understand how grain growth can lead to volume changes in the silicide phase, we note that grain boundaries have a lower density that the bulk Nb_5Si_3 phase. As the silicide grains grow and the total area of grain boundaries decrease, the total volume of the silicide phase will decrease as well. While the resulting volume changes are small for most bulk materials, growth of submicron grains in vapor deposited materials can lead to significant changes in volume as noted by Chen and Spaepen [18]. We used their model to estimate that the volume of the silicide phase would decrease by 0.5% after the 1400°C anneal, 1.2% after 1500°C anneal and 1.8% after the 1600°C anneal due to grain growth. If the Nb constrained this densification one might expect pores to form with a volume percentage equivalent to the decrease in volume of the silicide. Quite surprisingly the volume percentage of pores listed in Table 1 closely match the percentage decreases in volume that we calculated. While the Nb layers are likely to offer limited constraint to the densification of the silicide layers at high temperatures, the close agreement of the predicted and measured volumes suggest that grain growth is likely to play an important role in the formation of the pores. Thus, while growth of the silicide grains is essential for imparting creep resistance, it appears to give rise to porosity in the silicide layers. This strongly suggests the need for different processing routes that either avoid post-deposition grain growth or apply pressure during high temperature anneals.

5.4. Conclusions on Microstructural Breakdown in Microlaminates

1) The predominant high temperature breakdown mechanism observed in Nb/Nb_5Si_3 microlaminates was the loss of Si via sublimation from the outermost Nb_5Si_3 layers. This loss occurred via the diffusion of Si perpendicular to the layering through the outermost Nb layer and sublimation to the atmosphere. The rate of Si loss was controlled by a combination of the diffusion rate of Si in Nb and the prevailing Si vapor pressure.
2) The loss of Si parallel to the layering at elevated temperatures occurred via direct Si sublimation from the exposed ends of the Nb_5Si_3 layers. The rate of Si loss was far more rapid parallel to the layering than perpendicular to the layering. Si sublimation was substantually reduced by carrying out anneals in Ar compared to vacuum.
3) Minimal dissolution of Si from the silicide layers into the Nb occurred on annealing at elevated temperatures.
4) A metastable Nb_3Si phase formed on the Nb-side of the interfaces in samples annealing at 1500°C to 1600°C. The phase is thought to form on cooling from these temperatures as a result of precipitation of Si from the Nb layers. The formation of this phase, rather than the equilibrium Nb_5Si_3 phase is attributed to the development of tensile stresses in the Nb layers on cooling.
5) An amorphous intergranular phase forms in the Nb_5Si_3 layers on annealing. The formation of this phase is associated with oxygen impurities contained in the Nb_5Si_3 sputtering target and can be eliminated by using higher purity targets or by alloying.
6) The Nb/Nb_5Si_3 interfaces exhibit considerable morphological stability with relatively

little grooving, even after annealing at 1600°C. The measured groove angles suggest that breakdown is most likely to occur via pinch-off of the Nb layers than via pinch-off of the silicide layers.

7) The grain size of the silicide layer was persistently sub-micron even on annealing at 1600°C for 3 hours. Alternate processing routes will be needed to enlarge the Nb_5Si_3 grain structure for high temperature applications.

8) Pores develop in the silicide layers on annealing at elevated temperatures. The porosity is attributed to tensile stresses in the silicide layers that arise on annealing. The predominant driving forces for the tensile stresses in the silicide layers are the crystallization of the amorphous as-deposited Nb_5Si_3, the mismatch in coefficient of thermal expansion between the Nb and silicide layers, and grain growth in the silicide layers.

References for Section 5

1. P.G. Rowe, D.W. Skelly, M. Larsen, J. Heathcote, G.R. Odette and G. Lucas: *Scripta Metall. Mater.*, 1994, vol. 31, pp. 1487-92.

2. P.G. Rowe, D.W. Skelly, M. Larsen, J. Heathcote, G. Lucas, and G.R. Odette: *High Temperature Silicides and Refractory Alloys*, Materials Research Society Symposia Proceedings, Boston, MA, 1994, Materials Research Society, Pittsburgh, PA, 1994, vol. 322, pp. 461-72.

3. H. Cao, J.P.A. Lofvander, A.G. Evans, R.G. Rowe, and D.W. Skelly: *Mater. Sci. Eng.*, 1994, vol. A185, pp. 87-95.

4. G.R. Odette, B.L. Chao, J.W. Sheckherd and G.E. Lucas: *Acta Metall. Mater.*, 1992, vol. 40, pp. 2381-89.

5. D. Josell and F. Speapen: *Acta Metall. Mater.*, 1993, vol. 41, pp. 3017-27.

6. L.E. Murr: *Interfacial Phenomena in Metal and Alloys*, Addison-Wesley, Reading, Massachusetts, 1975.

7. W.W. Mullins: *Metall. Mater. Trans. A,* 1995, vol 26A, 1917-29.

8. D. Van Heerden, A.J. Gavens, T. Foecke and T.P. Weihs: *Mater. Scie. Eng, A*, 1999, vol 261, pp. 212-16.

9. A.J. Gavens, D. Van Heerden, T. Foecke and T.P. Weihs: *Metall. Mater Trans. A*, 1999, vol. 30A, pp. 2959-65.

10. F. Galasso and J. Pyle: *Acta. Cryst.*, 1963, vol. 16, pp. 228-29.

11. M.E. Schlesinger, H. Okamoto, A.B. Gokhale and R. Abbaschian: *J. Phase. Equilib.*, 1993, vol. 14, pp. 502-09.

12. T.Y. Kosolapova (ed): *Handbook of High Temperature Compounds: Properties, Production, Applications*, Hemisphere Publishing Corporation, New York, NY, 1990.

13. I. Barin: *Thermochemical Data of Pure Substances,* 3rd ed, VCH, New York, NY, 1995, p. 322.

14. M.G. Mendiratta and D.M Dimiduk: *Scripta Metall. Mater.*, 1991, vol. 25, pp. 237-42

15. T.B. Massalski (ed) *Binary Alloy Phase Diagrams*, ASM Metals Park, OH (1986)

16. K. Sadananda, C.R. Feng, R. Mitra and S.C. Deevi: *Mater. Sci. Eng.*, 1999, vol.

A261, pp. 223-28.

17. B.J. Hockey, S.M. Wiederhorn, W. Liu, J.G. Baldoni and S.T. Buljan: *J. Mater. Sci.*, vol. 26, pp. 3931-39.

18. L.C. Chen and F. Spaepen: *J. Appl. Phys.*, 1991, vol. 69, pp. 679-88.

6. Future Work:

1) Refine microlaminate production so as to produce large grained Nb_5Si_3 layers in microlaminate form. Potential production techniques include (1) hot pressing of Nb/Si sandwiches to reactively form laminates and (2) heating the substrates during vapor deposition.

2) Verify the impact of layer thickness, volume fraction, and residual on room temperature mechanical properties.

3) Identify the driving force(s) for the observed metastable, interfacial Nb_3Si phase that forms in Nb/Nb_5Si_3 microlaminates on annealing at and above 1500C.

4) Eliminate the amorphous intergranular phase that forms in the Nb_5Si_3 layers. This may be achieved by improving the purity of the silicide layers or it may require alloying of the silicide phase.

5) The observed microstructural stability of Nb/Nb_5Si_3 microlaminates at 1500°C suggests these materials may have a future in high-temperature structural applications. However, the high temperature mechanical properties of Nb/Nb_5Si_3 microlaminates, in particular their creep properties, must be quantified and compared to those of cast and hot extruded Nb/Nb_5Si_3 composites, as well as commercial alloys. The effects of composite geometry and material microstructures on silicide creep rates must be explored using experiments and modeling inorder to optimize the grain size and geometry of the silicide phase.

6) Finally it will be necessary to develop Nb alloys which are resistant to oxidation at elevated temperatures and the creep resistance of these phases must be examined.